

AD\_\_\_\_\_

Award Number: W81XWH-07-1-0247

TITLE: Transrectal Near-Infrared Optical Tomography for Prostate Imaging

PRINCIPAL INVESTIGATOR: Daqing Piao, Ph.D.

CONTRACTING ORGANIZATION: Oklahoma State University  
Stillwater, OK 74078

REPORT DATE: March 2009

TYPE OF REPORT: Annual

PREPARED FOR: U.S. Army Medical Research and Materiel Command  
Fort Detrick, Maryland 21702-5012

DISTRIBUTION STATEMENT: Approved for Public Release;  
Distribution Unlimited

The views, opinions and/or findings contained in this report are those of the author(s) and should not be construed as an official Department of the Army position, policy or decision unless so designated by other documentation.

REPORT DOCUMENTATION PAGE				Form Approved OMB No. 0704-0188	
Public reporting burden for this collection of information is estimated to average 1 hour per response, including the time for reviewing instructions, searching existing data sources, gathering and maintaining the data needed, and completing and reviewing this collection of information. Send comments regarding this burden estimate or any other aspect of this collection of information, including suggestions for reducing this burden to Department of Defense, Washington Headquarters Services, Directorate for Information Operations and Reports (0704-0188), 1215 Jefferson Davis Highway, Suite 1204, Arlington, VA 22202-4302. Respondents should be aware that notwithstanding any other provision of law, no person shall be subject to any penalty for failing to comply with a collection of information if it does not display a currently valid OMB control number. <b>PLEASE DO NOT RETURN YOUR FORM TO THE ABOVE ADDRESS.</b>					
1. REPORT DATE (DD-MM-YYYY) 01-03-2009		2. REPORT TYPE Annual		3. DATES COVERED (From - To) 1 MAR 2008 - 28 FEB 2009	
4. TITLE AND SUBTITLE  Transrectal Near-Infrared Optical Tomography for Prostate Imaging				5a. CONTRACT NUMBER	
				5b. GRANT NUMBER W81XWH-07-1-0247	
				5c. PROGRAM ELEMENT NUMBER	
6. AUTHOR(S) Daqing Piao, Ph.D.  E-Mail: daqing.piao@okstate.edu				5d. PROJECT NUMBER	
				5e. TASK NUMBER	
				5f. WORK UNIT NUMBER	
7. PERFORMING ORGANIZATION NAME(S) AND ADDRESS(ES)  Oklahoma State University Stillwater, OK 74078				8. PERFORMING ORGANIZATION REPORT NUMBER	
9. SPONSORING / MONITORING AGENCY NAME(S) AND ADDRESS(ES) U.S. Army Medical Research and Materiel Command Fort Detrick, Maryland 21702-5012				10. SPONSOR/MONITOR'S ACRONYM(S)	
				11. SPONSOR/MONITOR'S REPORT NUMBER(S)	
12. DISTRIBUTION / AVAILABILITY STATEMENT Approved for Public Release; Distribution Unlimited					
13. SUPPLEMENTARY NOTES					
14. ABSTRACT No abstract provided.					
15. SUBJECT TERMS No subject terms provided.					
16. SECURITY CLASSIFICATION OF:			17. LIMITATION OF ABSTRACT	18. NUMBER OF PAGES	19a. NAME OF RESPONSIBLE PERSON
a. REPORT	b. ABSTRACT	c. THIS PAGE			USAMRMC
U	U	U	UU	93	19b. TELEPHONE NUMBER (include area code)

## Table of Contents

	<u>Page</u>
Introduction.....	01
Body.....	01
Key Research Accomplishments.....	13
Reportable Outcomes.....	14
Conclusion.....	15
References.....	15
Appendices.....	17

# **ANNUAL REPORT**

## **PCRP 060814----“Transrectal Near-Infrared Optical Tomography for Prostate Imaging”**

### **INTRODUCTION**

The objective of this research is to explore the technology of trans-rectal near-infrared (NIR) optical tomography for accurate, selective prostate biopsy. Prostate cancer is the most common non-dermatologic cancer in American men. Prostate cancer suspicion is typically based on an elevated serum prostate-specific antigen (PSA) level or a suspicious nodule found during a digital rectal exam (DRE). When the PSA level is elevated or the DRE shows abnormal, there is a 25 % chance that cancer is present. The existence of prostate cancer can only be confirmed by a needle biopsy that is guided by trans-rectal ultrasound (TRUS). Since there are no pathognomonic findings for prostate cancer on ultrasound imaging, biopsies are taken following a systematic pattern throughout the prostate with preference given to the peripheral zone wherein most cancer are found. The accuracy of biopsy is questionable and many men undergo multiple biopsies due to the lack of a more specific/sensitive imaging modality. Pathologic studies have demonstrated positive correlation between increased micro-vessel density and the onset of the disease. Near-infrared (NIR) optical tomography is known of sensitive to blood-based contrast, therefore trans-rectally implemented NIR optical tomography may provide a new way of assessing the prostate cancer. One of the outcomes of trans-rectal NIR tomography of the prostate would be a more accurate imaging guidance for targeted prostate biopsy.

### **BODY**

#### **1. Proposed Specific Aims:**

- (1) To demonstrate that endoscopic NIR tomography at a probe size of 25mm in diameter can be achieved by use of spread-spectral-encoding from a broad-band light source.
- (2) To demonstrate that trans-rectal NIR tomography can image the prostate at the proximity of the rectum with significant tumor-tissue contrast.
- (3) To demonstrate that multi-spectral trans-rectal NIR tomography can be implemented with the single trans-rectal imaging probe.
- (4) To demonstrate that trans-rectal multi-spectral NIR tomography can quantify the hemoglobin concentration and oxygenation saturation in phantom, and further in prostate tumor model if the time of research allows.

#### **2. Progresses toward trans-rectal ultrasound-coupled near-infrared optical tomography**

In the 1<sup>st</sup> year of this research (Mar, 2007—Feb. 2008), we have successfully developed an axial-imaging 20mm diameter trans-rectal NIR tomography probe which is equivalent in size to a standard trans-rectal ultrasound (TRUS) probe. Calibrations and simulations were conducted to evaluate the imaging capabilities of this axial-imaging probe, and it was found that the imaging-depth of this axial probe may be limited to 15mm [Musgrove 2007]. *In vivo* axial trans-rectal imaging using this probe has been conducted on healthy canine prostate as shown in Fig. 1. For this study a planar array trans-rectal US probe was used to evaluate the location and ultrasonic structure of the prostate prior to imaging with this stand-alone axial-imaging NIR probe. The depth of imaging the prostate tissue seemed to be at the 1cm range. The tissue being imaged was therefore primary the peripheral tissue. The limited imaging depth may be caused partially by the axial-imaging geometry, and partially by the strong absorption of prostate tissue.

We have since investigated the approach of sagittal-imaging trans-rectal NIR optical tomography which has the potential of interrogating deeper tissues, and developed TRUS-coupled NIR tomography for concurrent multimodality trans-rectal NIR/US imaging.

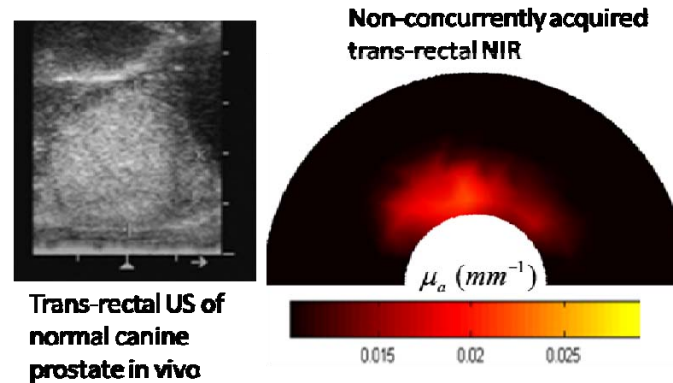


Figure 1. Axial trans-rectal NIR optical tomography of normal canine prostate *in vivo*. The absorption value of the prostate tissues agrees with that in Fig. 4.

## 2.1 Principle of trans-rectal NIR/US

The schematic configuration of our trans-rectal NIR/US prostate imaging is illustrated in Fig. 2. In order to interrogate deep prostatic tissues, it is necessary to have longitudinally distributed NIR arrays because the NIR imaging depth is approximately  $\frac{1}{2}$  of the array dimension. By arranging the longitudinal NIR arrays symmetrically on the lateral sides of the sagittal US transducer, the correlation between the NIR imaging and sagittal US can be made. The NIR arrays could have a number of optode configurations. However, the design of having sources or detectors exclusively on one of the two NIR arrays is adopted after evaluating the performance, the endo-rectal applicability, and the prototyping challenge [Xu et al, 2008].

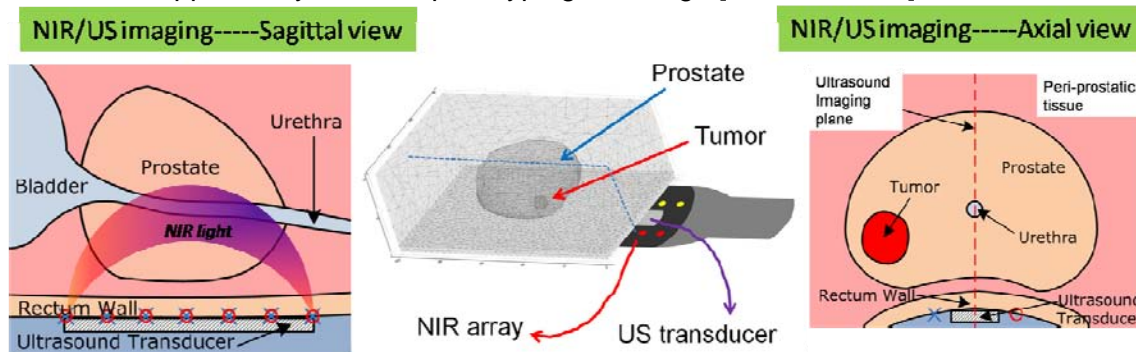


Figure 2. Illustration of trans-rectal NIR/US of the prostate. Trans-rectal US is placed in the middle of the trans-rectal NIR applicator (optodes distributed longitudinally) to perform combined NIR/US imaging.

The completed trans-rectal NIR/US probe and imager are shown in Fig. 3. The probe was developed based on the ALOKA Veterinary US unit. The NIR applicator was integrated over the intact 7.5MHz sagittal-imaging transducer of the bi-plane ALOKA trans-rectal US probe. The ALOKA US probe also had a 5MHz axial-imaging transducer. The NIR probe consisted of one source and one detector array separated laterally 20mm and placed symmetric to the sagittal US transducer. The NIR source and detector array, each having 7 channels, were 60mm in longitudinal dimension, which was identical to the longitudinal imaging view of the sagittal US transducer. Each NIR optode channel had a micro prism-lens pair for coupling the

light to and from the probe surface. The NIR light from a super-luminescent diode of 100mW at 840nm was focused sequentially onto 7 source fibers of the NIR applicator by a home-made translating fiber multiplexer. The NIR remissions collected by the 7 detection fibers were acquired by a 16-bit intensified CCD camera through a spectrometer. Acquisition of signals for all 7 source channels usually took 5 seconds after the prostate was localized on the sagittal trans-rectal US. An Aloka-900 (in our lab) or Aloka-3500 (belonging to OSU Vet-Med) US scanner acquired the bi-plane US images, of which the sagittal US had accurate position correlation with the trans-rectal NIR. The absorption and reduced scattering images of the prostate were reconstructed from steady-state measurements [Farrell 1992] using non-linear optimization method [Xu, 2005, Iftimia 2000, Jiang et al, 2008].

Using this probe/imager, trans-rectal NIR/US has been performed on normal and diseased canine prostate *in vivo*. Dogs have been previously used for prostate studies because of the similarity between canine and human prostate glands [Hazle 2002; Forsberg 2002; Rivera 2005]. We have successfully developed a canine prostate tumor model in OSU Center for Veterinary Health Sciences with this New Investigator. This study was approved by the university's Institutional Animal Care and Use Committee. The protocol was also approved and underwent an on-site inspection by the US Army Medical Research and Material Command. In the following sections we will discuss the results obtained from normal canine prostate and canine prostate cancer models. It should be noted that all the *in vivo* NIR images presented were reconstructed purely from NIR signal, without any US *priori* information.

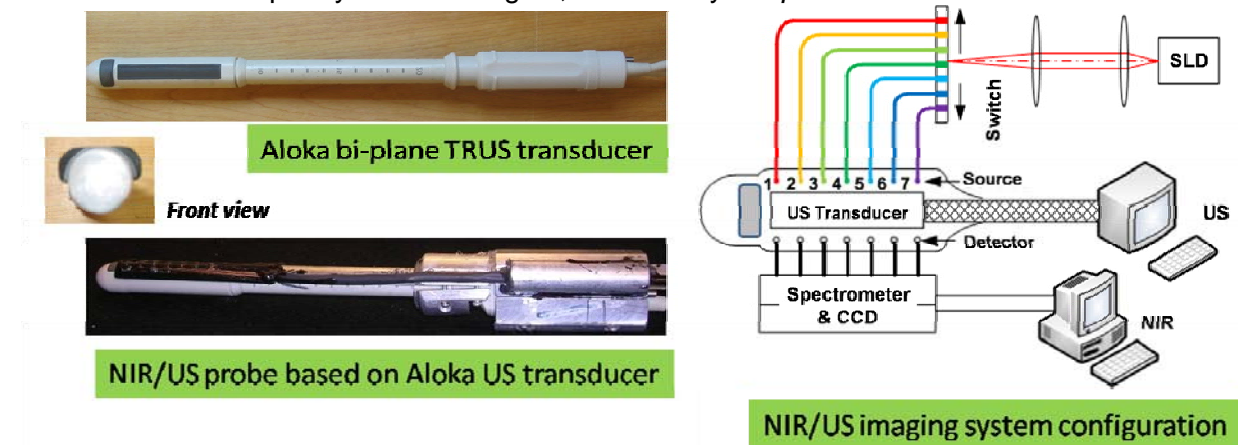


Figure 3 (Left). Photograph of the Aloka trans-rectal US transducer and the completed NIR/US probe used for canine imaging. (Right) Schematic diagram of the trans-rectal NIR/US imaging system that consists of a custom-built NIR imager and a commercial ALOKA SSD-3500 US scanner.

## 2.2. *In vivo* trans-rectal NIR/US of normal canine prostate

Figure 4 displays the trans-rectal NIR/US imaging results performed on normal canine prostate *in vivo*. The sagittal US was conducted at the middle of the right lobe, the middle-line of the prostate gland, and the middle of the left lobe. The trans-rectal NIR images were in 3-dimension but only the sagittal plane aligned with the US were displayed here. The NIR images were for absorption coefficient and reduced scattering coefficient, respectively. The prostate was shown as hyper-absorbing (as prostate is more vascular), and slightly hyper-scattering, with respect to the peripheral tissues. The absolute values as well as the large ranges of the absorption and reduced scattering coefficients of the prostate agree with the values reported in literatures [Svensson et al, 2007 reviewed optical properties of human prostate].

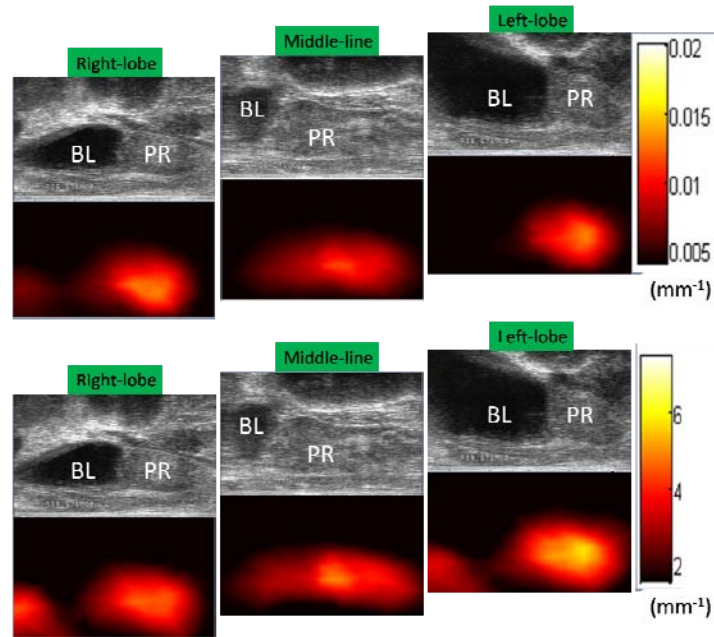


Figure 4. Trans-rectal NIR/US of normal canine prostate in vivo: The US images were taken at the right lobe, middle-line, and the left lobe. (Left), US/NIR absorption; (right) US/NIR reduced scattering. The dimensions of the images are 50mmx30mm (cranial-caudal x dorsal-ventral).

### 2.3. In vivo trans-rectal NIR/US of transmissible venereal tumors in canine pelvic canal

We have developed a canine prostate cancer model using canine transmissible venereal tumor (TVT). The unique canine TVT is a round cell tumor of dogs that mainly affects the external genitalia and can be transmitted from animal to animal during copulation, regardless of histocompatibility. The neoplastic cells are generally thought to be of histiocytic origin [Mozos et al, 1996]. TVT cells can be propagated in immunocompromised (SCID) mice and transferred to different tissues (such as the prostate gland) of the dog to result in a neoplastic mass effect useful for imaging studies [Rivera 2005]. For these studies, an existing TVT cell line was obtained as cryopreserved tissue from MD Anderson Cancer Center (Houston, TX). The tumor tissue was quick-thawed, homogenized and inoculated into the subcutis of a NOD/SCID mouse. After approximately 12 weeks, the tumor reached an appropriate volume ( $4.0\text{-}4.5\text{cm}^3$ ) for recovery and were processed and inoculated into a second NOD/SCID mouse. Following growth in the second mouse (8 weeks), the neoplastic cells were recovered and homogenized for inoculation into the canine prostate gland.

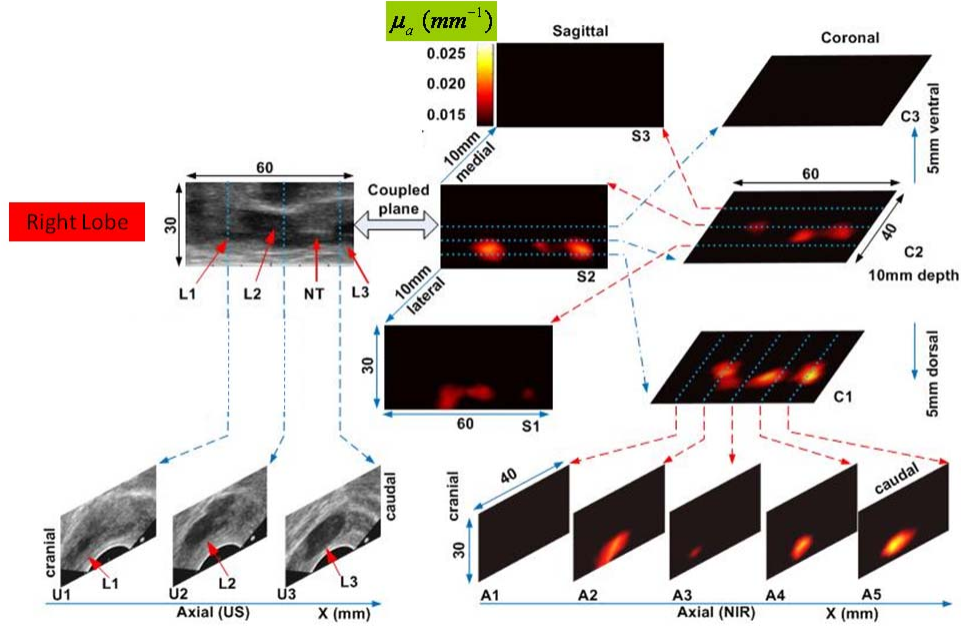
A 12 kg sexually intact adult Beagle dog estimated to be approximately 4 years of age was housed and administered using general anesthesia for TVT cell injection. A 6-inch 16 gauge hypodermic needle was inserted transperineally into the right lobe of the prostate where ~3 cc of the prepared TVT cells were injected. During retraction of the injection needle, it was considered unavoidable that TVT cells would leak from the prostate injection site and be "seeded" along the needle insertion tract. The dog was examined weekly by US using the trans-rectal NIR/US probe covered by condom as did with standard trans-rectal US. During the first two weeks following TVT cell injection there was no evidence of tumor growth on US and rectal examination. The next US examination occurred 5 weeks post-injection when hypoechoic masses were observed both in the prostatic parenchyma and peri-prostatically around the right lobe of the prostate. The dog underwent weekly trans-rectal US monitoring for 2 more weeks, and was then humanely euthanized 8 weeks after the initial TVT cell injection for a complete necropsy and histological examination of prostate and peri-prostatic tissues.

The NIR absorption and reduced scattering images taken at 5 weeks post-injection are displayed in Fig. 5(a) and (b), respectively. The US and NIR images have the same dimension of 60mm×30mm (cranial-caudal×dorsal-ventral) for sagittal, 40mm×30mm (right lateral–left lateral×dorsal-ventral) for axial, and 60mm×40mm (cranial-caudal×right lateral–left lateral) for coronal views, respectively. The sagittal trans-rectal US images were taken at the middle portion of the right lobe. The hypo-echoic region L1 indicates an intra-prostatic mass. The large hypo-echoic region L2 indicates a mass ventral and caudal to the prostate that may have connection with L1. The NT on the right lobe US image denotes the needle trajectory for introducing the TVT cells. Longitudinal hypo-echoic regions including L3 are seen along the NT. The hyper-absorptive regions on sagittal NIR images correspond to L1, L2, and L3 on sagittal US image. The 10mm-medial NIR image displays the absorptive masses at reduced NIR contrast, and the 10mm-lateral NIR reveals connected strong absorptive masses. The bladder is seen as slightly hypo-echoic at other medial sagittal US images (not shown here); however, no hyper-absorptive mass corresponding to the bladder is presented at the left-most region of the sagittal NIR images. The three axial TRUS images were taken at the cranial edge of the prostate crossing L1, the caudal edge of the prostate crossing L2, and the peri-rectal region crossing L3. The axial US images show a small hypo-echoic intra-prostatic mass at cranial side of the prostate, the distortion of the right lobe boundary and extending of the L2 over the prostate mid-line that correlates with the findings on mid-line sagittal US (shown in Fig. 6), and large peri-rectal hypo-echoic mass cranial to the perineum. The locations of axial NIR images are comparable to those of the axial trans-rectal US. The axial NIR image A2 should contain L1, and the axial NIR image A5 should contain L3. The coronal NIR images correspond to 5mm, 10mm, and 15mm ventral to the rectum. The no-show of the lesions on the 15mm coronal image is due to the decreased NIR sensitivity of side-firing and the reconstruction without any spatial *prior*. The hyper-absorptive mass indicative of L1 is seen medial to the hyper-absorptive masses indicative of L2 and L3. The appearance of the NIR hyper-absorptive masses in 3-views agrees with that of the US hypo-echoic regions in 2-views.

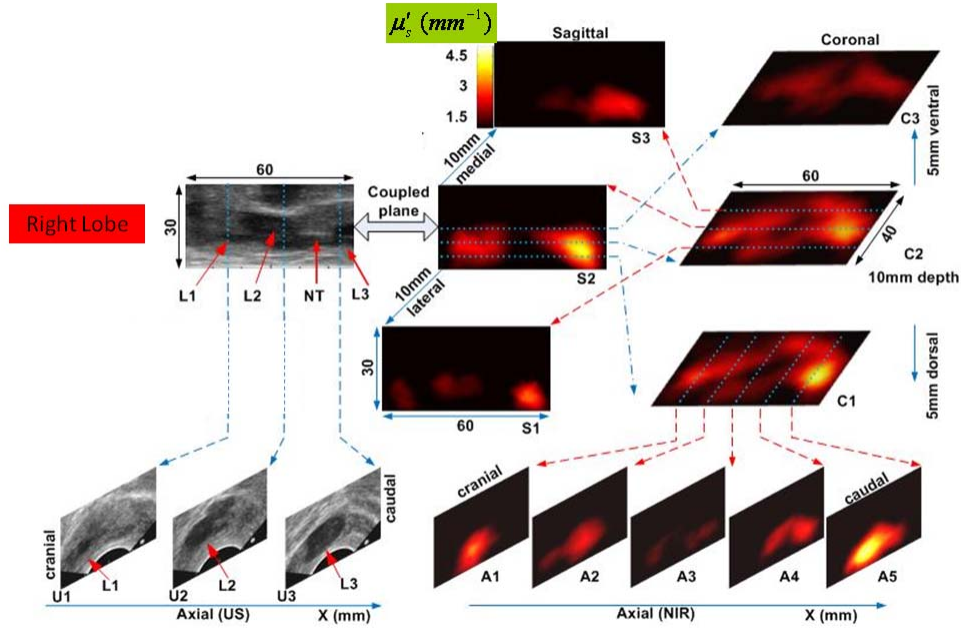
The hyper-absorptive masses in (a) being suspicious of TVTs are shown in (b) with different contrast patterns for the reduced scattering coefficient. In the NIR scattering images, L3 has much higher contrast than do the other masses corresponding to L1 and L2. The contrast elsewhere is also more homogenous compared with that in the absorption image.

In Fig. 6 we present the retrospective comparisons of the trans-rectal US and the NIR images obtained at the middle of the right lobe, the middle-line of the prostate, and the middle of the left lobe, before the TVT injection, 2 weeks after the TVT injection when the US and rectal examination showed no evidence of tumor growth, and 5 weeks after the TVT injection when the tumor growth was evident on both US and rectal examination. Both the absorption and reduced scattering images, correlating to the same set of US images, are shown. At the 2-week NIR absorption images, hyper-absorptive regions were found dorsal to the prostate in the right lobe only, and dorsal to the pelvic bone in the right lobe with potential extension to the middle line. The locations of these hyper-absorptive regions correlated very well with those of the hypo-echoic and hyper-absorptive regions found in week-5. The NT in week-5 US image indicated the needle track for injecting the tumor cells. The dimensions and contrasts of the hyper-absorptive regions implied a tumor growing in right lobe and extending toward the middle-line. The growth of the tumor was indicated earlier by the absorption images of trans-rectal NIR than by the trans-rectal US. The growth of the tumor on reduced scattering images, although not as evident as in the absorption images, did correlate with the findings in trans-rectal US. It is evident that combining the information of trans-rectal US and trans-rectal NIR renders earlier and much more accurate findings of the tumor growth.



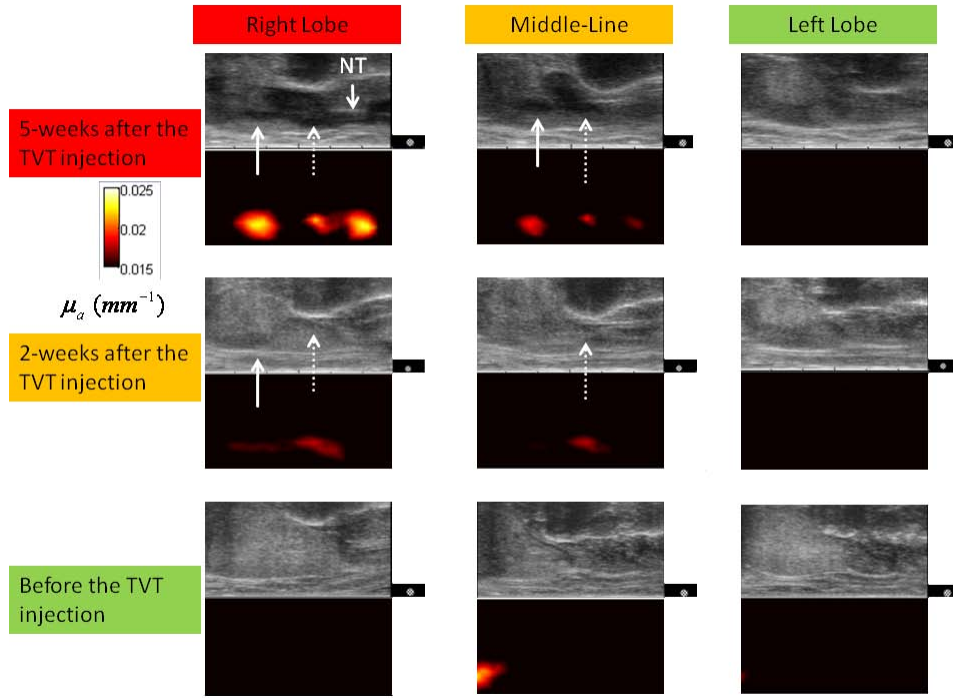


(a)

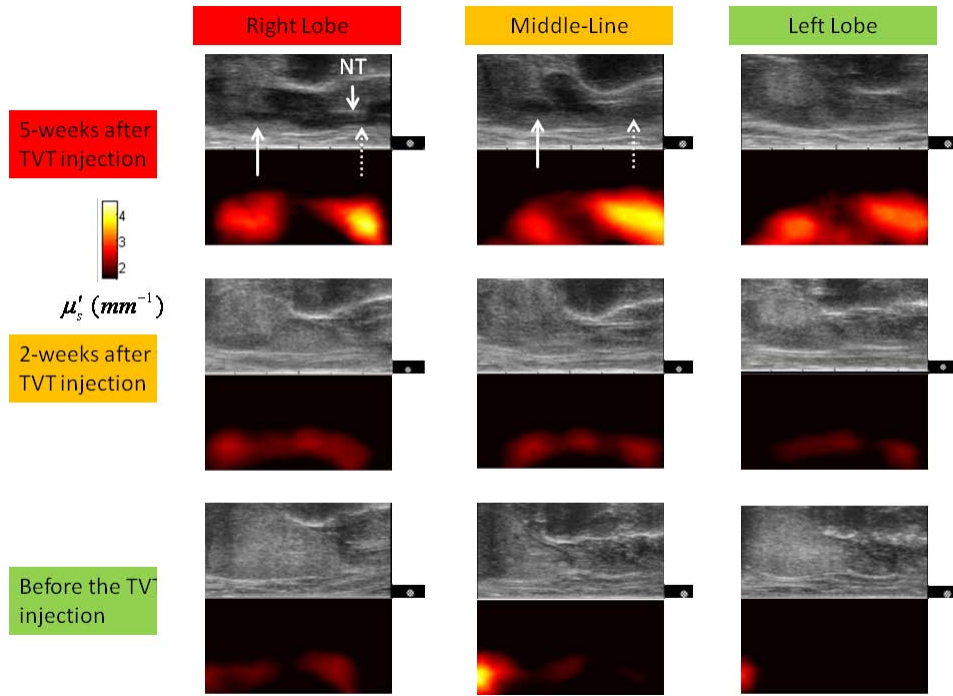


(b)

Figure 5 TVTs developed in canine pelvic canal assessed by trans-rectal NIR and US *in vivo* at 5-weeks post TVT-injection. The NIR images are in sagittal, axial, and coronal views. The US images are in sagittal and axial views. The dimensions of the images are: 60mm×30mm (cranial-caudal×dorsal-ventral) for sagittal, 40mm×30mm (right lateral–left lateral×dorsal-ventral) for axial, and 60mm×40mm (cranial-caudal×right lateral–left lateral) for coronal views, respectively.



(a)



(b)

Figure 6 Comparison between the image-monitoring of TVT development in canine pelvic canal assessed by trans-rectal NIR and US *in vivo*, over a period of 5 weeks. The images were taken at the middle of the right lobe, the middle-line of the prostate, and the middle of the left lobe, before the TVT injection, 2 weeks after the TVT injection when the US and rectal examination showed no evidence of tumor growth, and 5 weeks after the TVT injection when the tumor growth was evident on both US and rectal examination.

The gross and histological findings (taken at 8-week after the TVT injection) given in Fig. 7 confirmed intra- and peri-prostatic neoplastic infiltrates with masses also located along the urethra and peri-rectal tissue; the latter related to dissemination along the needle track during TVT inoculation. All masses consist of diffuse sheets of a monomorphic population of neoplastic round cells dissecting through pre-existing fibrovascular stroma. The neoplastic cells have large hyperchromatic nuclei, single conspicuous nucleoli and moderate amounts of featureless cytoplasm. The cytological features are consistent with canine transmissible venereal tumor (TVT).

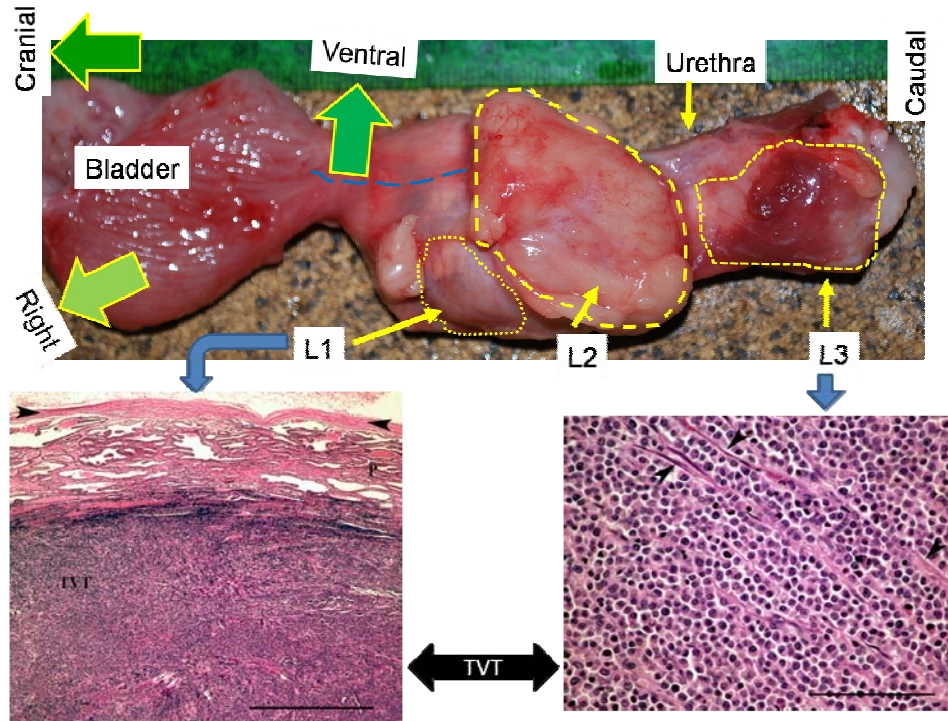


Figure 7. (Top) Postate gland taken after removal of the urinary bladder and intra-pelvic urethra immediately following euthanasia. The prostate gland is markedly expanded and misshapen secondary to intra-prostatic (L1) and peri-prostatic (L2) neoplastic masses. Neoplastic masses were also distributed along the distal intra-pelvic urethra (L3) and in the peri-rectal subcutaneous tissues (not shown). Histologically, expansile masses of transmissible venereal tumor cells (TVT, bottom left panel) displace and compress prostatic tissue (P). Prostatic capsule (arrowheads), Bar = 230 $\mu$ m. The TVT infiltrate (bottom right panel) consists of sheets of neoplastic round cells dissecting through pre-existing fibrovascular stroma (arrowheads), Bar = 300 $\mu$ m.

Among the US hypo-echoic masses obtained in week-5, the L1 was intra-prostatic, the L2 was largely ventral to the prostate, and the L3 was caudal to the prostate. These 3 masses were shown at similar depths on NIR images, which was partially due to the depth-dependent NIR sensitivity [Xu et al, 2008] and partially due to the large volume of diffuse photon interrogation with the tumor. Despite the depth inaccuracy, the TVT nodules had been detected by use of trans-rectal NIR alone. If the image reconstruction of trans-rectal NIR could be guided by the US structural information of the prostate (and the tumor if the tumor is visible to US), the characterization of the TVT nodules on NIR would become more accurate.

It is known that most prostate cancers are presented as multi-focal [Wise et al, 2002]. It must be noted that the intraprostatic TVT tumors were initiated in a non-immunosuppressed canine model on which the TVT nodules developed at multiple sites intra-prostatically and peri-

prostatically. Although not all of the TVT tumors were confined to the prostate, the successful imaging of multiple TVT nodules by trans-rectal NIR tomography implies the utility of detecting multiple intra-prostatic tumors. On trans-rectal US all of the TVT tumor nodules developed in this subject were shown strongly hypo-echoic that correlated with the strongly hyper-absorptive and moderately hyper-scattering findings on NIR imaging. The bladder, on the other hand, showed as hypo-echoic on US; however it was shown as iso-absorptive or iso-scattering on NIR. This suggests that trans-rectal NIR tomography has higher specificity in imaging the regions hypo-echoic to TRUS.

The feature of TVT as strongly hyper-absorptive on NIR tomography is likely due to the hyper-chromatic nuclei unique to TVT. The relatively higher scattering of the TVT may be due to the hyper-density and larger nuclei of the neoplastic cells [Wang et al, 2006]. As the neoplastic cells are arranged into microlobules by the pre-existing fibrovascular stroma, the TVT may also present certain polarization-sensitivity. Overall, the characteristic features of TVT on NIR tomography are comparable to those of breast cancer angiogenesis on NIR. The micro-architecture of spontaneous prostate cancer may be different from that of TVT. So the intrinsic NIR contrast of human prostate cancer may not be as pronounced as those of TVT, but it can be expected that the human prostate cancer will have notable contrast on trans-rectal NIR tomography if the contrast is taken for hemoglobin concentration, and oxygenation saturation. These contrasts, which are difficult for trans-rectal US to acquire, could help to characterize the malignancy of the prostate lesions.

#### **2.4. Detecting single prostate cancer using the prototype NIR/US probe---simulation studies**

We have also conducted simulation studies on the performance of prostate cancer detection using the above-mentioned prototype NIR/US probe and a prior-guided NIR reconstruction method developed specifically for prostate NIR tomography [Xu et al, 2008]. The purpose was to evaluate the detectability of the cancer when it shows conspicuous on US, therefore it was assumed that the morphological information of the prostate and lesion was available from trans-rectal US. This is not entirely representative of the actual clinical cases as many cancers are not visible on trans-rectal US, but it will provide valuable insights. Trans-rectal US images of human prostate available in open sources were used for the simulation study. The TRUS image was first converted to COMSOL Multiphysics compatible format. The prostate tumor is mimicked using a spherical shape to allow for flexibility of adjusting its size. The absorption and reduced scattering coefficients of the rectum, peri-prostate tissue, prostate and the tumor are assigned with values as suggested by literature [Li, 2007].

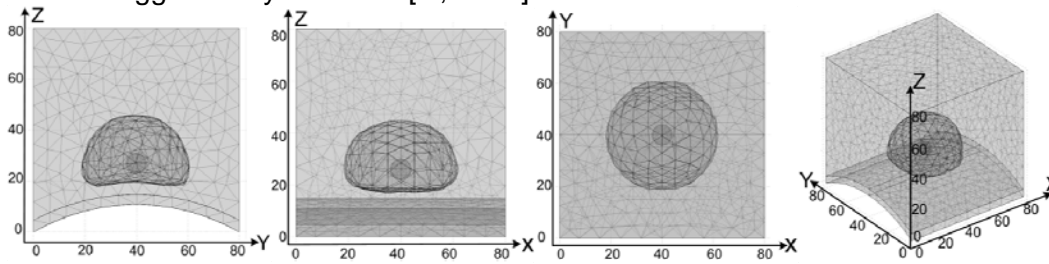


Figure 8 Finite-element mesh of the prostate for simulation

Figure 8 illustrates one example of the completed FEM-mesh for trans-rectal NIR optical tomography derived from a trans-rectal US image, where x, y and z denote the longitudinal, lateral and the depth coordinates, respectively. A typical mesh used for this work contains



approximately 4000 nodes and 20000 linear tetrahedral elements. The mesh in the figure corresponds to a volume of  $80 \times 80 \times 80 \text{ mm}^3$  and the 'walnut' shaped prostate has a dimension of  $50 \times 50 \times 30 \text{ mm}^3$ . The rectum wall is 4mm thick with a curvature radius of 80 mm. The choice of the curvature radius is due to the fact that the NIR array added to a TRUS probe may have a flat surface that would transform the rectum lumen to an elliptical shape. The source modulation frequency is set at 100MHz, and 1% Gaussian noise is added to all forward calculations to form the measurement data. Comparisons of detection sensitivity are made between the prototype probe of 7sd (indicating 7 source or detector on one lateral side of US) and an NIR probe of 26ssdd (indicating 26 source or detector—separated to 2 lines--on each lateral side of US), both having 6cm span of NIR array.

#### 2.4.1 Reconstruction accuracy versus target longitudinal location

A target of 10mm in diameter is placed at the middle-sagittal plane of  $y=40\text{mm}$ ,  $z=26\text{mm}$ , and varied in longitudinal coordinates from  $x=25$  to  $55\text{mm}$  with a step of  $5\text{mm}$  (Fig. 9(a)). The optical properties reconstructed by the two geometries are plotted versus the true values in Fig. 9(b) and (c). The optical properties recovered by 26ssdd and 7sd are close to each other at most of the longitudinal locations, but the 7sd design shows a larger variation in the recovered absorption contrast at  $x=30\text{mm}$  and  $x=50\text{mm}$  compared to other positions. This may be related to fewer source-detector pairs that contribute to the target detection when close to the boundary or the existence of any irregular elements in the mesh.

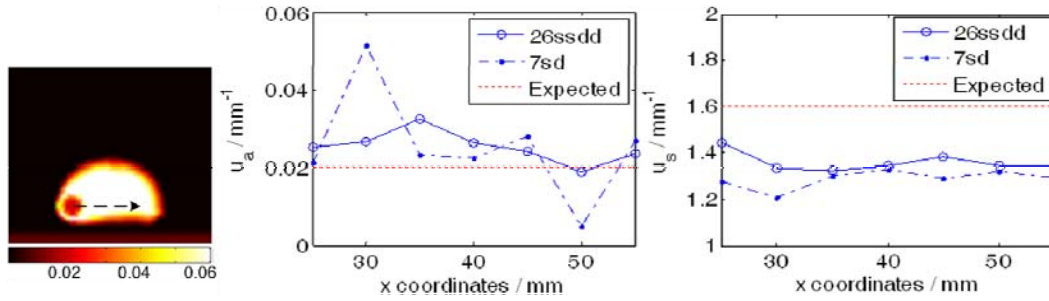


Figure 9 Comparison of two geometries for a target varying in longitudinal location in the middle-sagittal plane: (a) illustration of the target location change [Unit:  $\text{mm}^{-1}$ ]; (b) comparison of absorption coefficient reconstruction; (c) comparison of reduced scattering coefficient reconstruction

#### 2.4.2 Reconstruction accuracy versus target depth

A target of 10mm in diameter is placed at the middle-sagittal plane at  $x=40\text{mm}$ ,  $y=40\text{mm}$ , and the depth is varied from  $z=25$  to  $40\text{mm}$  at a step of  $2.5\text{mm}$  (the last data point is simulated at  $z=39\text{mm}$  as at  $40\text{mm}$  the target is out of the prostate) (Fig. 10(a)). The reconstructed optical properties are plotted in Fig. 10(b) and (c). The 26ssdd configuration outperforms the 7sd one again, however beyond  $z=30\text{mm}$ , both designs are incapable of recovering the absorption coefficient of the target from the prostate background. This depth limitation is related to the maximum span of the NIR array, the large absorption coefficient ( $0.06\text{mm}^{-1}$ ) of the prostate, and the size of the target. For a larger target with a diameter of  $14\text{mm}$ , it is verified that the target may be resolved up to  $36\text{mm}$  depth from the NIR array in comparison to  $30\text{mm}$  for a target of  $10\text{mm}$  diameter. A potentially smaller absorption coefficient of intact prostate may also increase the depth limit of target detection due to an increase in the depth sensitivity.

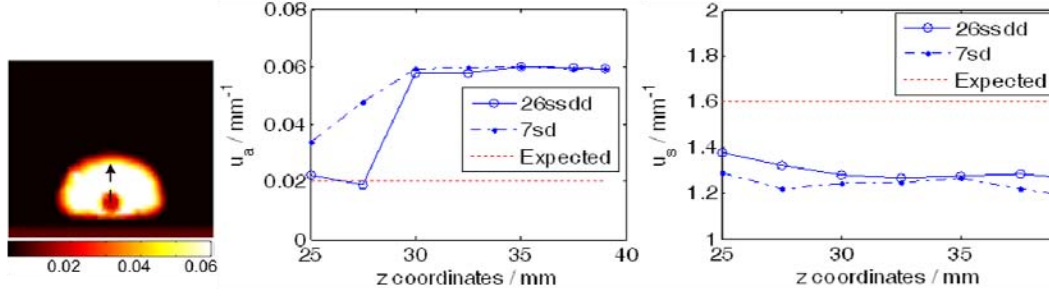


Fig. 10 Comparison of two geometries for a target varying in depth in the middle-sagittal plane: (a) illustration of the target location change [Unit: mm<sup>-1</sup>]; (b) comparison of absorption coefficient reconstruction; (c) comparison of reduced scattering coefficient reconstruction

#### 2.4.3 Reconstruction accuracy versus target size

A target is placed at middle-sagittal plane of  $x=40\text{mm}$ ,  $y=40\text{mm}$  and  $z=26\text{mm}$ , and the diameter of the target is varied from 4mm to 14mm with a step of 1mm. The change of the target diameter is illustrated in Fig. 11(a). The reconstructed optical properties are shown in Fig. 11(b) and (c). It is clear that the larger the target, the better the accuracy of reconstruction. The 26ssdd can recover the absorption contrast of the target when the diameter is greater than 6mm and the 7sd can recover the target for target diameter greater than 8mm. These comparisons suggest that the accuracy of recovering the absorption properties is strongly dependent on the number of NIR optodes, which weakly affects that of scattering properties.

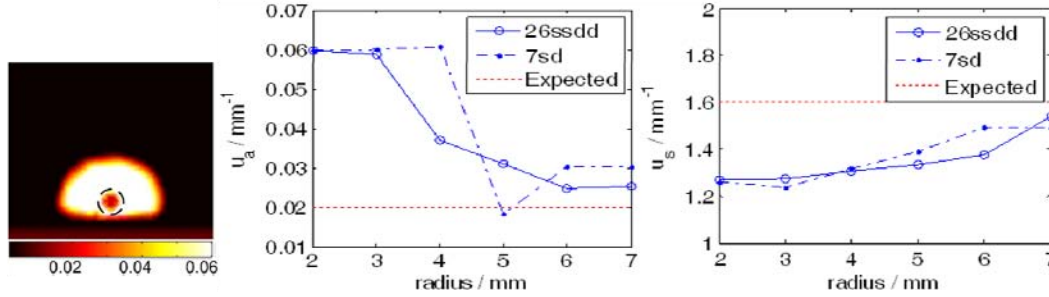


Fig. 11 Comparison of two geometries for a target varying in size in the middle-sagittal plane: (a) illustration of the target size change [Unit: mm<sup>-1</sup>]; (b) comparison of absorption coefficient reconstruction; (c) comparison of reduced scattering coefficient reconstruction

### 2.5. Detecting dual-center prostate cancer using the prototype NIR/US probe---simulation studies

Capability of differentiating two targets is of particular relevance to prostate cancer imaging owing to the existence of secondary or multifocal tumors. In this section, we investigate only the case of having two targets in the same sagittal plane and conduct the simulations with the 7sd probe design only.

#### 2.5.1 Reconstruction of two targets located at the same depth in sagittal plane

Figure 12 shows two 10mm-diameter regions being added to the prostate, at coordinates (25, 40, 26) and (55, 40, 26), respectively. In (a) only one region has optical contrast, and in (b) both regions have optical contrasts. In both cases the optical contrast can be reconstructed with

good accuracy. The  $\mu_a$  of the target with true optical contrast is reconstructed within  $\pm 20\%$  of the set value and  $\mu_s'$  can be reconstructed within  $\pm 23\%$  of the set values. The target with no optical contrast is reconstructed with some artifacts, nevertheless, the target with optical contrast can be easily differentiated from the one without.

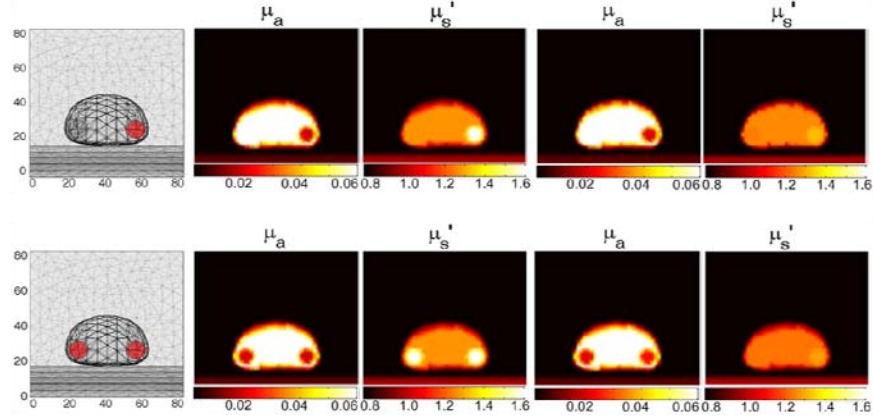


Fig. 12 Two suspicious regions at the same depth [Units: mm and  $\text{mm}^{-1}$ ]

### 2.5.2 Reconstruction of two targets located at different depth in sagittal plane

Two targets of 10mm diameter are added in the prostate at coordinates of (25, 40, 28) and (55, 40, 24), respectively. Figure 13 shows the reconstructed images for the case of both targets having negative contrast.

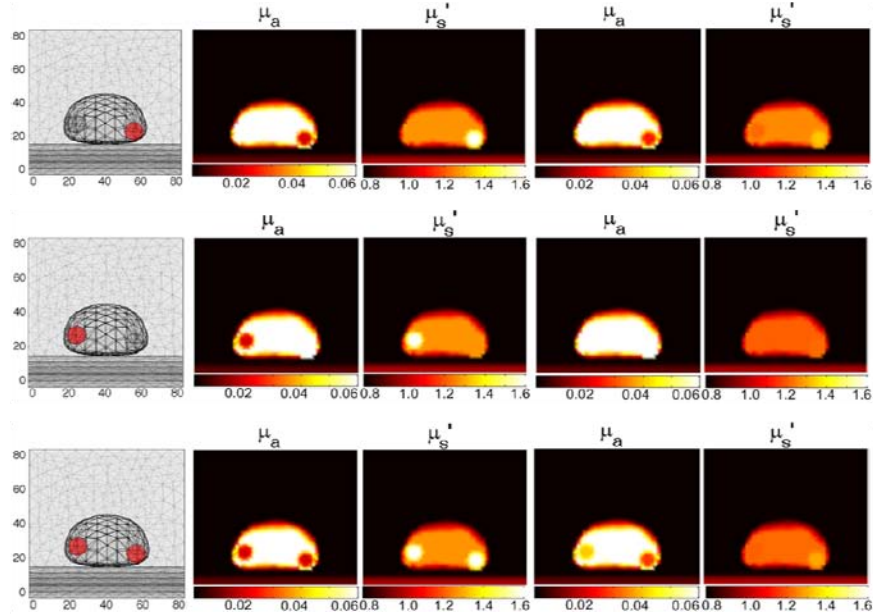


Fig. 13 Two targets at different depths: negative tumor contrast cases  
[Unit: mm and  $\text{mm}^{-1}$ ]

When the target is at a depth of 24mm, the  $\mu_a$  and  $\mu_s'$  can be reconstructed within  $\pm 20\%$  and  $\pm 25\%$  of the set values, respectively. However, a target at 28mm depth cannot be reconstructed. This is due to the high absorption coefficient of the prostate set at  $0.06\text{mm}^{-1}$ .

When the prostate absorption coefficient is reduced to  $0.006\text{mm}^{-1}$  which will provide positive optical contrast in the two target regions, both targets can be recovered as shown in Fig. 14. The  $\mu_a$  of the target can be reconstructed within  $\pm 5\%$  of the set value, while the  $\mu_s$  is still reconstructed within  $\pm 23\%$  of the expected values.

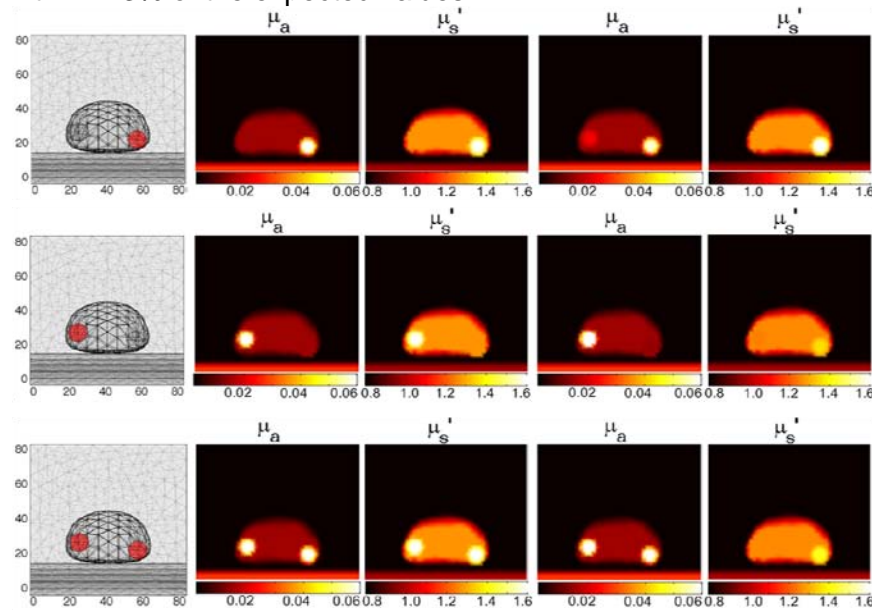


Fig. 14 Two targets at different depths: positive tumor contrast cases [Unit: mm and  $\text{mm}^{-1}$ ]

## KEY RESEARCH ACCOMPLISHMENTS

The following research accomplishments have been made during the 2<sup>nd</sup> year of this project:

1. The 20mm diameter axial-imaging trans-rectal NIR tomography probe has been tested on imaging healthy canine prostate *in vivo*. Prostate tissues in the peripheral zone were imaged and reconstructed with optical contrasts agree with literature values.
2. A TRUS-coupled trans-rectal NIR tomography probe has been developed. The combined probe performs sagittal US and NIR imaging concurrently. The NIR imaging at the middle-sagittal plane correlates with the TRUS image.
3. *In vivo* trans-rectal NIR/US imaging of normal canine prostate has been demonstrated.
4. A canine prostate tumor model has been developed using canine TVT cells. We now have a reproducible large animal prostate tumor model.
5. *In vivo* trans-rectal NIR/US imaging of canine TVT development has been demonstrated. There is evidence that when TRUS is aided by trans-rectal NIR, the tumor development can be detected earlier and more accurately.
6. Quantitative evaluation of the imaging performance of the combined trans-rectal NIR/US imaging has been conducted by simulation. The evaluation includes both detecting single tumor and multi-centric tumors.



## REPORTABLE OUTCOMES

The progress in the 2<sup>nd</sup> year of this project has results in following publications or manuscripts:

### Provisional Patent Applications

1. Daqing Piao, Zhen Jiang, Guan Xu, Charles F. Bunting, "Method and Apparatus for combined/concurrent trans-channel near-infrared optical tomography and ultrasound for imaging internal organs", US provisional patent application, #61/144,556, filed on Jan. 16, 2009.

### Journal Papers

1. Jiang Z, **Piao D**, Xu G, Ritchey JW, Holyoak GR, Bartels KE, Bunting CF, Slobodov G, Krasinski JS, "Trans-rectal ultrasound-coupled near-infrared optical tomography of the prostate Part II: Experimental demonstration," *Optics Express*, 16(22): 17505–17520 (2008). [PubMed index: 18958031].
2. Xu G, **Piao D**, Musgrove CH, Bunting CF, Dehghani H, "Trans-rectal ultrasound-coupled near-infrared optical tomography of the prostate Part I: Simulation," *Optics Express*, 16(22): 17484–17504 (2008). [PubMed index: 18958030].

### Proceeding Papers and Conference Presentations

3. Jiang Z, Ritchey JW, Holyoak GR, Bartels KE, Xu G, Bunting CF, Slobodov G, Krasinski JS, Piao D, "In vivo trans-rectal ultrasound coupled trans-rectal near-infrared optical tomography of canine prostate bearing transmissible venereal tumor," *Proceedings of SPIE*, Vol. 7174, Paper #71741U..
4. Xu G, Bunting CF, Dehghani H, Piao D, "A hierarchical spatial prior approach for prostate image reconstruction in trans-rectal optical tomography," *Proceedings of SPIE*, Vol. 7171, Paper #71710S.
5. Jiang Z, Piao D, Krasinski JS, "Development of a continuous-wave dual-band trans-rectal optical tomography system for concurrent sagittal imaging with trans-rectal ultrasound," *Proceedings of SPIE*, Vol. 7171, Paper #71710G.
6. Piao D, Holyoak GR, Bartels KE, Ritchey JW, Jiang Z, Xu G, Bunting CF, "In vivo trans-rectal optical tomography of normal canine prostate---demonstration of optical contrast of intact prostate over its peripheral tissue," *Saratov Fall Meetings 2008*, Saratov, Russia, Sep. 23-26, 2008 (**Internet session invited lecture**).

### Students Fully or Partially Supported During The 2nd Year:

1. JIANG, Zhen                      PhD student
2. XU, Guan                        PhD student
3. Mukherjee, Sovanlal        PhD student
4. XIE, Hao                        MS degree in May, 2008.

### Grants Being Awarded That Can Be Attributed To This Research:

1. Big XII Faculty Fellowship Program ----- Faculty Fellow Award  
Piao, D (PI),                      02/2009----08/2009,                      \$2,500  
Title:                      Faculty Fellowship in University of Missouri, Columbia  
Objective:                This is a faculty fellowship award for visiting Big XII universities to enhance research collaborations.
2. Oklahoma EPSCoR ---- Research Opportunity Award  
Piao, D (Supporting PI),                      06/2009----08/2009,                      OSU- \$3,500

Jiang, Y (PI) University of Central Oklahoma (Total \$10,000)  
 Title: Advanced Reconstruction Method for Optical and Ultrasonic Imaging  
 Objective: This is a summer research opportunity award grant for faculties in Oklahoma regional universities to conduct research in Oklahoma research-intensive universities, including Oklahoma State University.

### 3. Oklahoma State University-----Technology Business Assessment Group (TBAG)

Piao, D (PI), 12/01/2008----11/30/2009, \$25,000  
 Title: Clinical Trans-rectal Optical Imaging Applicator for Prostate Biopsy  
 Objective: To develop a B&K ultrasound-coupled near-infrared optical imaging applicator for trans-rectal near-infrared tomography of human prostate for future clinical trials.

## CONCLUSIONS

The objective of this research is to explore the technology of trans-rectal near-infrared (NIR) optical tomography that may benefit accurate, selective prostate biopsy. The research in the 2<sup>nd</sup> year has made important advancements. The advancements include the invention of TRUS-coupled NIR tomography, the development of a canine prostate tumor model, the demonstration of TRUS-coupled NIR tomography of canine prostate tumor *in vivo*, and the establishment of preliminary evidence that augmenting the NIR imaging to the standard TRUS detects the prostate tumor earlier and with better accuracy. The proposed technology has advanced an important step, from trans-rectal NIR optical tomography to TRUS-coupled NIR optical tomography, toward clinical validations.

## REFERENCES

- Farrell TJ, Patterson MS, Wilson BC (1992), "A diffusion theory model of spatially resolved, steady-state diffuse reflectance for the noninvasive determination of tissue optical properties," *Med. Phys.* 19(4): 879-888.
- Forsberg F, Johnson DK, Merton DA, Li JB, Losco PE, Hagen EK, and Goldberg BB (2002), "Contrast-enhanced transrectal ultrasonography of a novel canine prostate cancer model," *J Ultrasound Med.*, 21(9), 1003-13.
- Hazle JD, Diederich CJ, Kangasniemi M, Price RE, Olsson LE, and Stafford RJ (2002), "MRI-guided thermal therapy of transplanted tumors in the canine prostate using a directional transurethral ultrasound applicator," *J Magn Reson Imaging.*, 15(4), 409-17.
- Iftimia N, and Jiang H (2000), "Quantitative optical image reconstruction of turbid media by use of direct-current measurements," *Appl. Opt.* 39, 5256-5261.
- Jiang Z, Piao D, Xu G, Ritchey JW, Holyoak GR, Bartels KE, Bunting CF, Slobodov G, and Krasinski JS (2008), " Trans-rectal ultrasound-coupled near-infrared optical tomography of the prostate, part II: experimental demonstration." *Opt Express.* 16(22):17505-20.
- Jiang Z, Ritchey JW, Holyoak GR, Bartels KE, Xu G, Bunting CF, Slobodov G, Krasinski JS, and Piao D (2009a), "In vivo trans-rectal ultrasound coupled trans-rectal near-infrared optical tomography of canine prostate bearing transmissible venereal tumor," *Proc. SPIE*, #7174-64.

- Jiang Z, Holyoak GR, Bartels KE, Ritchey JW, Xu G, Bunting CF, Slobodov G, and Piao D (2009b), "In vivo trans-rectal ultrasound-coupled near-infrared optical tomography of a transmissible venereal tumor model in canine pelvic canal ", J. Biomed. Opt. Letters, submitted.
- Li C, Liengsawangwong R, Choi H, and Cheung R (2007), "Using a priori structural information from magnetic resonance imaging to investigate the feasibility of prostate diffuse optical tomography and spectroscopy: a simulation study," Med. Phys. 34, 266-274.
- Mozos E, Mendez A, Gomez-Villamandos JC, De Las Mulas MJ, and Perez J (1996), "Immunohistochemical characterization of canine transmissible venereal tumor," Vet Pathol., 33, 257-263.
- Musgrove C, Bunting CF, Dehghani H, Pogue BW, and Piao D (2007), "Computational aspects of endoscopic near-infrared optical tomography: initial investigations," Proc. SPIE 6343, 643409
- Piao D, Jiang Z, Xu, G, Musgrove CH, and Bunting CF (2008a), "Approach on trans-rectal optical tomography probing for the imaging of prostate with trans-rectal ultrasound correlation", Proc. SPIE, 6850, 68500E.
- Piao D, Holyoak GR, Bartels KE, Ritchey JW, Jiang Z, Xu G, and Bunting CF (2008b), "In vivo trans-rectal optical tomography of normal canine prostate---demonstration of optical contrast of intact prostate over its peripheral tissue," Saratov Fall Meetings 2008, Saratov, Russia, Sep. 23-26, 2008.
- Rivera B, Ahrar K, Kangasniemi MM, Hazle JD, and Price RE (2005), "Canine transmissible venereal tumor: a large-animal transplantable tumor model," Comp Med., 55(4), 335-43.
- Shinohara K, Wheeler TM, and Scardino PT (1989), "The appearance of prostate cancer on transrectal ultrasonography: correlation of imaging and pathological examinations," J Urol;142:76–82.
- Svensson T, Andersson-Engels S, Einarsdóttir M, and Svanberg K (2007), "In vivo optical characterization of human prostate tissue using near-infrared time-resolved spectroscopy," J Biomed Opt. 12(1):014022.,
- Wang X, Pogue BW, Jiang S, Dehghani H, Song X, Srinivasan S, Brooksby BA, Paulsen KD, Kogel C, Poplack SP, and Wells WA (2006), "Image reconstruction of effective Mie scattering parameters of breast tissue in vivo with near-infrared tomography," J Biomed Opt. 11, 041106.
- Wise AM, Stamey TA, McNeal JE, and Clayton JL (2002), "Morphologic and clinical significance of multifocal prostate cancers in radical prostatectomy specimens," Urology 60, 264-9).
- Weidner N, Carroll PR, Flax J, Blumenfeld W, and Folkman J (1993), "Tumor angiogenesis correlates with metastasis in invasive prostate carcinoma," Am J Pathol. Aug;143(2):401-9.

Xu G, Piao D, Musgrove CH, Bunting CF, and Dehghani H (2008), "Trans-rectal ultrasound-coupled near-infrared optical tomography of the prostate, part I: simulation," Opt Express.; 16(22):17484-504.

Xu H (2005), "MRI-coupled broadband near-infrared tomography for small animal brain studies," Ph.D. Dissertation, Dartmouth College, Hanover, NH, 36–36.

## **APPENDICES**

1. Curriculum vitae
2. Reprints of manuscripts.

BIOGRAPHICAL SKETCH				
NAME  <b>Piao, Daqing (Daching)</b>		POSITION TITLE  <b>Assistant Professor of Bioengineering</b>		
eRA COMMONS USER NAME PIAODQ				
EDUCATION/TRAINING <i>(Begin with baccalaureate or other initial professional education, such as nursing, and include postdoctoral training.)</i>				
INSTITUTION AND LOCATION		DEGREE <i>(if applicable)</i>	YEAR(s)	FIELD OF STUDY
Tsinghua University, Beijing, China		B.Sc.	1984-1990	Physics
University of Connecticut, Storrs, CT		M.Sc.	1999-2001	Biomedical Engineering
University of Connecticut, Storrs, CT		Ph.D.	2001-2003	Biomedical Engineering

## A. POSITONS AND HONORS.

### Positions and Employment

2005--	<b>Assistant Professor of Bioengineering</b> School of Electrical & Computer Engineering, Oklahoma State University, Stillwater, OK
2004-2005	<b>Research Associate</b> Thayer School of Engineering, Dartmouth College, Hanover, NH
2003-2004	<b>Post-Doctoral Fellow</b> Department of Electrical & Computer Engineering, University of Connecticut, Storrs, CT
1994-1999	<b>R&amp;D Engineer, Project Manager</b> Shanghai Kanglian Medical Engineering Co. Ltd., Shanghai, China
1990-1994	<b>MRI Engineer</b> Guangdong Weida Medical Apparatus (Group) Co., Guangdong, China

### Professional Memberships

Member	The Institute of Electrical and Electronics Engineers (IEEE)
Member	Engineering in Medicine and Biology Society (EMBS)
Member	The International Society for Optical Engineering (SPIE)
Member	Optical Society of America (OSA)

### Professional Activities

#### **Journal Paper Reviewer**

2004-	Optics Letters	(Optical Society of America)
2004-	Applied Optics	(Optical Society of America)
2005-	Optical Engineering	(SPIE)
2005-	Journal of Biomedical Optics	(SPIE)
2005-	Lasers in Surgery & Medicine	(American Society for Laser Medicine and Surgery)
2006-	Applied Physics Letters	(American Institute of Physics)
2006-	Expert Review of Medical Devices	(Future Drugs)
2007-	Journal of Selected Topics in Quantum Electronics	(IEEE)
2007-	Optics Express	(Optical Society of America)

#### **Grant Proposal Reviewer**

2005-	<b>Reviewer</b> U.S. Civilian Research and Development Foundation Cooperative	Research Program
2006-	<b>Panelist</b> National Science Foundation, CAREER Panel	

#### **Conference Organization**

2008-	<b>Session Chair</b> SPIE International Symposium on Biomedical Optics (BIOS'08), Conference 6850, Multimodal Biomedical Imaging III, Jan. 19-24, 2008, San Jose, CA.
-------	--

### Awards and Honors

1984	<b>Youngest Freshman of the year</b> (at the age of 14), Tsinghua University, Beijing, China
------	--

- 1986 **Electronic Shop Internship Award**, General Electronic Shop, Tsinghua University, Beijing, China (Awarded to 4 out of 100)
- 1988 **Machine Shop Internship Award**, General Machine Shop, Tsinghua University, Beijing, China (Awarded to 2 out of 100)
- 1989 **Guanghua Prize**, Guanghua Foundation and Tsinghua University, Beijing, China (Awarded to 1 out of 100)
- 1990 **magna cum laude**, Tsinghua University, Beijing, China
- 1993 **Outstanding Engineer**, Guangdong Weida Medical Apparatus (Group) Corp., Guangdong, China
- 2002 **Pre-Doctoral Traineeship Award**, Department of Defense Breast Cancer Research Program
- 2003 **Best Ph.D. Thesis Award**, School of Engineering, University of Connecticut, Storrs, CT
- 2006 **New Investigator Award**, Department of Defense Prostate Cancer Research Program
- 2009 **Big XII Faculty Fellow**, Faculty Fellow Program, Big XII Universities

#### **Patents and Provisional Patent Applications**

1. **Daqing Piao**, Zhen Jiang, Guan Xu, Charles F. Bunting, "Method and Apparatus for combined/concurrent trans-channel near-infrared optical tomography and ultrasound for imaging internal organs", Provisional patent application, #61/144,556.
2. Brian W. Pogue, **Daqing Piao**, "System and method for spectral-encoded high-rate hemodynamic tomography", U.S. patent appl, #20060247531, US Class 600 (2006).
3. Brian W. Pogue, **Daqing Piao**, Keith D. Paulsen, Shudong Jiang, Hamid Dehghani, Heng Xu, Roger Springett, Subha Srinivasan, "Systems and methods for tomographic image reconstruction", World Intellectual Property Organization, patent appl. #PCT/US2006/016210, Class A61B 5/00.

#### **Invited Seminar Talks**

<b>Dartmouth College,</b>	(2004, 2006)	<b>Dartmouth Hitchcock Medical Center,</b>	(2005)
<b>UT Southwestern Medical Center,</b>	(2005)	<b>University of Texas at Arlington,</b>	(2005)
<b>University of Minnesota,</b>	(2005)	<b>Oklahoma State University,</b>	(2005, 2009)
<b>Marquette University,</b>	(2005)	<b>University of Oklahoma,</b>	(2005)
<b>Nomadics Inc.,</b>	(2005, 2007)	<b>University of Connecticut,</b>	(2006)
<b>University of Missouri--Columbia,</b>	(2007, 2009)	<b>Washington University in St. Louis,</b>	(2007)
<b>Siemens Corporate Research,</b>	(2007)	<b>The Catholic University of America,</b>	(2007)

## **B. PUBLICATIONS.**

#### **Book Chapters**

- [01] Piao D, "Diffuse Optical Techniques: Instrumentation", Chapter 4 of "*Translational Multimodal Optical Imaging*" Editor: Fred S. Azar and Xavier Intes, Publisher: Artech House, 2008.

#### **Journal Papers**

**2009----**

- [xx] Jiang Z, Holyoak GR, Bartels KE, Ritchey JW, Xu G, Bunting CF, Slobodov G, **Piao D**, "In vivo trans-rectal ultrasound-coupled near-infrared optical tomography of a transmissible venereal tumor model in canine pelvic canal", *Journal of Biomedical Optics Letters*, submitted.

**2008----**

- [27] Jiang Z, **Piao D**, Xu G, Ritchey JW, Holyoak GR, Bartels KE, Bunting CF, Slobodov G, Krasinski JS, "Trans-rectal ultrasound-coupled near-infrared optical tomography of the prostate Part II: Experimental demonstration," *Optics Express*, 16(22): 17505–17520 (2008). [PubMed index: 18958031].
- [26] Xu G, **Piao D**, Musgrove CH, Bunting CF, Dehghani H, "Trans-rectal ultrasound-coupled near-infrared optical tomography of the prostate Part I: Simulation," *Optics Express*, 16(22): 17484–17504 (2008). [PubMed index: 18958030].
- [25] Jiang Z, Zhu Q, and **Piao D**, "Minimization of geometric-beam-broadening in a grating-based time-domain delay line for optical coherence tomography application: reply to comment," *Journal of Optical Society of America A*, 25(9): 2298 (2008). [PubMed index: 18758557].

**2007----**

- [24] Jiang Z, Zhu Q, and **Piao D**, "Minimization of geometric-beam-broadening in a grating-based time-domain delay line for optical coherence tomography application," *Journal of Optical Society of America A*, 24(12): 3808-3818 (2007). [PubMed index: 18059934].

- [23] **Piao D**, Pogue BW, "Rapid near-infrared tomography for hemodynamic imaging using a low coherence wideband light source", *Journal of Biomedical Optics*, 12(1): 014016 (2007). [PubMed index: 17343491]
- 2006----**
- [22] **Piao D**, Zhang G, Vemulapalli SN, Dehghani H, Pogue BW, "Near-infrared optical tomography in endoscopy-geometry", *Optics & Photonics News*, 17(12): 31 (2006). "Optics in 2006" special issue.
- [21] **Piao D**, Xie H, Zhang W, Kransinski JS, Zhang G, Dehghani H, and Pogue BW, "Endoscopic, rapid near-infrared optical tomography", *Optics Letters*, 31(19): 2876-2878 (2006). [PubMed index: 16868408].
- 2005----**
- [20] **Piao D**, Dehghani H, Jiang S, Srinivasan S, and Pogue BW, "Instrumentation for video-rate near-infrared diffuse optical tomography", *Review of Scientific Instruments*, 76(12): 124301 (2005).
- [19] **Piao D**, Jiang S, Srinivasan S, Dehghani H, and Pogue BW, "Video-rate near-infrared optical tomography using spectrally-encoded parallel light delivery", *Optics Letters*, 30(19): 2593-2595 (2005). [PubMed index: 16208910].
- [18] **Piao D**, Sadeghi M, Zhang J, Chen Y, Sinusas A., and Zhu Q, "A hybrid positron detection and optical coherence tomography system: Design, calibration and experimental validation with rabbit atherosclerotic models", *Journal of Biomedical Optics*, 10(4): 044010 (2005). [PubMed index: 16178644].
- [17] Chen Y, Otis LL, **Piao D**, and Zhu Q, "Characterization of dentin, enamel and carious lesions by a polarization-sensitive optical coherence tomography system", *Applied Optics*, 44(11): 2041-2048 (2005). [PubMed index: 15835353].
- [16] **Piao D**, and Zhu Q, "Direct bi-directional angle-insensitive imaging of the flow signal intensity in Doppler optical coherence tomography", *Applied Optics*, 44(3): 348-357 (2005). [PubMed index: 15717824].
- 2004----**
- [15] Otis LL, **Piao D**, Gibson C, and Zhu Q, "Quantifying labial blood flow using optical Doppler tomography", *Oral Surgery, Oral Medicine, Oral Pathology, Oral Radiology, and Endodontics*, 98(2): 189-194 (2004). [PubMed index: 15316546].
- [14] Chen NG, Huang M, Xia H, **Piao D**, Zhu Q, and Cronin E, "Portable near-infrared diffusive light imager for breast cancer detection", *Journal of Biomedical Optics*, 9(3): 504-510 (2004). [PubMed index: 15189088].
- [13] Yan S, **Piao D**, Chen Y, and Zhu Q, "Digital signal processor-based real-time optical Doppler tomography system", *Journal of Biomedical Optics*, 9(3): 454-463 (2004). [PubMed index: 15189082].
- [12] **Piao D**, and Zhu Q, "Power-efficient grating-based scanning optical delay line: time-domain configuration", *Electronics Letters*, 40(2): 97-98 (2004).
- 2003----**
- [11] Zhu Q, **Piao D**, Sadeghi M, and Sinusas AJ, "Simultaneous optical coherence tomography imaging and beta particle detection", *Optics Letters*, 28(18): 1704-1706 (2003). [PubMed index: 13677543].
- [10] **Piao D**, and Zhu Q, "Quantifying Doppler angle and mapping flow velocity by a combination of Doppler-shift and Doppler-bandwidth measurements in optical Doppler tomography", *Applied Optics*, 42(25): 5158-5166 (2003). [PubMed index: 12962386].
- [09] **Piao D**, Otis LL, and Zhu Q, "Doppler angle and flow velocity mapping by combined Doppler shift and Doppler bandwidth measurements in optical Doppler tomography", *Optics Letters*, 28(13): 1120-1122 (2003). [PubMed index: 12879927].
- [08] **Piao D**, Otis LL, Dutta NK, and Zhu Q, "Quantitative assessment of flow velocity estimation algorithms for optical Doppler tomography imaging", *Applied Optics*, 41(29): 6118-6127 (2003). [PubMed index: 12389980].
- 2001----**
- [07] Zhu Q, Chen NG, Guo P, Yan S and **Piao D**, "Near infrared diffusive light imaging with ultrasound localization", *Optics and Photonics News*, 12(12): 31 (2001). "Optics in 2001" special issue.
- [06] Chen NG, Guo P, Yan S, **Piao D**, and Zhu Q, "Simultaneous near infrared diffusive light and ultrasound imaging", *Applied Optics*, 40(34): 6367-6380 (2001). [PubMed index: 18364946].
- [05] **Piao D**, Zhu Q, Dutta NK, Yan S, and Otis LL, "Cancellation of coherent artifacts in optical coherence tomography imaging", *Applied Optics*, 40(31): 5124-5131 (2001). [PubMed index: 18364794].
- [04] Zhu Q, Chen NG, **Piao D**, Guo P, and Ding X, "Design of near infrared imaging probe with the assistance of ultrasound localization", *Applied Optics*, 40(19): 3288-3303 (2001). [PubMed index: 11958271].
- 2000----**
- [03] **Piao D**, and Luo C, "The sparkle noise abatement in RF excitation signal of LMW-400 MRI system", *Chinese Journal of Medical Instrumentation*, 24(6): 326-329 (2000).
- 1999----**
- [02] Wang Q, Rong L, Lu W, Zhou B, Chen Y, Sun X, and **Piao D**, "The effects of 33.3GHz millimeter wave on H<sub>22</sub> liver cancer cell lines and the associated mice model" *Chinese Journal of Gastroenterology*, 4(2): 74-77 (1999).
- [01] **Piao D**, and Zhou B, "A review on the suppression of MRI acoustic scanning noise" *International Medical Devices*, 5(2): 48-52 (1999).

## Peer-reviewed Proceeding Papers and Abstracts (a total of 54)

### Invited Conference Presentations

**Saratov Fall Meeting'05**, Saratov, Russia, Sep. 27-30, 2005. Internet invited

**Saratov Fall Meeting'06**, Saratov, Russia, Sep. 26-29, 2006, Internet invited.

**Saratov Fall Meeting'08**, Saratov, Russia, Sep. 23-26, 2008, Internet invited.

**SPIE Internal Symposium on Biomedical Optics BIOS'07**, paper 6431-02, San Jose, CA, Jan. 20-25, 2007.

**SPIE Internal Symposium on Biomedical Optics BIOS'08**, paper 6850-13, San Jose, CA, Jan. 19-24, 2008.

## C. REARCH SUPPORT

### Ongoing Research Grants

#### 5. Big XII Faculty Fellowship Program ----- Faculty Fellow Award

**Piao, D (PI),** 02/2009----08/2009, **\$2,500**  
**Title:** Faculty Fellowship in University of Missouri, Columbia  
**Objective:** This is a faculty fellowship award for visiting Big XII universities to enhance research collaborations.

#### 4. Oklahoma EPSCoR ---- Research Opportunity Award

**Piao, D (Supporting PI),** 06/2009----08/2009, OSU- **\$3,500**  
**Jiang, Y (PI) University of Central Oklahoma** (Total \$10,000)  
**Title:** Advanced Reconstruction Method for Optical and Ultrasonographic Radiology  
**Objective:** This is a summer research opportunity award grant for faculties in Oklahoma regional universities to conduct research in Oklahoma research-intensive universities.

#### 3. Oklahoma State University-----Technology Business Assessment Group (TBAG) ---- Seed Fund

**Piao, D (PI),** 12/01/2008----11/30/2009, **\$25,000**  
**Title:** Clinical Trans-rectal Optical Imaging Applicator for Prostate Biopsy Guidance  
**Objective:** To develop a near-infrared optical imaging applicator for trans-rectal near-infrared tomography of human prostate.

#### 2. U.S. Army Medical Research and Material Command (USAMRMC) ---- New Investigator Award

**Piao, D (PI),** 03/01/2007----02/28/2010, **\$331,238**  
**Prostate Cancer Research Program**  
**Title:** Trans-rectal Near-infrared Optical Tomography for Prostate Imaging  
**Objective:** To develop and validate trans-rectal near-infrared optical tomography technique for in vivo prostate cancer imaging in animals.

#### 1. Oklahoma Center for the Advancement of Science and Technology (OCAST)

**Piao, D (PI),** 09/01/2006----08/31/2009, **\$135,000**  
**Regular Health Research Program**  
**Title:** Video-rate Endoscopic NIR tomography of Hemodynamics  
**Objective:** To develop an endoscopic imaging technology that may benefit *in vivo* minimally-invasive detection of hemodynamic changes in internal organs.

### Completed Research Grants

#### 1. U.S. Army Medical Research and Material Command (USAMRMC) ---- Pre-doctoral Training Award

**Piao, D (PI),** 06/15/2002 – 06/14/2005, **\$65,994**  
**Breast Cancer Research Program**  
**Title:** Monitoring cancer oxygenation changes induced by ultrasound  
**Objective:** To evaluate a new hypothesis that oxygen delivery to the localized tumor region could be enhanced by ultrasound at the diagnostic radiation level.



# Trans-rectal ultrasound-coupled near-infrared optical tomography of the prostate Part I: Simulation

Guan Xu,<sup>1</sup> Daqing Piao,<sup>1\*</sup> Cameron H. Musgrove,<sup>2</sup> Charles F. Bunting,<sup>1</sup>  
Hamid Dehghani<sup>3</sup>

<sup>1</sup>*School of Electrical and Computer Engineering, Oklahoma State University, Stillwater, OK, 74078-5032, USA*

<sup>2</sup>*Sandia National Laboratories, Albuquerque, NM, 87155-1330, USA*

<sup>3</sup>*School of Physics, University of Exeter, Exeter, UK, EX4 4QL*

\*Corresponding Author: [daqing.piao@okstate.edu](mailto:daqing.piao@okstate.edu)

**Abstract:** We investigate the feasibility of trans-rectal optical tomography of the prostate using an endo-rectal near-infrared (NIR) applicator that is to be integrated with a trans-rectal ultrasound (TRUS) probe. Integration with TRUS ensures accurate endo-rectal positioning of the NIR applicator and the utility of using TRUS spatial *prior* information to guide NIR image reconstruction. The prostate NIR image reconstruction is challenging even with the use of spatial *prior* owing to the anatomic complexity of the imaging domain. A hierarchical reconstruction algorithm is developed that implements cascaded initial-guesses for nested domains. This hierarchical image reconstruction method is then applied to evaluating a number of NIR applicator designs for integration with a sagittal TRUS transducer. A NIR applicator configuration feasible for instrumentation development is proposed that contains one linear array of optodes on each lateral side of the sagittal TRUS transducer. The performance of this NIR applicator is characterized for the recovery of single tumor mimicking lesion as well as dual targets in the prostate. The results suggest a strong feasibility of trans-rectal prostate imaging by use of the endo-rectal NIR/US probe.

©2008 Optical Society of America

**OCIS codes:** (170.3880) Medical and biological imaging; (170.6960) Tomography; (170.7230) Urology.

---

## References and links

1. A. Jemal, R. Siegel, E. Ward, T. Murray, J. Xu, and M. J. Thun, "Cancer statistics, 2007," *CA Cancer J. Clin.* **57**, 43-66 (2007).
2. T. J. Polascik, J. E. Oesterling, and A. W. Partin, "Prostate specific antigen: a decade of discovery--what we have learned and where we are going," *J. Urol.* **162**, 293-306 (1999).
3. G. D. Grossfeld and P. R. Carroll, "Prostate cancer early detection: a clinical perspective," *Epidemiol. Rev.* **23**, 173-80 (2001).
4. T. A. Stamey, M. Caldwell, J. E. McNeal, R. Nolley, M. Hemenez, and J. Downs, "The prostate specific antigen era in the United States is over for prostate cancer: what happened in the last 20 years?," *J. Urol.* **172**, 1297-1301 (2004).
5. C. R. Pound, A. W. Partin, M. A. Eisenberger, D. W. Chan, J. D. Pearson, and P. C. Walsh, "Natural history of progression after PSA elevation following radical prostatectomy," *JAMA*. **281**, 1591-1597 (1999).
6. A. C. Loch, A. Bannowsky, L. Baeurle, B. Grabski, B. König, G. Flier, O. Schmitz-Krause, U. Paul, and T. Loch, "Technical and anatomical essentials for transrectal ultrasound of the prostate," *World J. Urol.* **25**, 361-366 (2007).
7. A. Bill-Axelson, L. Holmberg, M. Ruutu, et al. "Radical prostatectomy versus watchful waiting in early prostate cancer," *N. Engl. J. Med.* **352**, 1977-1984 (2005).
8. B. Spajic, H. Eupic, D. Tomas, G. Stimac, B. Kruslin, and O. Kraus, "The incidence of hyperechoic prostate cancer in transrectal ultrasound-guided biopsy specimens," *Urology* **70**, 734-737 (2007).

9. K. Shinohara, T. M. Wheeler, and P. T. Scardino, "The appearance of prostate cancer on transrectal ultrasonography: correlation of imaging and pathological examinations," *J. Urol.* **142**, 76-82 (1989).
10. C. R. Porter, "Does the number of prostate biopsies performed affect the nature of the cancer identified?" *Nat. Clin. Pract. Urol.* **4**, 132-133 (2007).
11. V. Scattoni, A. Zlotta, R. Montironi, C. Schulman, P. Rigatti, and F. Montorsi, "Extended and saturation prostatic biopsy in the diagnosis and characterisation of prostate cancer: a critical analysis of the literature," *Eur. Urol.* **52**, 1309-1322 (2007).
12. B. Tromberg, J. Coquoz, O. Fishkin, J. B. Pham, T. Anderson, E. R. Butler, J. Cahn, M. Gross, J. D. Venugopalan, and D. Pham, "Non-invasive measurements of breast tissue optical properties using frequency-domain photon migration," *Phil. Trans. R. Soc. Lond. B* **352**, 661-668 (1997).
13. B. W. Pogue, S. P. Poplack, T.O. McBride, W. A. Wells, K. S. Osterman, U. L. Osterberg, and K. D. Paulsen, "Quantitative hemoglobin tomography with diffuse near-infrared spectroscopy: pilot results in the breast," *Radiology* **218**, 261-266 (2001).
14. V. Ntziachristos and B. Chance, "Probing physiology and molecular function using optical imaging: applications to breast cancer," *Breast Cancer Res.* **3**, 41-46 (2001).
15. R. Choe, A. Corlu, K. Lee, T. Durduran, S. D. Konecky, M. Grosicka-Koptyra, S. R. Arridge, B. J. Czerniecki, D. L. Fraker, A. DeMichele, B. Chance, M. A. Rosen, and A. G. Yodh, "Diffuse optical tomography of breast cancer during neoadjuvant chemotherapy: a case study with comparison to MRI," *Med. Phys.* **32**, 1128-1139 (2005).
16. M. A. Franceschini, K. T. Moesta, S. Fantini, G. Gaida, E. Gratton, H. Jess, W. W. Mantulin, M. Seeber, P. M. Schlag, and M. Kaschke, "Frequency-domain techniques enhance optical mammography: initial clinical results," *Proc. Nat. Acad. Sci. USA* **94**, 6468-6473 (1997).
17. Q. Zhu, E. B. Cronin, A. A. Currier, H. S. Vine, M. Huang, N. Chen, and C. Xu, "Benign versus malignant breast masses: optical differentiation with US-guided optical imaging reconstruction," *Radiology* **237**, 57-66 (2005).
18. S. A. Bigler, R. E. Deering, and M. K. Brawer, "Comparison of microscopic vascularity in benign and malignant prostate tissue," *Hum. Pathol.* **24**, 220-226 (1993).
19. J. H. Ali, W. B. Wang, M. Zevallos, and R. R. Alfano, "Near infrared spectroscopy and imaging to probe differences in water content in normal and cancer human prostate tissues," *Technol. Cancer Res. Treat.* **3**, 491-497 (2004).
20. M. R. Arnfield, J. D. Chapman, J. Tulip, M. C. Fenning, and M. S. McPhee, "Optical properties of experimental prostate tumors in vivo," *Photochem. Photobiol.* **57**, 306-311 (1993).
21. T. C. Zhu, A. Dimofte, J. C. Finlay, et al. "Optical properties of human prostate at 732 nm measured in mediated photodynamic therapy," *Photochem. Photobiol.* **81**, 96-105 (2005).
22. T. Svensson, S. Andersson-Engels, M. Einarsdóttir, and K. Svanberg, "In vivo optical characterization of human prostate tissue using near-infrared time-resolved spectroscopy," *J. Biomed. Opt.* **12**, 014022 (2007).
23. M. Goel, H. Radhakrishnan, H. Liu, et al. "Application of near infrared multi-spectral CCD imager system to determine the hemodynamic changes in prostate tumor," in *OSA Biomedical Topical Meetings* (Optical Society of America, 2006), paper SH10.
24. H. Liu, Y. Song, K. L. Worden, X. Jiang, A. Constantinescu, and R. P. Mason, "Noninvasive investigation of blood oxygenation dynamics of tumors by near-infrared spectroscopy," *Appl. Opt.* **39**, 5231-43 (2000).
25. X. Zhou and T. C. Zhu, "Image reconstruction of continuous wave diffuse optical tomography (DOT) of human prostate," in *Proceedings of the COMSOL Users Conference* (2006).
26. S. L. Jacques and M. Motamedi, "Tomographic needles and catheters for optical imaging of prostatic cancer," *Proc. SPIE* **2395**, 111-118 (1995).
27. C. Li, R. Liengsawangwong, H. Choi, and R. Cheung, "Using *a priori* structural information from magnetic resonance imaging to investigate the feasibility of prostate diffuse optical tomography and spectroscopy: a simulation study," *Med. Phys.* **34**, 266-274 (2007).
28. C. Musgrove, C. F. Bunting, H. Dehghani, B. W. Pogue, and D. Piao, "Computational aspects of endoscopic near-infrared optical tomography: initial investigations," *Proc. SPIE* **6343**, 643409 (2007).
29. D. Piao, H. Xie, W. Zhang, G. Zhang, C. H. Musgrove, C. F. Bunting, H. Dehghani, B. W. Pogue, and S. N. Vemulapalli, "Near-infrared optical tomography: endoscopic imaging approach," *Proc. SPIE* **6431**, 643103 (2007).
30. H. Dehghani, C. M. Carpenter, P. K. Yalavarthy, B. W. Pogue, and J. P. Culver, "Structural *a priori* information in near-infrared optical tomography," *Proc. SPIE* **6431**, 64310B1 (2007).
31. Q. Zhu, T. Durduran, V. Ntziachristos, M. Holboke, and A. G. Yodh, "Imager that combines near-infrared diffusive light and ultrasound," *Opt. Lett.* **24**, 1050-1052 (1999).
32. M. J. Holboke, B. J. Tromberg, X. Li, N. Shah, J. Fishkin, D. Kidney, J. Butler, B. Chance, and A. G. Yodh, "Three-dimensional diffuse optical mammography with ultrasound localization in a human subject," *J. Biomed. Opt.* **5**:237-47 (2000).
33. B. W. Pogue, S. Geimer, T. O. McBride, S. Jiang, U. L. Osterberg, and K. D. Paulsen, "Three-dimensional simulation of near-infrared diffusion in tissue: boundary condition and geometry analysis for finite-element image reconstruction," *Appl. Opt.* **40**, 588-600 (2001).

34. M. Schweiger, S. R. Arridge, and D. T. Delpy, "Application of the finite-element method for the forward and inverse models in optical tomography," *J. Math. Imag. Vision* **3**, 263-283 (1993).
35. J. J. More, "Levenberg-Marquardt algorithm: implementation and theory," in *Numerical Analysis*, (Springer Berlin / Heidelberg, 1978), pp. 105-116.
36. X. Yu, G. Chen, and S. Cheng, "Dynamic learning rate optimization of the backpropagation algorithm," *IEEE Trans. Neural Netw.* **6**, 669-677 (1995).
37. D. Shen, Y. Zhan, and C. Davatzikos, "Segmentation of prostate boundaries from ultrasound images using statistical shape model," *IEEE Tran. Med. Imaging* **22**, 539-55 (2003).
38. M. Schweiger, S. R. Arridge, O. Dorn, A. Zacharopoulos, and V. Kolehmainen, "Reconstructing absorption and diffusion shape profiles in optical tomography using a level set technique," *Opt. Lett.* **31**, 471-473 (2006).
39. V. Kolehmainen, S. R. Arridge, W. R. B. Lionheart, M. Vauhkonen, and J. P. Kaipio, "Recovery of region boundaries of piecewise constant coefficients of an elliptic PDE from boundary data," *Inverse Probl.* **15**, 1375-1391 (1999).
40. V. Kolehmainen, M. Vauhkonen, J. P. Kaipio, and S. R. Arridge, "Recovery of piecewise constant coefficients in optical diffusion tomography," *Opt. Express* **7**, 468-480 (2000).
41. V. Kolehmainen, S. R. Arridge, M. Vauhkonen, and J. P. Kaipio, "Simultaneous reconstruction of internal tissue region boundaries and coefficients in optical diffusion tomography," *Phys. Med. Biol.* **45**, 3267-3284 (2000).
42. S. Srinivasan, B. W. Pogue, H. Dehghani, S. Jiang, X. Song, and K. D. Paulsen, "Improved quantification of small objects in near-infrared diffuse optical tomography," *J. Biomed. Opt.* **9**, 1161-1171 (2004).
43. P. K. Yalavarthy, H. Dehghani, B. W. Pogue, and K. D. Paulsen, "Critical computational aspects of near infrared circular tomographic imaging: Analysis of measurement number, mesh resolution and reconstruction basis," *Opt. Express* **14**, 6113-6127 (2006).
44. H. Shan, N. Pantong, J. Su, H. Liu, and M. V. Klibanov, "Globally convergent reconstruction algorithm for diffusion tomography of prostate," in *Biomedical Optics/Digital Holography and Three-Dimensional Imaging/Laser Applications to Chemical, Security and Environmental Analysis* on CD-ROM (The Optical Society of America, Washington, DC, 2008), paper BSuE33.
45. A. M. Wise, T. A. Stamey, J. E. McNeal, and J. L. Clayton, "Morphologic and clinical significance of multifocal prostate cancers in radical prostatectomy specimens," *Urology* **60**, 264-9 (2002).
46. G. J. Miller and J. M. Cygan, "Morphology of prostate cancer: the effects of multifocality on histological grade, tumor volume and capsule penetration," *J. Urol.* **152**(5 Pt 2), 1709-13 (1994).

## 1. Introduction

Prostate cancer is the second most commonly diagnosed cancer and the second leading cause of cancer deaths in American men [1]. Prostate cancer screening is performed by measurement of serum prostate-specific antigen (PSA) [2], digital rectal examination (DRE), and in many cases a combination of both tests [3]. The introduction of PSA test contributed to substantially increased detection rate of organ-confined prostate cancer or considerable stage migration [4]. However, PSA is not a specific indicator of prostate malignancy and post-treatment tumor recurrence, except after radical prostatectomy [5]. A clearly increased serum PSA value (>20 ng/ml) may indicate the presence of a prostate carcinoma at a very high probability [6]. In the gray zone between 4 and 10 ng/ml the tissue marker PSA is frequently influenced by benign alterations, so that it is not possible, on the basis of the PSA value alone, to differentiate between benign and malignant cases [6, 7]. DRE can often distinguish between prostate cancer and non-cancerous conditions; it may also detect prostate cancers having normal PSA levels. However, palpation during a DRE is subjective, insensitive, and more than half of all prostate cancers detected are not palpable [3]. When the suspicion of prostate cancer is raised by abnormal PSA and/or DRE, the diagnosis is made by biopsy. The technique of trans-rectal ultrasound (TRUS) based trans-rectal prostate biopsy, carried out with a semi-automatic coil spring device and an 18-gauge needle, is to date considered as the gold standard [6].

Prostate neoplastic lesions may be identified on TRUS as being hypoechoic [8]. However at most 60% neoplastic lesions appear hypoechoic on TRUS while most of the remaining neoplastic lesions appear isoechoic [9]. The hypoechoic, cancer-suspicious areas may be histologically either benign or malignant [9]. The lack of TRUS specificity thereby prompts the practice of "systematic biopsy" of the prostate. The current trend is to use 10- to 12-core

biopsy with a preference in the peripheral zone, where most neoplastic lesions are found, as the initial biopsy strategy. It should be noted that the majority of biopsies are found to be negative, and in men with persistent suspicion of prostate cancer after several negative biopsies, more extensive protocols (>12 cores) up to saturation biopsy (24 cores) represent a necessary diagnostic procedure [10]. However, despite years of research, the exact number of biopsies to be taken is still largely unknown [11].

The need of having many biopsy-cores for systematic, yet random, tissue sampling of the prostate may be alleviated if the acoustic contrast that TRUS relies on is augmented with functional or “surrogate” markers of the prostate tumor such that the biopsy is directed to the malignant lesions. A functional imaging modality augmenting TRUS is certainly more desirable if it is non-ionizing and minimally-invasive as is TRUS. Optical tomography based on near-infrared (NIR) light could emerge as such a modality.

Near-infrared measurements of attenuation through tissue have demonstrated significant contrast gradients between blood and parenchymal tissue that is otherwise difficult to obtain [12-17]. The alteration of vascularity or the hemoglobin content in the tumor provides high intrinsic optical contrast between the tumor and benign tissues which has been well-demonstrated in breast cancer imaging [12-17]. When multi-spectral detection is engaged, NIR imaging is also capable of directly quantifying the chromophore concentrations important for characterization of the malignancy [12-17]. In prostate, studies have shown vascular density gradient in malignant versus benign tissue specimens [18], and different water concentrations in cancerous and benign tissues *in vitro* [19]. Invasive NIR measurements of prostate have been conducted for experimental prostate tumors [20] and human prostate [21, 22]. Surface measurements of implanted prostate tumor have also been reported [23, 24]. All these studies demonstrate the potential of using NIR to detect and characterize prostate cancer. NIR diffuse optical measurement, performed interstitially, is also becoming an important tool for monitoring photodynamic therapy in prostate [21, 22, 25]. Prostate NIR imaging via trans-urethral probing had been analyzed and tested [26]. Recently, trans-rectal prostate NIR imaging has been investigated in simulation in the context of assisting MRI for treatment decision [27].

To our knowledge, experimental work on trans-rectal NIR tomography has not been performed except for our recent attempts [28, 29] which may be largely due to the challenge of fabricating a suitable trans-rectal applicator. Optical tomography typically needs 10s of channels of NIR optodes in order to achieve reasonable spatial resolution as a large tissue volume is being interrogated. The NIR illumination can be delivered by small diameter fibers, but the detection of weak scattered light is in favor of fibers of larger diameters and/or suitably larger numerical apertures. Unlike in breast NIR tomography where there is minimum spatial restriction for the optode configuration, trans-rectal applicator for NIR tomography has to deploy many optodes in a very compact space. This restriction could become more pronounced when trans-rectal NIR applicator is also to be combined with TRUS transducer. Since the depth of tissue interrogation by diffuse NIR light is roughly one-half of the source-detector separation for typical scattering-dominant biological tissue, reaching targets centimeters deep in prostate implies a NIR array of several centimeters in size. Such an NIR array is feasible for trans-rectal application if the optodes are arranged longitudinally, which should provide a sagittal-view in trans-rectal NIR imaging. The images obtained by trans-rectal NIR tomography alone would, however, be difficult to correlate with the anatomy. Unlike in breast imaging where the NIR applicator could be accurately positioned, accurate positioning of a trans-rectal NIR applicator with respect to the prostate is difficult which is due to the “blind” location of the prostate, slow NIR image reconstruction, and lack of anatomic details in NIR tomography images. It is thereby imperative to use a real-time morphological imaging modality concurrently with trans-rectal NIR tomography to provide a positioning guidance for NIR applicator in order to correlate the NIR tomography findings with the prostate anatomy. The structural information of the prostate can further be utilized as

the spatial *prior* [30] to improve the accuracy of NIR image reconstruction. Among the prostate imaging techniques, TRUS is perhaps the best modality for trans-rectal NIR tomography to combine owing to the operational similarity between these two modalities.

The diagnostic benefit of augmenting NIR contrast to US has been demonstrated in breast cancer detection [31, 32]. The methodology of combining NIR & US can certainly be extended from breast imaging to prostate imaging; nevertheless, the technique cannot be extended from imaging the breast to imaging the prostate without an NIR/US applicator suitable for trans-rectal manipulation. In this work, we demonstrate TRUS coupled trans-rectal optical tomography of the prostate. This work is reported in two consecutive papers. The Part-I paper, based on simulation, investigates designs of NIR tomography applicator suitable for integrating with a commercial TRUS transducer. A hierarchical NIR image reconstruction algorithm is developed for utilizing the TRUS structural *a priori* information which is then used to evaluate several NIR applicator configurations for integrating with a TRUS transducer. The Part-II paper implements the probe design suggested in Part-I, presents the instrumentation details of the TRUS coupled trans-rectal NIR tomography probe & system, and demonstrates TRUS-coupled trans-rectal NIR tomography of a canine prostate.

## 2. The geometry of trans-rectal NIR imaging and the utility of TRUS information

### 2.1 Configuration of sagittal trans-rectal NIR array for coupling with sagittal TRUS

The TRUS is typically performed in bi-plane (sagittal and transverse) for prostate imaging. The sagittal and transverse views are switched during prostate imaging, but for biopsy procedure, the firing of the spring-loaded needle is monitored in the sagittal plane wherein the needle trajectory may be accurately marked. We have acquired a bi-plane TRUS probe (Aloka UST-672-5/7.5) as is shown in Fig. 1(a), which has a proximal sagittal transducer window of 60mm×10mm and a distal transverse transducer window of 120°×10mm. The cylindrical TRUS probe has a maximum diameter of 20mm. Integrating NIR applicator to a TRUS probe implies that the dimension, particularly the radial one, of the NIR array is quite restricted. As discussed earlier, longer source-detector separation is needed to interrogate deeper targets; therefore the most feasible configuration of an NIR array may be through distributing a linear array of optode on each lateral side of the sagittal TRUS transducer, as illustrated in Fig. 1(b). Taking into account the mechanical structure necessary to support the optodes, the combined

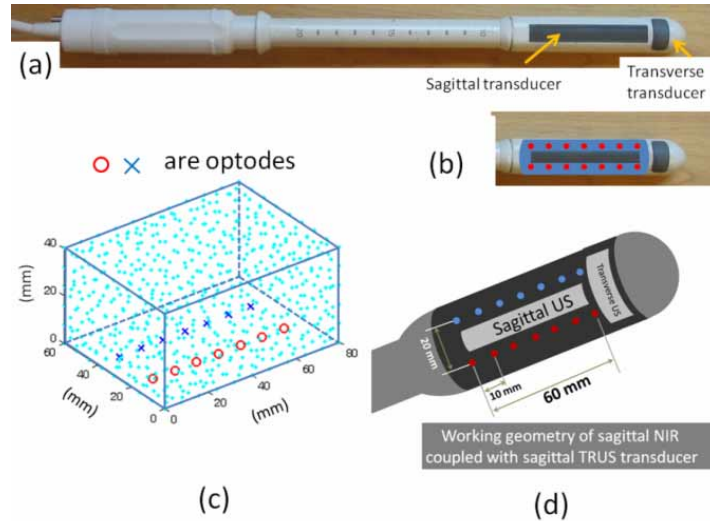


Fig. 1. (a) Photograph of a bi-plane TRUS transducer. (b) Configuration of an NIR array feasible for coupling with sagittal TRUS. (c) The NIR imaging geometry for the one depicted in (b). (d) Illustration of a trans-rectal probe that integrates NIR and US synergistically.

probe will likely have a radial size of at least a few millimeters larger than that of the original TRUS probe. NIR tomography has to use multimode fibers to detect weak diffuse light, and these multimode fibers must be delivered longitudinally before being side-fired. Bending the fiber is not a viable solution here for side-firing unless the fibers are passed inside the TRUS probe. The side-firing alternatively may however be realized by implementing micro-optical components, but the compact space inside or surrounding the probe may not accommodate a large number of such channels. A NIR array, which could couple with TRUS, may be configured by fabricating 7 fiber channels on each lateral side of the TRUS to span 60mm longitudinally as the TRUS does, and placing the optical channels 10mm apart. The NIR array must leave the 10mm-wide sagittal TRUS transducer unblocked; therefore a 20mm spacing of the NIR optodes from one lateral side to the other is perhaps needed. These considerations lead to the NIR array geometry shown in Fig. 1(c) where 14 optodes are spaced 10mm longitudinally and 20mm laterally. Fig. 1(d) illustrates an NIR/US probe if the sagittal NIR array can be fabricated synergistically with the TRUS probe.

## 2.2 Forward and inverse methods for sagittal trans-rectal optical tomography

The prostate and peripheral tissues are scattering-dominant in NIR [19-22]. We use the diffusion approximation to the radiative transport equation in frequency-domain [33]:

$$\nabla \cdot D(\vec{r}) \nabla U(\vec{r}, \omega) - (\mu_a + \frac{i\omega}{c}) U(\vec{r}, \omega) = -S(\vec{r}, \omega) \quad (1)$$

where  $U(\vec{r}, \omega)$  is the photon fluence rate at position  $\vec{r}$ ,  $S(\vec{r}, \omega)$  is the source,  $\omega$  is the source modulation frequency,  $c$  is the speed of light in the medium,  $\mu_a$  is the absorption coefficient, and  $D = [3(\mu_a + \mu'_s)]^{-1}$  is the diffusion coefficient with  $\mu'_s$  being the reduced or transport scattering coefficient. Finite-element method [34] is used to solve Equ. (1) under the Robin-type boundary condition [33]:

$$U(\vec{r}_0, \omega) + 2DA\hat{n}_0 \cdot \nabla U(\vec{r}_0, \omega) = 0 \quad (2)$$

where  $\vec{r}_0$  is the boundary,  $\hat{n}_0$  is the outward normal vector of the boundary and  $A$  is the refractive index mismatch coefficient. The refractive indices used for air and tissue are 1 and 1.33 respectively, leading to  $A=2.82$  as in [33].

The imaging volume is divided to 4 regions-of-interest (ROIs): the rectum wall, the periprostate tissue, the prostate, and the prostate tumor. The Jacobian (sensitivity) values are calculated for each ROI rather than each node which has the form of:

$$J = \begin{bmatrix} \frac{\partial \ln I_{11}}{\partial \mu_{a\_rect}} & \frac{\partial \ln I_{11}}{\partial \mu_{a\_peri}} & \frac{\partial \ln I_{11}}{\partial \mu_{a\_pros}} & \frac{\partial \ln I_{11}}{\partial \mu_{a\_lesi}} & \frac{\partial \ln I_{11}}{\partial \mu'_{s\_rect}} & \frac{\partial \ln I_{11}}{\partial \mu'_{s\_peri}} & \frac{\partial \ln I_{11}}{\partial \mu'_{s\_pros}} & \frac{\partial \ln I_{11}}{\partial \mu'_{s\_lesi}} \\ \frac{\partial \ln I_{12}}{\partial \mu_{a\_rect}} & \ddots & \ddots & \vdots & \vdots & \ddots & \ddots & \vdots \\ \vdots & \ddots & \ddots & \vdots & \vdots & \ddots & \ddots & \vdots \\ \frac{\partial \ln I_{77}}{\partial \mu_{a\_rect}} & \dots & \dots & \frac{\partial \ln I_{77}}{\partial \mu_{a\_lesi}} & \frac{\partial \ln I_{77}}{\partial \mu'_{s\_rect}} & \ddots & \ddots & \frac{\partial \ln I_{77}}{\partial \mu'_{s\_lesi}} \\ \frac{\partial \phi_{11}}{\partial \mu_{a\_rect}} & \frac{\partial \phi_{11}}{\partial \mu_{a\_peri}} & \frac{\partial \phi_{11}}{\partial \mu_{a\_pros}} & \frac{\partial \phi_{11}}{\partial \mu_{a\_lesi}} & \frac{\partial \phi_{11}}{\partial \mu'_{s\_rect}} & \dots & \dots & \frac{\partial \phi_{11}}{\partial \mu'_{s\_lesi}} \\ \frac{\partial \phi_{12}}{\partial \mu_{a\_rect}} & \ddots & \ddots & \vdots & \vdots & \ddots & \ddots & \vdots \\ \vdots & \ddots & \ddots & \vdots & \vdots & \ddots & \ddots & \vdots \\ \frac{\partial \phi_{77}}{\partial \mu_{a\_rect}} & \dots & \dots & \frac{\partial \phi_{77}}{\partial \mu_{a\_lesi}} & \frac{\partial \phi_{77}}{\partial \mu'_{s\_rect}} & \dots & \dots & \frac{\partial \phi_{77}}{\partial \mu'_{s\_lesi}} \\ \frac{\partial \mu_{a\_rect}}{\partial \mu_{a\_rect}} & \dots & \dots & \frac{\partial \mu_{a\_rect}}{\partial \mu_{a\_lesi}} & \frac{\partial \mu_{a\_rect}}{\partial \mu'_{s\_rect}} & \dots & \dots & \frac{\partial \mu_{a\_rect}}{\partial \mu'_{s\_lesi}} \end{bmatrix} \quad (3)$$

where  $I_{ij}$  ( $i, j=1,2,...,7$ ) and  $\phi_{ij}$  ( $i, j=1,2,...,7$ ) are the intensity and phase terms of  $U(\vec{r}, \omega)$ , respectively. In Equ. 3, “rect”, “peri”, “pros”, and “lesi” denote “rectum wall”, “peri-prostate tissue”, “prostate”, and “prostate lesion”, respectively.

The Levenberg-Marquart (LM) algorithm [35] governs the iterative recovery of the optical properties by updating the ROI-specific values of  $\mu_a$  and  $\mu_s$  according to

$$x_{k+1} = x_k + \alpha \cdot [J^T(x_k)J(x_k) + \lambda I]^{-1} J^T(x_k) \Delta v(x_k) \quad (4)$$

where  $x$  is the array of parameters to be optimized,  $\Delta v$  is the forward projection error and  $\lambda$  is a penalty or regularization term. A small damping factor  $\alpha$  in the range of (0, 1) is introduced in Equ. 4 to stabilize the convergence. It is shown that an empirically chosen  $\alpha$  could make the LM algorithm more reliable and computationally more efficient [36].

### 2.3 TRUS prior assisted finite-element mesh for trans-rectal NIR tomography reconstruction

The TRUS prostate images which are available in open sources [37] are used for the simulation study. The TRUS image was first imported into a pre-processing software 3ds-MAX [Autodesk Inc] (shown in Fig. 2(a)). The 3ds-MAX provides very flexible geometry-deforming functions, with which a basic 3-D geometry of the prostate can be outlined manually. The finalized 3-D mesh of the prostate is then converted to COMSOL Multiphysics [COMSOL AB] compatible format (shown in Fig. 2(b)) using MeshToSolid [Syncode Inc]. The prostate tumor is then mimicked using a spherical shape to allow for flexibility of adjusting its size. The absorption and reduced scattering coefficients of the rectum, peri-prostate tissue, prostate and the tumor are assigned with values as suggested by literature [27]. Figure 3 illustrates one example of the completed FEM-mesh for trans-rectal optical tomography derived from a TRUS image, where  $x$ ,  $y$  and  $z$  denoting the longitudinal, lateral and the depth coordinates, respectively. A typical mesh used for this work contains approximately 4000 nodes and 20000 linear tetrahedral elements.

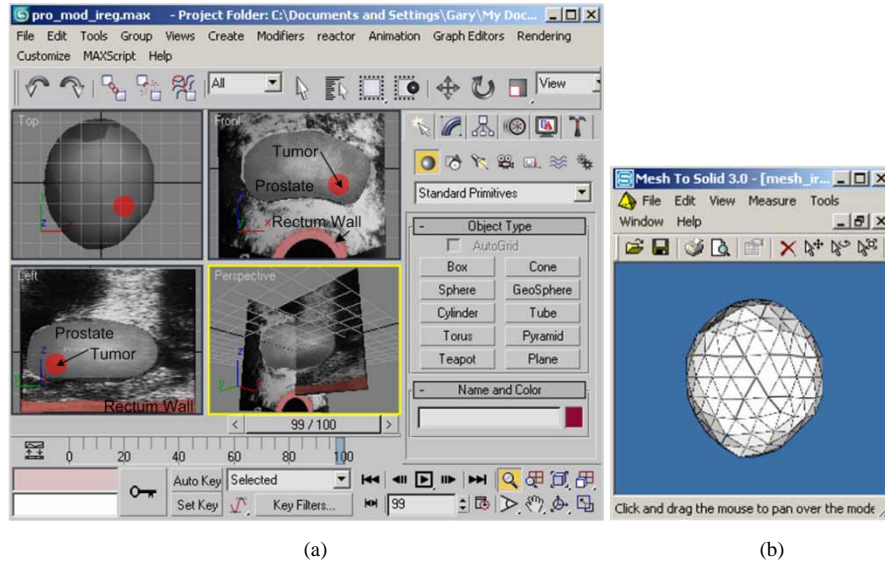


Fig. 2. (a) 3ds-MAX Interface, (b) Mesh-to-Solid Interface

The mesh in Fig. 3 corresponds to a volume of  $80 \times 80 \times 80 \text{ mm}^3$  and the ‘walnut’ shaped prostate has a dimension of  $50 \times 50 \times 30 \text{ mm}^3$ . The rectum wall is 4mm thick with a curvature radius of 80 mm. The choice of the curvature radius is due to the fact that the NIR array added to a TRUS probe may have a flat surface that would transform the rectum lumen to an



elliptical shape. A larger radius also gives more flexibility in handling the posterior prostate region within the mesh.

Although only the rectum wall is a physical boundary, treating the other 5 surfaces as physical boundaries (Robin type, Equ. 2) should have negligible effect upon the results as the lateral-medial and ventral-dorsal dimensions well exceed the potential path of photon propagation for the NIR array given in Fig. 1(c). The modulation frequency  $\omega$  of the source in Equ. 1 is set at 100MHz, and 1% Gaussian noise is added to all forward calculations to form the measurement data.

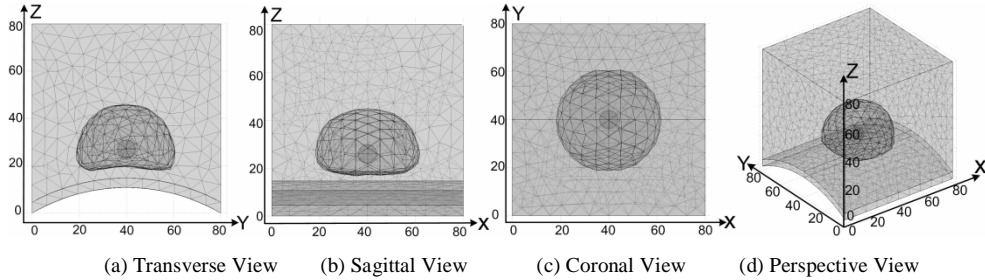


Fig. 3. FEM mesh generated based on approaches in Fig. 2. [Unit: mm].

### 3. A hierarchical spatial prior approach for trans-rectal NIR tomography reconstruction

#### 3.1 Sensitivity of the sagittal trans-rectal NIR array

The NIR array proposed in Fig. 1(c) has 7 source channels occupying one linear array and 7 detection channels occupying the other array. The sensitivity with respect to a perturbation of a specific optical property is determined by the corresponding Jacobian values in Equ. 3. Figure 4 plots the sensitivity specific to absorption, or  $\partial \ln I_{ij} / \partial \mu_a$ , for a medium with optical properties of  $\mu_a = 0.01 \text{ mm}^{-1}$  and  $\mu_s' = 1.0 \text{ mm}^{-1}$ , calculated by projecting the Jacobian values along a line in the imaging volume. Figure 4(a) is the longitudinal sensitivity in the mid-sagittal plane for a line from (0, 40, 30) to (80, 40, 30), Fig. 4(b) is the lateral sensitivity in the mid-transverse plan for a line from (40, 0, 30) to (40, 80, 30), and Fig. 4(c) is the depth sensitivity in the mid-sagittal plane for a line from (40, 40, 15.1) (here 15.1 is the  $z$  coordinate, but the actual depth from the rectum surface is 0mm owing to the curvature of the rectum) to (40, 40, 80), respectively. The dimension or the locations of the source & detector array is marked on the abscissa of all three plots. The TRUS sagittal plane is located at  $y=40\text{mm}$ , which is the mid-sagittal plane within the NIR imaging volume.

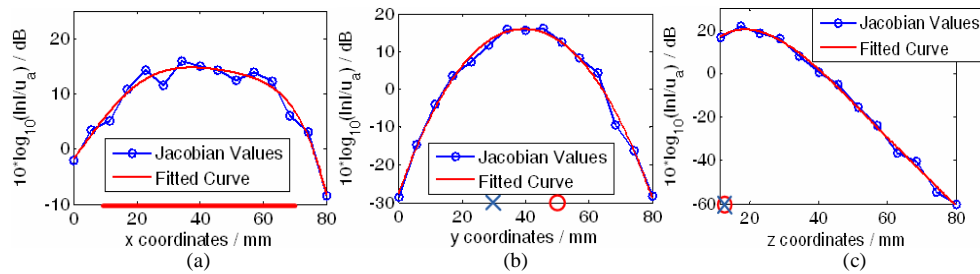


Fig. 4. Sensitivity profile. (a) Mid-sagittal plane, longitudinal sensitivity; (b) mid-transverse plane, lateral sensitivity; (c) mid-sagittal plane, depth sensitivity. The marks on abscissa or the origin show the positions of optodes.

Figure 4 indicates that the longitudinal sensitivity has  $\sim 6\text{dB}$  variation in the middle 75% range of the array, and the lateral sensitivity peaks at the mid-sagittal plane. In the middle-



sagittal plane the sensitivity degrades  $\sim 1\text{dB/mm}$  as z-coordinate increases from 20mm, which is apparently due to the side-way placement of the NIR array. The depth-degrading sensitivity will cause deeper targets to be reconstructed at a shallower position [28] if no spatial *prior* is incorporated.

### 3.2 Trans-rectal NIR image reconstruction without a priori information

The performance of recovering tumor-mimicking target by trans-rectal NIR tomography without any structural *prior* is examined. Figure 5 lists the results for the tumor target being placed at left, middle, and right within the prostate. The top row in Fig. 5 lists the target images of  $\mu_a$  and  $\mu_s'$  generated by the TRUS-defined geometry as shown in Fig. 3. The optical properties of the 10mm diameter tumor target are  $\mu_a = 0.02\text{mm}^{-1}$  and  $\mu_s' = 1.6\text{mm}^{-1}$ , with the parameters of other regions as listed in Table 1. These target images are used to generate the noise-added simulated measurement data. The image reconstruction is then conducted using a mesh of homogenous element density throughout the entire volume and updated element by element. The results are given in the bottom row of Fig. 5. As seen, the tumor target may be localized, but the recovered resolution or spatial information is poor. The accuracy of optical property recovery is also low. Further, it is found that a tumor target with negative contrast in absorption cannot be accurately recovered using similar settings. It is however expected that the detection and characterization of the tumor target will be improved when the spatial information of prostate and the tumor is available.

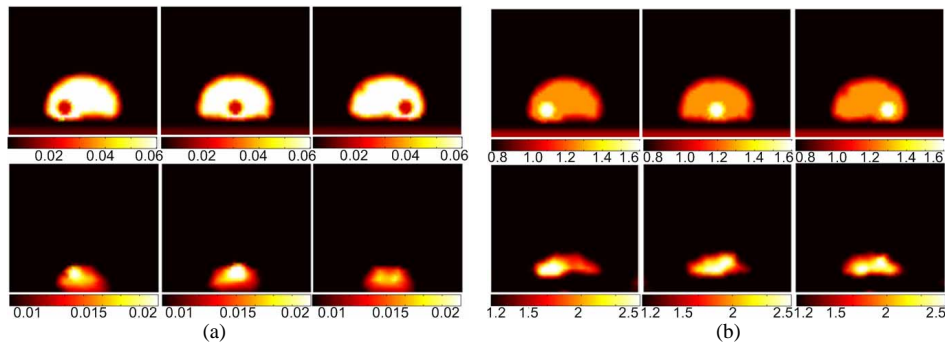


Fig. 5. NIR-only element-based reconstruction of a tumor target in various longitudinal locations. Row 1: target image for calculating the forward data; Row 2: Images reconstructed without any spatial prior. (a):  $\mu_a$  images; (b):  $\mu_s'$  images. [Unit:  $\text{mm}^{-1}$ ]

### 3.3 A hierarchical spatial prior method for TRUS guided trans-rectal NIR reconstruction

The tissue volume interrogated by trans-rectal NIR imaging constitutes a nested-domain including a thin layer of rectum wall, a large volume of peri-prostate tissue, a relatively absorbing prostate, and the lesion within the prostate. These nested imaging domains may be further complicated by the pelvic bone that could interfere with the light propagation. Schweiger, et al. [38], Kolehmainen et al. [39-41], and Srinivasan et al. [42] have previously investigated the issue of recovering the shapes and optical properties of regions with optical contrast inside a non-nested or nested domains, where the shapes of the ROIs were derived from optical information when no spatial *prior* is available from other complementary imaging modalities. These methods have shown sufficient robustness in recovering the shapes and optical properties of the ROIs, yet the problem of stability and/or slow convergence was noticed in such approaches dealing with nested-domains. In trans-rectal NIR tomography reconstruction the spatial information from TRUS may be implemented by assigning homogenous optical properties within each ROIs of the imaging domain. However the convergence and the accuracy of reconstruction will still depend upon the initial guess in

addition to the accuracy of the *prior* information. The dependence on initial guess in a gradient based solver is due to the local minimum feature [36], as indicated in Fig. 6, which could be exaggerated in prostate imaging due to the possible multiple combinations of optical properties in the nested-structures. The image reconstruction in trans-rectal optical tomography is further complicated by the discrepancy regarding the optical contrast that the prostate tumor could have, namely positive or negative [19-22, 27].

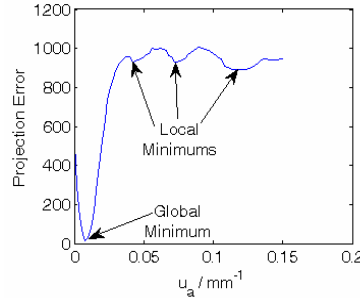


Fig. 6. Local-minimum issue in reconstruction. The forward calculation is based on Fig. 3(a) with assumption of homogeneous imaging volume. The projection error is calculated by using reduced scattering coefficient of the true value ( $0.008\text{mm}^{-1}$ ), and using an absorption coefficient value from 0 to  $0.15\text{mm}^{-1}$  at a step of  $0.002\text{mm}^{-1}$ , with respect to the forward data. Other than the global minimum, three local minimums can be observed where the iteration can stop incorrectly. This is the effect of varying only one parameter. More local minimums may occur when reconstructing more parameters.

When the TRUS is available, a conventional method of utilizing the spatial information would be the having the optical property of each ROI set as homogenous and updated simultaneously at each iteration. However, we have found that this conventional approach may not lead to reliable convergence for prostate imaging, which is attributed to the local-minimum problem. One example is given in Table 1 for the NIR array shown in Fig. 1(c). The prostate model is generated according to a previous work [27] (details of which are given later in Fig. 8), and a target of 10mm diameter is located at (40, 50, 15) which is 15 mm from the rectal surface. When the four ROIs including the rectum, the peri-prostate tissue, the prostate, and the prostate tumor are updated simultaneously from the same initial guess of  $\mu_a = 0.01\text{mm}^{-1}$  and  $\mu_s' = 1.0\text{mm}^{-1}$ , the iteration stops after 1 update due to the negative  $\mu_a$  value obtained for the rectum wall. The iteration fails to continue apparently due to the local minimum issue.

Table 1. Results of simultaneously updating the 4 ROIs from the same initial guess

Regions	$\mu_a \text{ (mm}^{-1}\text{)}$				$\mu_s' \text{ (mm}^{-1}\text{)}$			
	Surrounding Tissue	Rectum Wall	Prostate	Tumor	Surrounding Tissue	Rectum Wall	Prostate	Tumor
Set value	0.002	0.01	0.06	0.02	0.8	1	1.27	1.6
Simultaneous Update	0.1216	<b>-0.008</b>	0.026	0.0215	1.1482	2.3602	0.6173	0.7073

The local minimum problem may be mitigated by a cascaded initial-guess approach or a hierarchical spatial *prior* method. The principle of this method is to first reconstruct the global optical properties of the entire volume, then to reconstruct the optical properties of prostate and rectum wall, and last to reconstruct the tumor lesion area. The 2<sup>nd</sup> and 3<sup>rd</sup> steps use the value obtained in the previous step as the initial guess of that specific ROI. Therefore at each step, the perturbation by a relatively smaller region is less influential and convergence of the iteration is better achieved. The detailed steps are shown in Fig. 7 and described in below:

(a) The first iterations assign an entirely homogenous imaging volume. In this round the initial projection error will be large and the convergence is most likely dominated by the global minimum. A single set of  $\mu_a$  and  $\mu_s$  are determined using LM algorithm (Equ. 4) and will be used as the initial guess for the second step.

(b) The second iterations consider three regions, the rectum wall, peri-prostate tissue, and prostate, within the imaging volume. The calculation of the optical properties of these three ROIs start at the same initial guess as provided in step (a) but converges at different values.

(c) The values obtained from step (b) are used as the initial guess for the three ROIs but with a tumor added to the prostate. The tumor and the prostate take the same initial values as determined by the previous step. Each of the four ROIs (rectum wall, peri-prostate tissue, prostate, and tumor) converge to different end value.

The change of the overall projection error for the three steps is plotted in Fig. 7(d), and as evident, rapid and reliable convergence is observed. The hierarchy of the implementation of initial values for iteration is illustrated alternatively in Fig. 7(e).

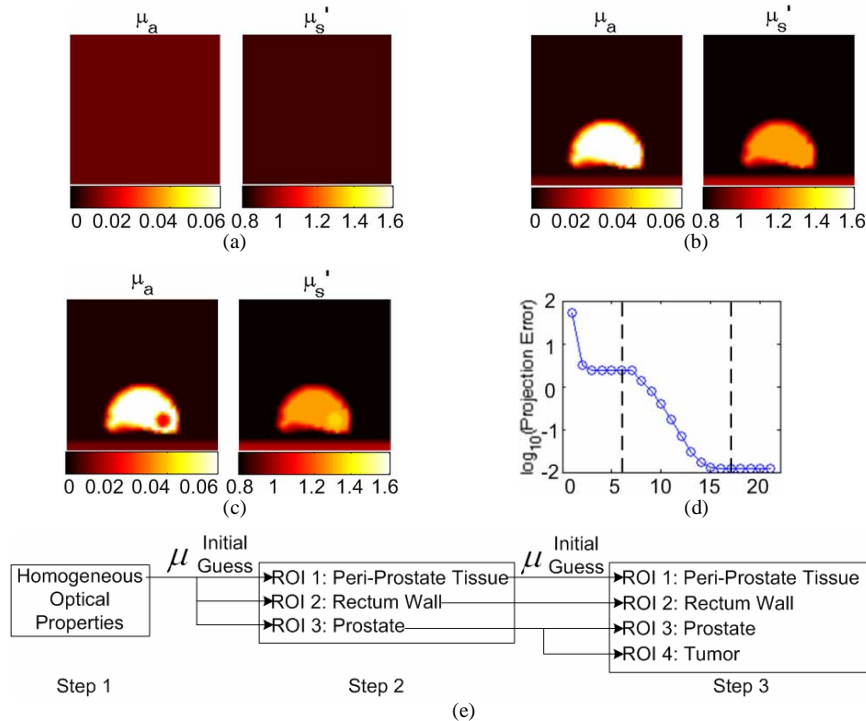


Fig. 7. The 3-step hierarchical reconstruction method (a) Step 1—one ROI for the entire volume; (b) step 2—three ROIs representing rectum wall, peri-prostate tissue, prostate; (c) step 3—four ROIs representing rectum wall, peri-prostate tissue, prostate, tumor; (d) change of the overall projection error, where the dash lines separate the converging of the three steps in (a)—(c); (e) block chart of the hierarchical initial guess assignment. [Unit in (a)---(c):  $\text{mm}^{-1}$ ]

### 3.4 Validation of the hierarchical spatial prior method

Recently Li et al. reported simulation results for trans-rectal optical tomography in the context of using MRI anatomic information [27], which is referred to as “NIR/MRI” in the following text. The proposed hierarchical spatial *prior* method is evaluated using the same probe geometry, prostate geometry and the optical properties (also in Table 1) presented in the NIR/MRI work. The size and depth of the tumor for simulation were not specified in the NIR/MRI work, but a tumor with diameter of 10 mm and a depth of 15mm from the planar probe surface is considerably close to the one presented in the NIR/MRI paper. The NIR/MRI

work also indicated the challenge of reconstruction that may be due to the local minimum. The authors set an arbitrary searching range for the optical properties ( $\mu_a$ :0-0.1 mm<sup>-1</sup>,  $\mu_s$ :0-2 mm<sup>-1</sup>), and in 4 sets of the results, 3 of the tumor absorption value reached the limits and were stopped from further iteration, whereas the 4<sup>th</sup> value converged at a value more than 2 folds of the set value.

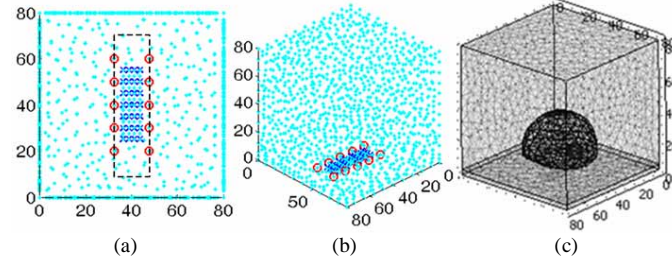


Fig. 8. The FEM mesh generated by following the geometry in NIR/MRI paper: (a) the geometry of the optodes, where the dash rectangle delineates the dimension of the NIR array that will be evaluated later for integration with US; (b) the 3-d view of the optodes and the imaging volume; (c) FEM containing the prostate and the tumor. [Unit: mm]

In the NIR/MRI work, a stand-alone trans-rectal NIR probe is simulated. The stand-alone NIR probe could have contained more optode channels incorporated than a TRUS-coupled NIR probe. In the NIR/MRI work, the best result is deducted for 10 sources and 28 detectors, which is used to evaluate the hierarchical method. The NIR probe geometry and the imaging domain of the NIR/MRI work are re-plotted in Fig. 8 for clarification and the hierarchical method is also preformed in transverse-view as did the NIR/MRI work. A 1% noise is also used in both methods assuring the consistency of measurement data.

Table 2. Reconstruction of a prostate tumor of negative contrast with respect to the prostate

	$\mu_a$ (mm <sup>-1</sup> )				$\mu_s$ (mm <sup>-1</sup> )			
Regions	Surrounding Tissue	Rectum Wall	Prostate	Tumor	Surrounding Tissue	Rectum Wall	Prostate	Tumor
Set value	0.002	0.01	0.06	0.02	0.8	1	1.27	1.6
NIR/MRI	0.0025	0.01	0.0575	0.0448	0.8324	1	1.339	1.075
3-step	0.002	0.0099	0.06	0.0208	0.8012	1.0028	1.2824	1.3495

Table 3. Reconstruction of a prostate tumor of positive contrast with respect to the prostate

	$\mu_a$ (mm <sup>-1</sup> )				$\mu_s$ (mm <sup>-1</sup> )			
Regions	Surrounding Tissue	Rectum Wall	Prostate	Tumor	Surrounding Tissue	Rectum Wall	Prostate	Tumor
Set value	0.002	0.01	0.006	0.02	0.8	1	1.27	1.6
3-step	0.0020	0.0100	0.0061	0.0163	0.7998	0.9997	1.2863	1.2434

Table 2 lists the results of the hierarchical method in comparison with those given in NIR/MRI paper. The hierarchical method (listed as “3-step” in the table), as expected, slightly outperforms the NIR/MRI method in terms of the accuracy of recovering optical properties. The results of recovering a target of positive absorption contrast are listed in Table 3 using the NIR/MRI probe geometry and our proposed 3-step method. The case of reconstructing a target with positive absorption contrast is not presented in the NIR/MRI paper, therefore only

the 3-step method is presented in Table 3 for comparison with the set values. In Table 3 the absorption coefficient of prostate is set much lower than that in Table 2 but the tumor optical properties are kept the same as those in Table 2. It is found that if the absorption of prostate in Table 3 is kept the same as in Table 2, the positive absorption target can hardly be reconstructed. The choice of lower prostate absorption is for testing our hierarchical method and the values may be much lower than the values reported of prostate [19-22]. It is noted that the reported values of prostate absorption coefficient vary in literatures where the measurements were taken either from *in vitro* tissue or from *in vivo* tissue using invasive methods. The absorption coefficient of intact or native prostate is in fact unknown, and is likely to be lower than the values reported in literatures.

The reconstructed images for targets of both negative and positive contrasts are listed in Fig. 9. These results demonstrate the capability of our hierarchical spatial *prior* method in reconstructing prostate lesion with either negative or positive absorption contrast.

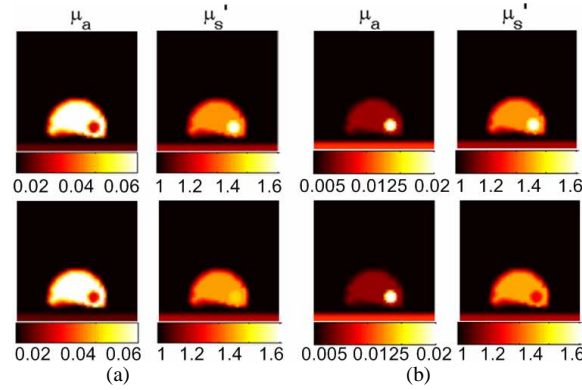


Fig. 9. Reconstructed images for a target with absorption contrast: (a) negative contrast (b) positive contrast. Top row: target setting; Bottom row: reconstructed image. [Unit:  $\text{mm}^{-1}$ ]

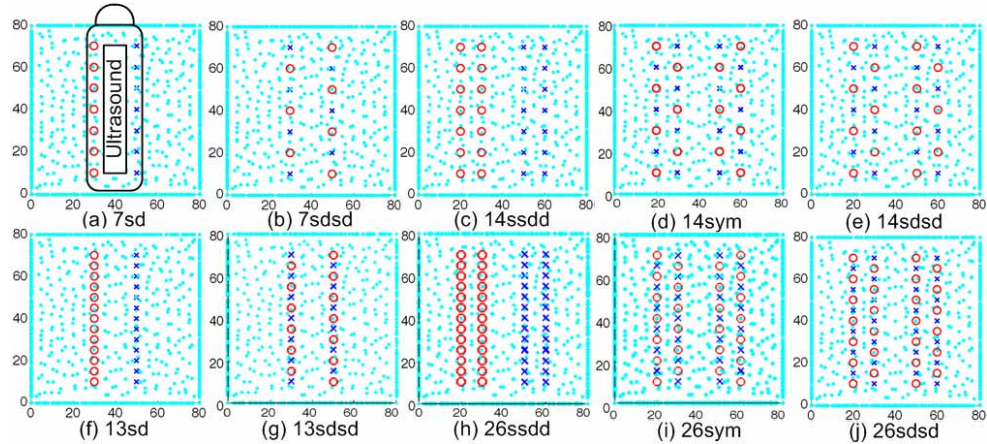


Fig. 10. NIR array designs. The dimension of the sagittal TRUS is shown in (a). The number of the Fig. caption denotes the number of optodes on each lateral side of the TRUS as is depicted in (a). “sd” denotes one line of source and one line of detector; “ssdd” denotes two lines of source and two lines of detector; “sdsd” denotes mixed source/detector in one line; “sym” denotes symmetric distribution of the optodes with respect to the sagittal TRUS. [Unit: mm]

#### 4. Assessment of NIR applicator designs for coupling NIR with TRUS

It is stated previously that an NIR array of dual-line geometry is feasible for concurrent trans-rectal NIR/US imaging considering the space limitation when coupling NIR with TRUS transducer for endo-rectal application. Based on the fabrication constraints, we have also suggested that each line array consist of 7 channels. The 7 channels could be exclusively source or detector as shown in Fig. 10(a), or interspersed source/detector as in Fig. 10(b). There are certainly a number of NIR geometries that can be coupled to TRUS sagittal transducer if not-limited by difficulties in fabrication or endo-rectal use. Compared with the geometry in Fig. 10(a), more channels could be added to each line-array as shown in Fig. 10(f), more lines can be added as shown in Fig. 10(c), or more lines and more channels added as in Fig. 10(h). More options are also listed in Fig. 10.

The array in Fig. 10(a) is the most desirable in terms of the fabrication easiness and endo-rectal applicability. The designs in Fig. 10(a), (b), (f) and (g) correspond to an NIR probe with a minimum lateral dimension of 20mm. The designs in Fig. 10(c)-(e) and (h-j) correspond to NIR probe with a minimum 40mm lateral dimension which is not suitable for endo-rectal use. The geometries in Fig. 10(a)–(e) represent a 10mm spacing between the closest optodes, and the geometries in Fig. 10(f)–(j) require a 5mm spacing between the closest optodes. The smaller spacing in Fig. 10(f)–(j) will be challenging for fabrication considering the number of fiber channels and the side-firing configuration if the probe is to be integrated to TRUS probe unless the internal structural of the TRUS probe can be altered.

##### 4.1 Sensitivity comparison

The sensitivities of all the 10 configurations of Fig. 10 are compared in Fig. 11. The mesh in Fig. 3 with homogeneous optical properties ( $\mu_a = 0.01\text{mm}^{-1}$  and  $\mu_s' = 1.0\text{mm}^{-1}$ ) is used for the sensitivity calculation. The sensitivity in Fig. 10 is evaluated at the lines identical to those in Fig. 4. Only the absorption sensitivity is evaluated.

The observations made from Fig. 11 are: (1) increasing the spatial dimension of source-detector array generally improves the sensitivity; (2) increasing the number of source-detector pairs generally improves the sensitivity, as demonstrated previously [43]; (3) interspersed source-detector layout may have slightly wider lateral sensitivity but is comparable to non-dispersed source-detector layout for other imaging views; (4) the geometry of 26ssdd (the upper thicker line) has the best sensitivity feature among the 10 geometries, therefore it can be used as a standard to evaluate the simple geometry of 7sd (the lower thicker line).

##### 4.2 Comparison between the 7sd design and the 26ssdd design

The 7sd design represents an array which is less challenging in fabrication and more practical for endo-rectal use. The 26ssdd geometry is impractical for endo-rectal application, difficult to fabricate, but has the best performance among the designs listed. It is shown in Fig. 11 that the sensitivity of 7sd design is approximately 10dB lower than that of 26ssdd in the specified longitudinal, lateral, and depth directions. Quantitative comparison of the performance is conducted between these two geometries for representative target variations. The optical properties listed in Table 2 (set values) are used for these comparisons.



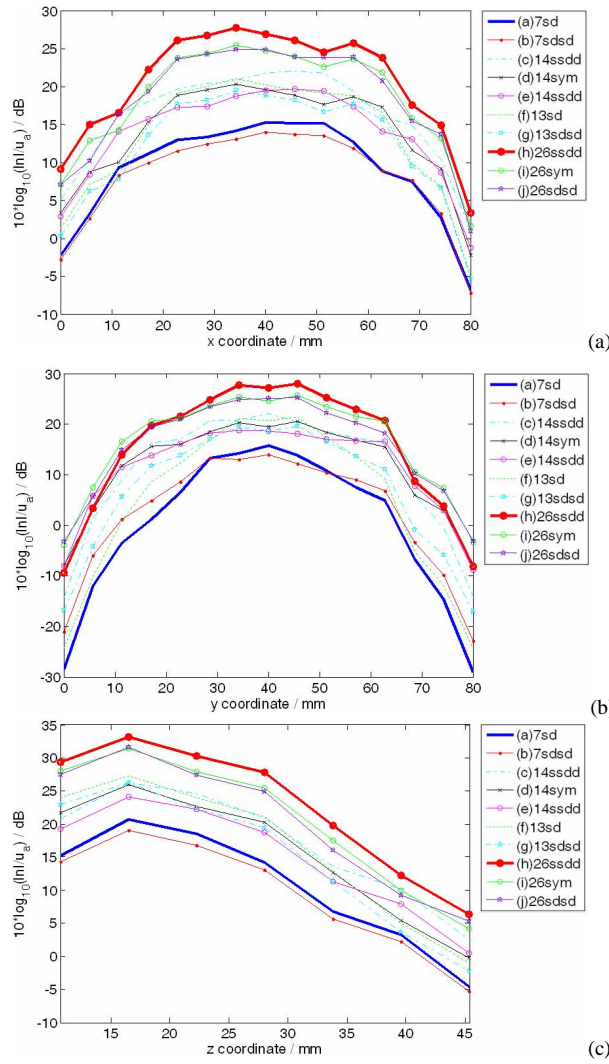


Fig. 11 Sensitivity comparison: (a) longitudinal direction, (b) lateral direction, (c) depth direction. The upper thicker line corresponds to the configuration (h) in Fig. 10, and the lower thicker line corresponds to the desired configuration (a) in Fig. 10.

#### 4.2.1 Reconstruction accuracy versus target longitudinal location

A target of 10mm in diameter is placed at the middle-sagittal plane of  $y=40\text{mm}$ ,  $z=26\text{mm}$ , and varied in longitudinal coordinates from  $x=25$  to  $55\text{mm}$  with a step of  $5\text{mm}$  (Fig. 12(a)). The optical properties reconstructed by the two geometries are plotted versus the true values in Fig. 12(b) and (c). The optical properties recovered by 26ssdd and 7sd designs are close to each other at most of the longitudinal locations, but the 7sd design shows a larger variation in the recovered absorption contrast at  $x=30\text{mm}$  and  $x=50\text{mm}$  compared to other positions. This may be related to fewer source-detector pairs that contribute to the target detection when close to the boundary or the existence of any irregular elements in the mesh.

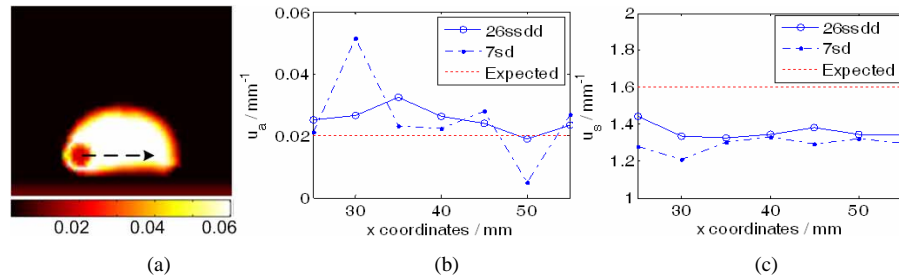


Fig. 12. Comparison of two geometries for a target varying in longitudinal location in the middle-sagittal plane: (a) illustration of the target location change [Unit: mm<sup>-1</sup>]; (b) comparison of absorption coefficient reconstruction; (c) comparison of reduced scattering coefficient reconstruction

#### 4.2.2 Reconstruction accuracy versus target depth

A target of 10mm in diameter is placed at the middle-sagittal plane at  $x=40$ mm,  $y=40$ mm, and the depth is varied from  $z=25$  to 40mm at a step of 2.5mm (the last data point is simulated at  $z=39$ mm as at 40mm the target is out of the prostate) (Fig. 13(a)). The reconstructed optical properties are plotted in Fig. 13(b) and (c). The 26ssdd configuration outperforms the 7sd one again, however beyond  $z=30$ mm, both designs are incapable of recovering the absorption coefficient of the target from the prostate background. This depth limitation is related to the maximum span of the NIR array, the absorption coefficient of the prostate, and the size of the target. For a larger target with a diameter of 14mm, it is verified that the target may be resolved up to 36mm depth from the NIR array in comparison to 30mm for a target of 10mm diameter. A potentially smaller absorption coefficient of intact prostate may also increase the depth limit of target detection due to an increase in sensitivity.

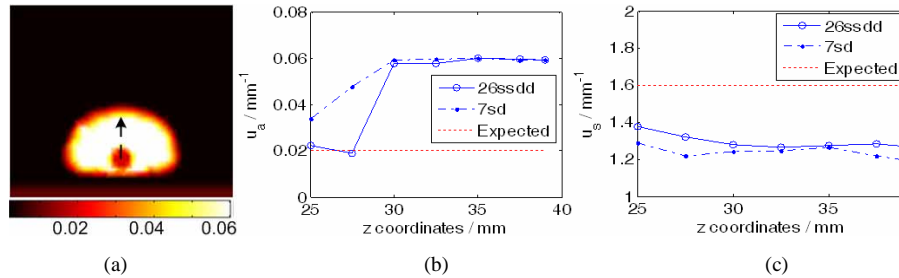


Fig. 13. Comparison of two geometries for a target varying in depth in the middle-sagittal plane: (a) illustration of the target location change [Unit: mm<sup>-1</sup>]; (b) comparison of absorption coefficient reconstruction; (c) comparison of reduced scattering coefficient reconstruction

#### 4.2.3 Reconstruction accuracy versus target size

A target is placed at middle-sagittal plane of  $x=40$ mm,  $y=40$ mm and  $z=26$ mm, and the diameter is varied from 4mm to 14mm with a step of 1mm. The target diameter change is illustrated in Fig. 14(a). The reconstructed optical properties are shown in Fig. 14(b) and (c). It is clear that the larger the target, the better the accuracy of reconstruction. The 26ssdd can recover the absorption contrast of the target when the diameter is greater than 6mm and the 7sd can recover the target for target diameter greater than 8mm.

These comparisons suggest that the 7sd design is inferior to the 26ssdd design, especially for the reconstruction of absorption properties. However, the accuracy of reconstructing scattering properties by the 7sd design is close to that of 26ssdd. Considering the challenges in trans-rectal NIR probing for coupling with TRUS, it is fair to develop and test the instrumentation with the 7sd design.



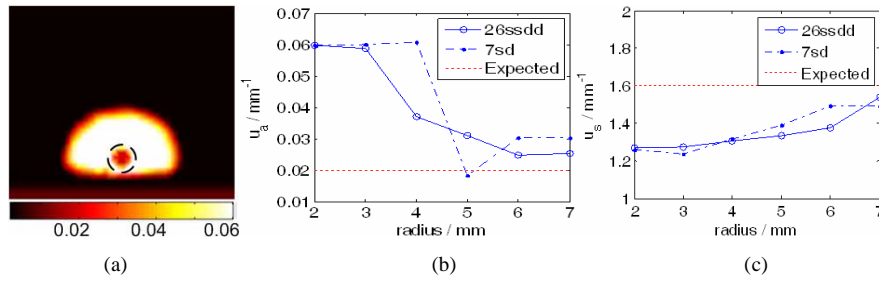


Fig. 14. Comparison of two geometries for a target varying in size in the middle-sagittal plane: (a) illustration of the target size change [Unit: mm<sup>-1</sup>]; (b) comparison of absorption coefficient reconstruction; (c) comparison of reduced scattering coefficient reconstruction

#### 4.3 Capability of recovering two targets by the 7sd design in sagittal plane

Capability of differentiating two targets is of particular relevance to prostate cancer imaging owing to the existence of secondary or multifocal tumors [44-46]. The multiple lesions may fall into the same TRUS field-of-view (FOV), or one falls outside the TRUS FOV. For the former case, the US *prior* could be used to guide NIR reconstruction of both targets. For the latter case, as NIR actually performs 3-D imaging it may interrogate the out-of-plane target and help redirecting the US to that target. In this section, however, we investigate only the former case of having two targets in the same sagittal plane. This requires implementing the multi-target location information in the last step of the hierarchical spatial *prior* routine. The following simulations are conducted with the 7sd probe design only.

##### 4.3.1 Reconstruction of two targets located at the same depth in sagittal plane

Figure 15 shows two 10mm-diameter regions being added to the prostate, at coordinates (25, 40, 26) and (55, 40, 26), respectively. In Fig. 15(a) only one region has optical contrast, and in Fig. 15(b) both regions have optical contrasts. In both cases the optical contrast can be reconstructed with good accuracy, as is shown in Table 4. The  $\mu_a$  of the target with true optical contrast is reconstructed within  $\pm 20\%$  of the set value and  $\mu_s$  can be reconstructed within  $\pm 23\%$  of the set values. The target with no optical contrast is reconstructed with some artifacts, nevertheless, the target with optical contrast can be easily differentiated from the one without.

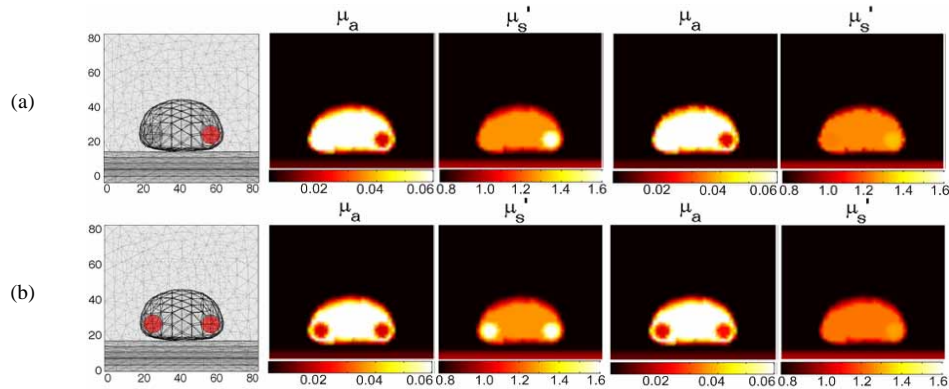


Fig. 15. Two suspicious regions at the same depth [Units: mm and mm<sup>-1</sup>]

Table 4. Comparison of reconstructed optical properties ( $\text{mm}^{-1}$ ) in Fig. 15

$\mu_a(\text{mm}^{-1})$						
Fig.	Regions	Peri-prostate	Rectum	Prostate	Target 1	Target 2
(a)	Set value	0.002	0.01	0.06	0.06	0.02
	Reconstructed	0.002	0.0101	0.0601	0.0778	0.0208
(b)	Set value	0.002	0.01	0.06	0.02	0.02
	Reconstructed	0.002	0.01	0.0597	0.0207	0.024
$\mu_s'(\text{mm}^{-1})$						
Fig.	Regions	Peri-prostate	Rectum	Prostate	Target 1	Target 2
(a)	Set value	0.8	1.0	1.27	1.27	1.6
	Reconstructed	0.7995	0.9935	1.261	1.2187	1.3216
(b)	Set value	0.8	1.0	1.27	1.6	1.6
	Reconstructed	0.8007	0.9953	1.2343	1.2302	1.2837

#### 4.3.2 Reconstruction of two targets located at different depth in sagittal plane

Two targets of 10mm diameter are added in the prostate at coordinates of (25, 40, 28) and (55, 40, 24), respectively. Figure 16 shows the reconstructed images for the case of both targets having negative contrast and the reconstructed values are listed in Table 5.

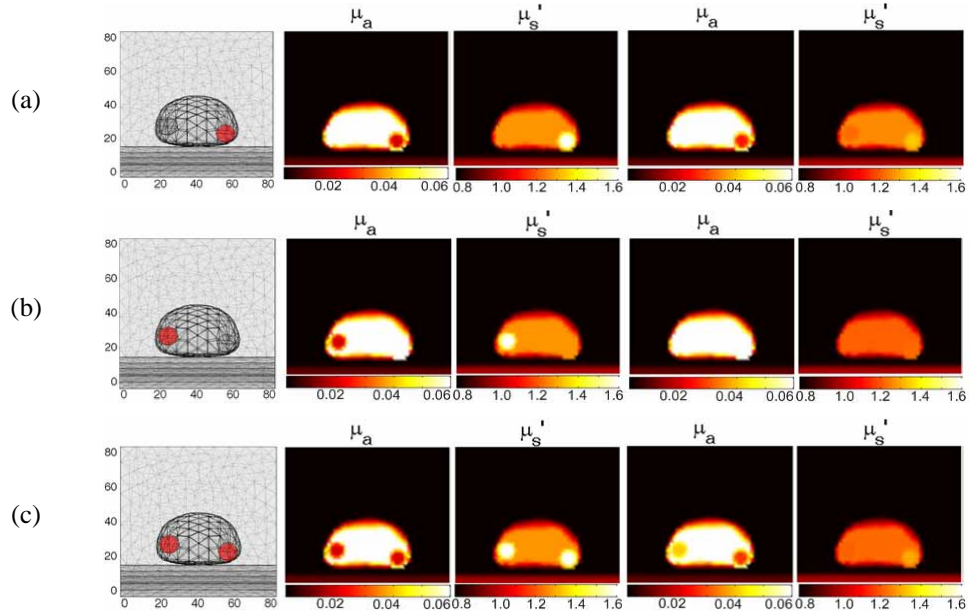


Fig. 16. Two targets at different depths: negative contrast cases [Unit: mm and  $\text{mm}^{-1}$ ]

Table 5. Comparison of reconstructed optical properties ( $\text{mm}^{-1}$ ) in Fig. 16

$\mu_a$ ( $\text{mm}^{-1}$ )						
Fig.	Regions	Peri-prostate	Rectum	Prostate	Region 1	Region 2
(a)	Set value	0.002	0.01	0.06	0.06	0.02
	Reconstructed	0.002	0.01	0.0594	0.0674	0.0252
(b)	Set value	0.002	0.01	0.06	0.02	0.06
	Reconstructed	0.002	0.0101	0.0597	0.0592	0.0607
(c)	Set value	0.002	0.01	0.06	0.02	0.02
	Reconstructed	0.002	0.01	0.0596	0.0402	0.0276
$\mu_s$ ( $\text{mm}^{-1}$ )						
Fig.	Regions	Peri-prostate	Rectum	Prostate	Region 1	Region 2
(a)	Set value	0.8	1.0	1.27	1.27	1.6
	Reconstructed	0.8009	0.9977	1.2538	1.2167	1.3286
(b)	Set value	0.8	1.0	1.27	1.6	1.27
	Reconstructed	0.8015	0.9931	1.2102	1.2179	1.2083
(c)	Set value	0.8	1.0	1.27	1.6	1.6
	Reconstructed	0.8015	0.9956	1.2177	1.2024	1.2962

When the target is at a depth of 24mm, the  $\mu_a$  and  $\mu_s$  can be reconstructed within  $\pm 20\%$  and  $\pm 25\%$  of the set values, respectively. However, a target at 28mm depth cannot be reconstructed. This is due to the prostate's high absorption coefficient of  $0.06\text{mm}^{-1}$ . When the prostate absorption coefficient is reduced to  $0.006\text{mm}^{-1}$  which will provide positive optical contrast in the two target regions, both targets can be recovered as shown in Fig. 17 and Table 6. The  $\mu_a$  of the target can be reconstructed within  $\pm 5\%$  of the set value, while the  $\mu_s$  is still reconstructed within  $\pm 23\%$  of the expected values.

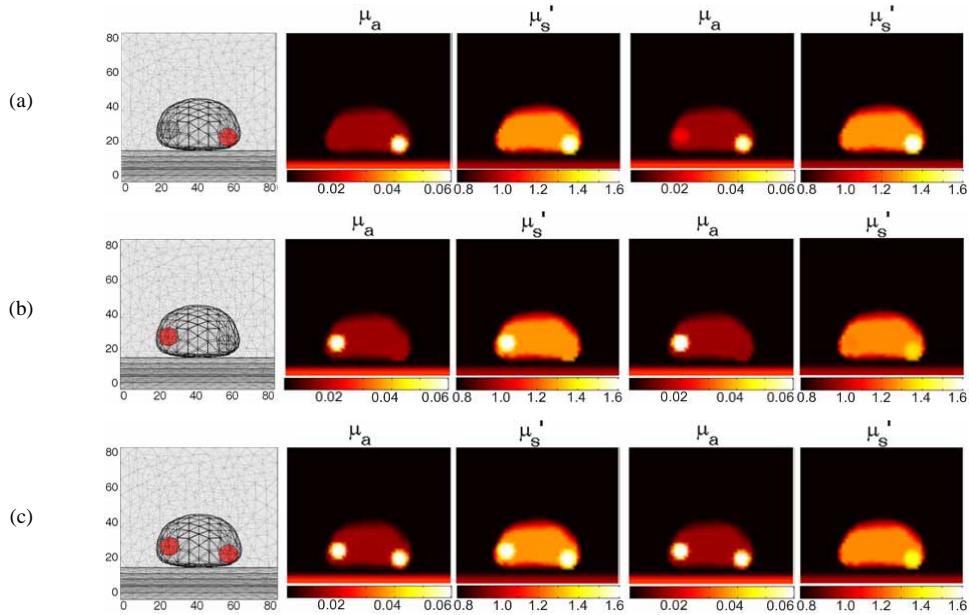


Fig. 17. Two targets at different depths: positive contrast cases [Unit: mm and  $\text{mm}^{-1}$ ]

Table 6. Comparison of reconstructed optical properties ( $\text{mm}^{-1}$ ) in Fig. 17

$\mu_{a(\text{mm}^{-1})}$						
Fig.	Regions	Peri-prostate	Rectum	Prostate	Region 1	Region 2
(a)	Set value	0.002	0.01	0.006	0.006	0.02
	Reconstructed	0.002	0.0101	0.006	0.0083	0.0191
(b)	Set value	0.002	0.01	0.006	0.02	0.006
	Reconstructed	0.002	0.0101	0.006	0.0116	0.0058
(c)	Set value	0.002	0.01	0.006	0.02	0.02
	Reconstructed	0.002	0.0099	0.006	0.0208	0.0199
$\mu'_s (\text{mm}^{-1})$						
Fig.	Regions	Peri-prostate	Rectum	Prostate	Region 1	Region 2
(a)	Set value	0.8	1.0	1.27	1.27	1.6
	Reconstructed	0.7993	0.9934	1.2637	1.2689	1.6722
(b)	Set value	0.8	1.0	1.27	1.6	1.27
	Reconstructed	0.8008	0.993	1.259	1.2402	1.3586
(c)	Set value	0.8	1.0	1.27	1.6	1.6
	Reconstructed	0.8049	0.9979	1.2576	1.2538	1.424

## 5. Discussions

The scope of this work is to investigate the feasibility of trans-rectal NIR tomography of the prostate in the context of concurrent imaging with sagittal TRUS using combined endo-rectal NIR/US probe. Recently there have been considerable interests on trans-rectal NIR tomography to augment existing imaging modalities which cannot be validated without the development of an endo-rectal NIR applicator. With an endo-rectal applicator, trans-rectal NIR tomography of the prostate can be performed stand-alone. However, without a position correlation with a real-time anatomic imaging modality such as TRUS, the images obtained by trans-rectal NIR would be difficult to interpret. Combining the NIR applicator with TRUS is a viable solution for accurate positioning of the NIR probe which would further enable using TRUS anatomy to guide the image reconstruction of trans-rectal NIR tomography. A variety of designs of NIR array for coupling with TRUS are possible, however, the NIR probe dimension and the number of NIR channels on the probe are quite limited.

The utilization of a hierarchical spatial *prior* is under the condition that the anatomic information of the prostate tumor can be extracted explicitly from TRUS. The prostate boundary can be well-delineated in TRUS, and so does a strongly hypo-echoic region indicating a suspicious lesion. This is when the NIR imaging may help determine if the suspicious lesion is malignant or benign based on optical contrasts [31]. However, since as many as 40% of the tumors may be seen as iso-echoic on TRUS, the utility or accuracy of this hierarchical imaging approach is hindered when TRUS images do not specify a suspicious region, or when it is difficult to define the spatial extent of a suspicion region in TRUS. Under these circumstances, the third step of the proposed hierarchical image reconstruction routine may be performed by element-based reconstruction within the prostate instead of region-based reconstruction for the prostate. Such approach is proven effective based on our initial investigations, but the accuracy and robustness may be affected by the depth-dependent sensitivity of the endo-rectal NIR probe and the relatively small number of source/detector channels that may be engineered on the NIR probe. More dedicated investigations could be conducted when the trans-rectal NIR/US approach is experimentally demonstrated. Prostate trans-rectal optical imaging is a relatively new area, thus it is imperative to focus the initial approach of trans-rectal NIR/US on characterizing lesions identifiable on TRUS.

Characterizing lesions marginally suspicious to TRUS or iso-echoic on TRUS may become less-challenging when the knowledge on trans-rectal NIR tomography of lesions most suspicious on TRUS is available.

The simulations studies presented here are largely based on setting the absorption properties of prostate at a high level of  $0.06\text{mm}^{-1}$ . This is significantly larger than that of breast tissue, and it is this parameter that dominates the detection depth of trans-rectal NIR tomography for the NIR array being discussed. Recent studies indicate that improved measurement condition, such as suppressing the bleeding interference, may lead to a lower absorption value of the prostate [22]. If the prostate is measured at its intact or native states by modalities such as trans-rectal optical tomography, an even lower absorption coefficient of the prostate may be obtained. A lower absorption coefficient will allow the same NIR array to detect deeper targets. In fact, a TRUS-coupled trans-rectal NIR tomography may not only help characterize lesions suspicious to TRUS, but also help quantify the optical properties of intact prostate that are unavailable so far.

## 6. Conclusions

The feasibility of imaging the prostate using a TRUS-coupled NIR applicator is investigated by simulation. A hierarchical iteration algorithm is first developed in order to incorporate the TRUS spatial *prior* more reliably into the trans-rectal NIR image reconstruction. This hierarchical reconstruction method uses a cascaded initial-guess approach to mitigate the local minimum problem common to NIR tomography reconstruction. It is shown that trans-rectal optical tomography based on this method is reliable. This hierarchical reconstruction method is then utilized to evaluate a number of designs of NIR applicator that may be integrated with a sagittal TRUS transducer. A configuration of the endo-rectal NIR applicator is proposed, that contains single line of optode on each lateral side of the sagittal TRUS transducer, with 20mm lateral separation between the two line arrays and 10 mm longitudinal spacing among the total 7 channels on each line-array. The performance of this simple NIR array design is evaluated for the imaging of single tumor target in prostate by comparing with a much more complicated design that is impractical for endo-rectal application. The simple NIR array design is also evaluated for imaging of two targets in the prostate. Results suggest that trans-rectal imaging of the prostate is feasible by coupling this simple NIR array with TRUS.

The following Part-II paper presents the instrumentation of a TRUS-coupled endo-rectal NIR array and demonstrates trans-rectal optical tomography of the prostate by the combined endo-rectal NIR/US applicator. The endo-rectal NIR array has incorporated the design suggested by Fig. 10(a). Concurrent trans-rectal imaging is acquired in the same sagittal plane by both US and NIR optical tomography. The real-time TRUS is used for accurate positioning of the endo-rectal NIR applicator and for guiding NIR image reconstruction with the spatial *a priori* information. Tests on phantoms and tissues using the combined trans-rectal NIR/US imager demonstrate that optical contrast may be recovered by endo-rectal NIR imaging only but with improved accuracy when the TRUS spatial *prior* is incorporated. Trans-rectal imaging of a healthy canine prostate *in situ* administered with tissue contrast validates the endo-rectal utility of the NIR/US probe as well as the hierarchical method for TRUS guided trans-rectal NIR image reconstruction.

## Acknowledgments

This work has been supported by the Prostate Cancer Research Program of the U.S. Army Medical Research Acquisition Activity (USAMRAA), 820 Chandler Street, Fort Detrick MD, 21702-5014, through grant #W81XWH-07-1-0247. The content of the information does not necessarily reflect the position or the policy of the USARAA, and no official endorsement should be inferred. Comments and questions may be directed to Daqing Piao at [daqing.piao@okstate.edu](mailto:daqing.piao@okstate.edu).

# Trans-rectal ultrasound-coupled near-infrared optical tomography of the prostate

## Part II: Experimental demonstration

Zhen Jiang,<sup>1</sup> Daqing Piao,<sup>1\*</sup> Guan Xu,<sup>1</sup> Jerry W. Ritchey,<sup>2</sup> G. Reed Holyoak,<sup>3</sup> Kenneth E. Bartels,<sup>3</sup> Charles F. Bunting,<sup>1</sup> Gennady Slobodov,<sup>4</sup> Jerzy S. Krasinski<sup>1</sup>

<sup>1</sup>*School of Electrical and Computer Engineering, Oklahoma State University, Stillwater, OK 74078 USA*

<sup>2</sup>*Department of Veterinary Pathobiology, Oklahoma State University, Stillwater, OK 74078 USA*

<sup>3</sup>*Department of Veterinary Clinical Sciences, Oklahoma State University, Stillwater, OK 74078 USA*

<sup>4</sup>*Department of Urology, University of Oklahoma Health Science Center, Oklahoma City, OK 73104 USA*

\*Corresponding author: [daqing.piao@okstate.edu](mailto:daqing.piao@okstate.edu)

**Abstract:** We demonstrate trans-rectal optical tomography of the prostate using an endo-rectal near-infrared (NIR) applicator integrated with a trans-rectal ultrasound (TRUS) probe. The endo-rectal NIR applicator incorporated a design presented in our previously reported work. A continuous-wave NIR optical tomography system is combined with a commercial US scanner to form the dual-modality imager. Sagittal trans-rectal imaging is performed concurrently by endo-rectal NIR and TRUS. The TRUS ensures accurate positioning of the NIR applicator as well as guides NIR image reconstruction using the spatial prior of the target. The use of a condom, which is standard for TRUS, is found to have minimal effect on trans-rectal NIR imaging. Tests on avian tissues validates that NIR imaging can recover the absorption contrast of a target, and its accuracy is improved when the TRUS spatial prior is incorporated. Trans-rectal NIR/US imaging of a healthy canine prostate in situ is reported.

©2008 Optical Society of America

**OCIS codes:** (170.3880) Medical and biological imaging; (170.6960) Tomography; (170.7230) Urology; (170.1610) Clinical applications.

---

### References and links

1. G. Xu, D. Piao, C. H. Musgrove, C. F. Bunting, and H. Dehghani, "Trans-rectal ultrasound coupled trans-rectal optical tomography of the prostate Part I: Simulations," Accepted for publication in Opt. Express.
2. G. D. Grossfeld and P. R. Carroll, "Prostate cancer early detection: a clinical perspective," Epidemiol. Rev. **23**, 173-80 (2001).
3. A. C. Loch, A. Bannowsky, L. Baeurle, B. Grabski, B. König, G. Flier, O. Schmitz-Krause, U. Paul, and T. Loch, "Technical and anatomical essentials for transrectal ultrasound of the prostate," World J. Urol. **25**, 361-366 (2007).
4. C. R. Porter, "Does the number of prostate biopsies performed affect the nature of the cancer identified?" Nat. Clin. Pract. Urol. **4**, 132-133 (2007).
5. V. Scattoni, A. Zlotta, R. Montironi, C. Schulman, P. Rigatti, and F. Montorsi, "Extended and saturation prostatic biopsy in the diagnosis and characterisation of prostate cancer: a critical analysis of the literature," Eur. Urol. **52**, 1309-1322 (2007).
6. B. Spajic, H. Eupic, D. Tomas, G. Stimac, B. Kruslin, and O. Kraus, "The incidence of hyperechoic prostate cancer in transrectal ultrasound-guided biopsy specimens," Urology **70**, 734-737 (2007).
7. K. Shinohara, T. M. Wheeler, and P. T. Scardino, "The appearance of prostate cancer on transrectal ultrasonography: correlation of imaging and pathological examinations," J. Urol. **142**, 76-82 (1989).
8. B. Tromberg, J. Coquoz, O. Fishkin, J. B. Pham, T. Anderson, E. R. Butler, J. Cahn, M. Gross, J. D. Venugopalan, and D. Pham, "Non-invasive measurements of breast tissue optical properties using frequency-domain photon migration," Phil. Trans. R. Soc. Lond. B **352**, 661-668 (1997).
9. B. W. Pogue, S. P. Poplack, T. O. McBride, W. A. Wells, K. S. Osterman, U. L. Osterberg, and K. D. Paulsen, "Quantitative hemoglobin tomography with diffuse near-infrared spectroscopy: pilot results in the breast," Radiology **218**, 261-266 (2001).

10. V. Ntziachristos and B. Chance, "Probing physiology and molecular function using optical imaging: applications to breast cancer," *Breast Cancer Res.* **3**, 41-46 (2001).
11. R. Choe, A. Corlu, K. Lee, T. Durduran, S. D. Konecky, M. Grosicka-Koptyra, S. R. Arridge, B. J. Czerniecki, D. L. Fraker, A. DeMichele, B. Chance, M. A. Rosen, and A. G. Yodh, "Diffuse optical tomography of breast cancer during neoadjuvant chemotherapy: a case study with comparison to MRI," *Med. Phys.* **32**, 1128-1139 (2005).
12. M. A. Franceschini, K. T. Moesta, S. Fantini, G. Gaida, E. Gratton, H. Jess, W. W. Mantulin, M. Seeber, P. M. Schlag, and M. Kaschke, "Frequency-domain techniques enhance optical mammography: initial clinical results," *Proc. Nat. Acad. Sci. USA* **94**, 6468-6473 (1997).
13. Q. Zhu, E. B. Cronin, A. A. Currier, H. S. Vine, M. Huang, N. Chen, and C. Xu, "Benign versus malignant breast masses: optical differentiation with US-guided optical imaging reconstruction," *Radiology* **237**, 57-66 (2005).
14. B. J. Tromberg, B. W. Pogue, K. D. Paulsen, A. G. Yodh, D. A. Boas, and A. E. Cerussi, "Assessing the future of diffuse optical imaging technologies for breast cancer management," *Med Phys.* **35**, 2443-51 (2008).
15. J. H. Ali, W. B. Wang, M. Zavallos, and R. R. Alfano, "Near infrared spectroscopy and imaging to probe differences in water content in normal and cancer human prostate tissues," *Technol. Cancer Res. Treat.* **3**, 491-497 (2004).
16. M. R. Arnfield, J. D. Chapman, J. Tulip, M. C. Fenning, and M. S. McPhee, "Optical properties of experimental prostate tumors in vivo," *Photochem. Photobiol.* **57**, 306-311 (1993).
17. T. C. Zhu, A. Dimofte, J. C. Finlay, D. Stripp, T. Busch, J. Miles, R. Whittington, S. B. Malkowicz, Z. Tochner, E. Glatstein, and S. M. Hahn, "Optical properties of human prostate at 732 nm measured in mediated photodynamic therapy," *Photochem. Photobiol.* **81**, 96-105 (2005).
18. T. Svensson, S. Andersson-Engels, M. Einarsdóttir, and K. Svanberg, "In vivo optical characterization of human prostate tissue using near-infrared time-resolved spectroscopy," *J. Biomed. Opt.* **12**, 014022 (2007).
19. M. Goel, H. Radhakrishnan, H. Liu, et al. "Application of near infrared multi-spectral CCD imager system to determine the hemodynamic changes in prostate tumor," in *OSA Biomedical Topical Meetings* (Optical Society of America, 2006), paper SH10.
20. X. Zhou and T. C. Zhu, "Image reconstruction of continuous wave diffuse optical tomography (DOT) of human prostate," in *Proc. the COMSOL Users Conference* (2006).
21. S. L. Jacques and M. Motamedi, "Tomographic needles and catheters for optical imaging of prostatic cancer," *Proc. SPIE* **2395**, 111-118 (1995).
22. C. Li, R. Liengsawangwong, H. Choi, and R. Cheung, "Using *a priori* structural information from magnetic resonance imaging to investigate the feasibility of prostate diffuse optical tomography and spectroscopy: a simulation study," *Med. Phys.* **34**, 266-274 (2007).
23. H. Dehghani, C. M. Carpenter, P. K. Yalavarthy, B. W. Pogue, and J. P. Culver, "Structural *a priori* information in near-infrared optical tomography," *Proc. SPIE* **6431**, 64310B1-7 (2007).
24. M. J. Holboke, B. J. Tromberg, X. Li, N. Shah, J. Fishkin, D. Kidney, J. Butler, B. Chance, and A. G. Yodh, "Three-dimensional diffuse optical mammography with ultrasound localization in a human subject," *J. Biomed Opt.* **5**, 237-247 (2000).
25. A. Li, E. L. Miller, M. E. Kilmer, T. J. Brulacchio, T. Chaves, J. Stott, Q. Zhang, T. Wu, M. Chorlton, R. H. Moore, D. B. Kopans, and D. A. Boas, "Tomographic optical breast imaging guided by three-dimensional mammography," *Appl. Opt.* **42**, 5181-90 (2003).
26. M. Guven, B. Yazici, X. Intes, and B. Chance, "Diffuse optical tomography with *a priori* anatomical information," *Phys. Med. Biol.* **50**, 2837-58 (2005).
27. D. Piao, H. Xie, W. Zhang, J. S. Kransinski, G. Zhang, H. Dehghani, and B. W. Pogue, "Endoscopic, rapid near-infrared optical tomography," *Opt. Lett.* **31**, 2876-2878 (2006).
28. N. Iftimia and H. Jiang, "Quantitative optical image reconstruction of turbid media by use of direct-current measurements," *Appl. Opt.* **39**, 5256-5261 (2000).
29. V. Ntziachristos, "Concurrent diffuse optical tomography, spectroscopy and magnetic resonance imaging of breast cancer," PhD Dissertation, University of Pennsylvania, Philadelphia, PA, 15-16 (2000).
30. R. C. Haskell, L. O. Svaasand, T. T. Tsay, T. C. Feng, M. S. McAdams, B. J. Tromberg, "Boundary conditions for the diffusion equation in radiative transfer," *J. Opt. Soc. Am. A* **11**, 2727-41 (1994).
31. R. Aronson, "Boundary conditions for diffusion of light," *J. Opt. Soc. Am. A* **12**, 2532-9 (1995).
32. D. Piao and B. W. Pogue, "Rapid near-infrared tomography for hemodynamic imaging using a low coherence wideband light source," *J. Biomed. Opt.* **12**, 014016 (2007).
33. H. Xu, "MRI-coupled broadband near-infrared tomography for small animal brain studies," Ph.D. Dissertation, Dartmouth College, Hanover, NH, 36-36 (2005).
34. S. Arridge, M. Cope, and D. Delpy, "The theoretical basis for the determination of optical pathlengths in tissue: temporal and frequency analysis," *Phys. Med. Biol.* Vol. 37, No 7, 1531-1560 (1992).
35. W. F. Cheong, S. A. Prahl, and A. J. Welch, "A review of the optical properties of biological tissues," *IEEE J. Quantum Electron.* **26**, 2166-2185 (1990).
36. H. Xie, "Dual-spectral endoscopic near-infrared optical tomography for assessment of hemoglobin concentration and oxygen saturation," Master Thesis, Oklahoma State University (2008).



37. A. H. Hielscher, R. E. Alcouffe, and R. L. Barbour, "Comparison of finite-difference transport and diffusion calculations for photon migration in homogeneous and heterogeneous tissues," *Phys. Med. Biol.* **43**, 1285-302 (1998).
38. Z. Yuan, Q. Zhang, E. Sobel, and H. Jiang, "Three-dimensional diffuse optical tomography of osteoarthritis: initial results in the finger joints," *J. Biomed. Opt.* **12**, 034001 (2007).
39. A. Custo, W. M. Wells 3rd, A. H. Barnett, E. M. Hillman, and D. A. Boas, "Effective scattering coefficient of the cerebral spinal fluid in adult head models for diffuse optical imaging," *Appl. Opt.* **45**, 4747-55 (2006).
40. C. Xu, Q. Zhu, "Estimation of chest-wall-induced diffused wave distortion with the assistance of ultrasound," *Appl. Opt.* **44**, 4255-64 (2005).

## 1. Introduction

This is a continuation of previously reported work [1] whose objective is to demonstrate the feasibility of trans-rectal ultrasound (TRUS) coupled trans-rectal near-infrared (NIR) tomography of the prostate.

Prostate cancer screening is performed by measurement of serum prostate-specific antigen (PSA), digital rectal examination (DRE), and a combination of these tests [2]. When the suspicion of prostate cancer is raised by abnormal PSA and/or DRE, the diagnosis is made by biopsy performed under US guidance (most often by TRUS). Biopsy is also used to confirm neoplastic lesions and to determine their clinical significance for treatment planning [3]. The current standard of prostate biopsy is to routinely use 10 to 12 cores of tissue obtained throughout the prostate for the initial assessment [4]. It should be noted that the majority of biopsies are found to be negative, and in men with persistent suspicion of prostate cancer after several negative biopsies, more extensive protocols (>12 cores) up to saturation biopsy (24 cores) represent a necessary diagnostic procedure [5]. TRUS-guided prostate biopsy is performed following a "systematic sampling" strategy because less than 60% of neoplastic lesions appear hypoechoic on TRUS while most of the remaining neoplastic lesions appear isoechoic [6]. Also, TRUS does not reliably differentiate neoplastic from benign tumors [7].

We have suggested [1] that the accuracy of prostate biopsy may be improved if the TRUS imaging could be augmented with a functional or "surrogate" marker of a prostate tumor. Based on decades of research on cancer imaging [8-14] and prostate measurements [15-22], near-infrared (NIR) tomography, being non-ionizing and minimally-invasive similar to TRUS, has the potential of providing such functional or "surrogate" markers of prostate tumors. NIR optical tomography, if carried out trans-rectally, may improve the specificity of TRUS imaging such that prostate biopsies could be directed to the most suspicious lesions.

In the first paper of this two part series [1] we discussed the challenges of trans-rectal optical tomography, particularly the fabrication of an endo-rectal NIR applicator for integrating with TRUS. Specifically, since a TRUS-coupled endo-rectal NIR applicator requires deploying many optodes in a very limited space. We suggested [1] that arranging optodes longitudinally is feasible and the configuration would allow interrogating deep prostate tissue in a sagittal imaging geometry. Coupling endo-rectal NIR to TRUS obtains functional information otherwise unavailable from TRUS alone. Coupling endo-rectal NIR to TRUS also renders accurate and real-time anatomic information from TRUS with which to correlate NIR. The structural information obtained from TRUS may further provide the needed spatial *prior* [14, 23-26] to improve the accuracy of NIR image reconstruction. In that initial paper we further suggested [1] an array configuration of the endo-rectal NIR applicator for direct integration with a TRUS transducer.

The work presented here details the development of an endo-rectal NIR probe built on our previous work [1] and demonstrates TRUS-coupled trans-rectal NIR tomography of the prostate. It validates that trans-rectal NIR tomography helps characterize a target identified by TRUS, and the accuracy of quantitative imaging of a target by trans-rectal NIR tomography is improved when the TRUS spatial *prior* is incorporated. TRUS-coupled trans-rectal optical



tomography of a canine prostate *in situ* is performed, indicating the utility of this approach for *in vivo* imaging.

## 2. Instrumentation

### 2.1 Development of a TRUS-coupled NIR applicator for trans-rectal optical tomography

The integrated sagittal-imaging trans-rectal NIR/US applicator consists of a custom-built NIR probe and a commercial bi-plane TRUS transducer, as shown in Fig. 1. The bi-plane TRUS probe is equipped with a proximal 7.5MHz sagittal-imaging transducer and a distal 5MHz transverse-imaging transducer. The sagittal TRUS transducer occupies a 60mm×10mm window. The diameters of the sagittal and transverse imaging sections of the TRUS probe are 18mm and 20mm, respectively. Adapting to the un-even TRUS cross-section, the NIR applicator is fabricated to a cap-shape and attached to the TRUS probe (Fig. 1(a) ~ (e)). The NIR array substrate was machined from a black polycarbonate material to minimize the surface reflection. This substrate was then connected to an aluminum bracket and securely fastened to the TRUS handle using a bottom clamp. The rectangular TRUS handle (Fig. 1(f) ~ (g)) ensured aligning the NIR applicator to the TRUS transducer. A slot of 60mm×10mm was opened up in the NIR applicator to expose the sagittal TRUS transducer.

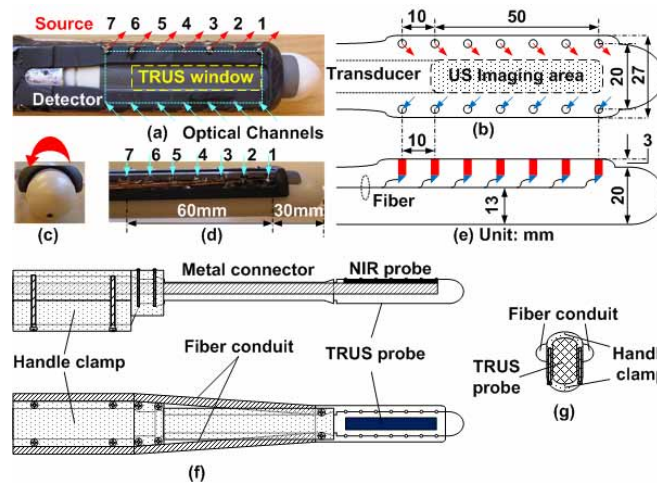


Fig. 1. The combined trans-rectal NIR/US probe: (a) top-view; (b) top-view dimension; (c) front-view; (d) side-view; (e) side-view dimension; (f) side and top views of the NIR/US alignment method; (g) rear-view of the NIR/US alignment method.

The geometry of the NIR array follows the design we previously described [1]. The NIR probe consists of two linear-arrays, one for the source and the other for the detector, separated by 20mm and placed on each side of the sagittal TRUS transducer. Each linear-array consists of 7 channels spaced 10mm apart and covering 60mm in length. The 60mm long NIR array is aligned precisely with the 60mm window of the sagittal TRUS transducer. The sagittal TRUS transducer actually has a longitudinal field-of-view (FOV) of 50mm. Therefore the NIR channels 1 to 6 on each linear-array match with the length of the sagittal TRUS transducer, and the NIR channel 7 of each linear-array is displaced longitudinally 10mm from the sagittal TRUS transducer.

A metal-coated 600μm-core diameter fiber (Oxford Electronics) is chosen for its thin cladding and mechanical strength. The 7 fibers of each linear-array are packaged into one groove of ~4mm×4mm in cross-section formed in the black substrate. Bending the fiber inside the small groove for side-firing at the probe surface is impractical. Instead micro-optics components are used for deflecting the light side-ways. As shown in Fig. 2, each source channel includes 2 gradient-index (GRIN) lenses and 1 prism attached to the fiber while each

detector channel has 1 GRIN lens and 1 prism attached to the fiber. The GRIN lens (Newport Corporation) has a pitch of 0.25, a diameter of 1mm, a length of 2.61mm, and a numerical aperture of 0.46. The prism is a coated 1mm right angle micro-prism (Tower Optics). Each fiber is polished and epoxied to a prism and a GRIN lens is attached to the other side of the micro-prism for illumination and detection at the probe surface. Each source channel has one GRIN lens attached to the proximal end of the fiber for coupling the emission of a superluminescent diode (SLD) using a spread-spectral-encoding configuration [27]. It is shown by ZEMAX (ZEMAX Development Co.) simulation that for collimated incident beam using a GRIN lens and a prism gives 38% more coupling than without the GRIN lens for a micro-prism of 80% reflection at NIR band that is typical for enhanced aluminum coating. A coupling efficiency improvement of 10%~15% is observed experimentally from the completed fiber channels. The overall coupling efficiencies of the 14 home-assembled fiber channels are shown in Table 1. The coupling efficiency is at about 50%, which could be improved if the assembly can be made more precise.

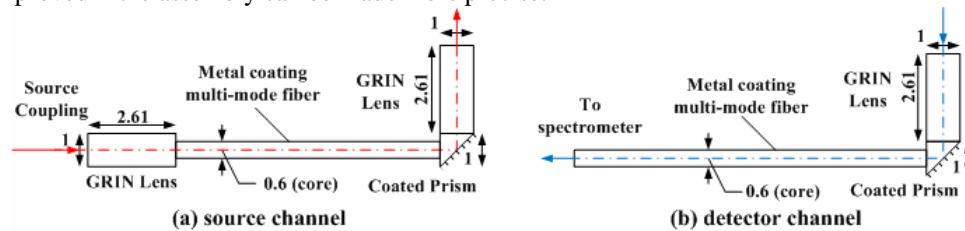


Fig. 2. Micro-optical configurations: (a) source channel; (b) detector channel. Unit: mm

Table 1. Measured coupling efficiency of the source/detector fiber channels

Source channels	s1	s2	s3	s4	s5	s6	s7
Coupling efficiency	46%	48%	49%	49%	51%	43%	49%
Detector channels	d1	d2	d3	d4	d5	d6	d7
Coupling efficiency	54%	48%	49%	51%	53%	52%	50%

## 2.2 Development of a continuous-wave NIR imager for coupling with US

The combined trans-rectal NIR/US imager is schematically illustrated in Fig. 3(a) and the photograph is given in Fig. 3(b). The US scanner is an ALOKA SSD-900V portable machine. The US images are transferred to the main computer of the combined imager by a PCI image acquisition card (National Instruments PCI-1405). The NIR imager uses a custom-designed superluminescent diode (SLD) (Superlumdiodes Inc.) that is pigtailed to a multi-mode fiber

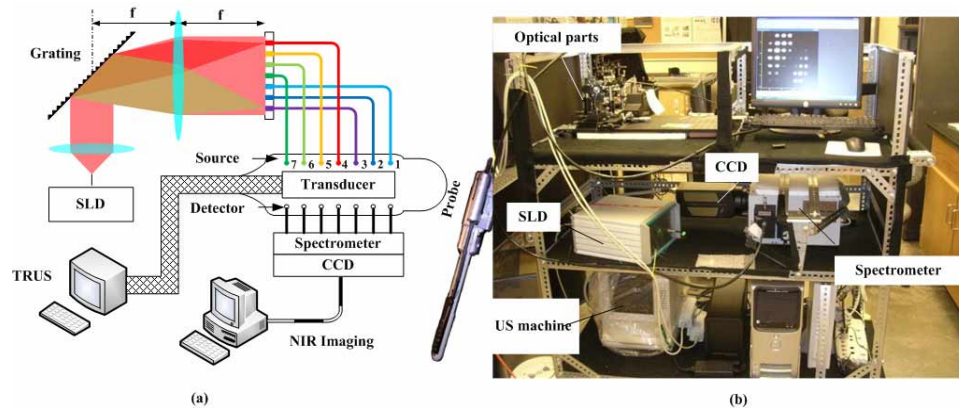


Fig. 3. The combined trans-rectal NIR/US system: (a) System diagram; (b) Photo of the system on a custom designed three-layer cart.

and delivers 100mW of 840nm NIR light with 14.2nm FWHM bandwidth. The SLD output beam is dispersed by a 1200 groves/mm grating and collimated unto linearly aligned 7 fibers connecting to the source channels on NIR applicator. NIR light with slightly different wavelengths are coupled to the 7 fibers to form a spread-spectral-encoding of the source channels [27]. The remitted lights collected by the 7 detection channels are coupled to a spectrometer (Acton Research). The signal corresponding to the individual source channels are discriminated horizontally by the spectrometer. The signals corresponding to the individual detector channels are differentiated vertically based on the position of the detection channels on the spectrometer entrance slit. A 16-bit intensified CCD camera (Princeton Instruments) acquires a complete set of NIR imaging data. The exposure time for one frame of data is in the range of 100s milliseconds, depending on the medium being imaged. The NIR system resides on a custom-built cart that also houses the US scanner.

The CCD has a maximum dynamic range of 48dB, which may not be sufficient to accommodate the full dynamic range of the signals when a medium is highly absorptive, as the minimum and maximum source-detector distances of the trans-rectal NIR array are 20mm and 63mm, respectively. Fortunately, the layout of the dual-line NIR array leads to lesser signal dynamic range for the light illuminated from the sources at the middle portion of the array than the ones at the edges of the array. Reducing the total dynamic range of the signal is possible by proper use of the Gaussian spectrum of the SLD source. The actual light coupling configuration is given in Fig. 4(a), where the stronger spectral components are coupled to the peripheral NIR channels (such as 1 and 7), and the weaker spectral components are coupled to the middle NIR channels (such as 3-5). Comparing with the configuration of coupling the uniform light to all 7 source channels, the strategy in Fig. 4(a) offers a 15dB reduction of the overall signal dynamic range for a medium of  $0.0023\text{mm}^{-1}$  absorption coefficient and  $1.0\text{mm}^{-1}$  reduced scattering coefficient (equivalent to a 1% Intralipid solution).

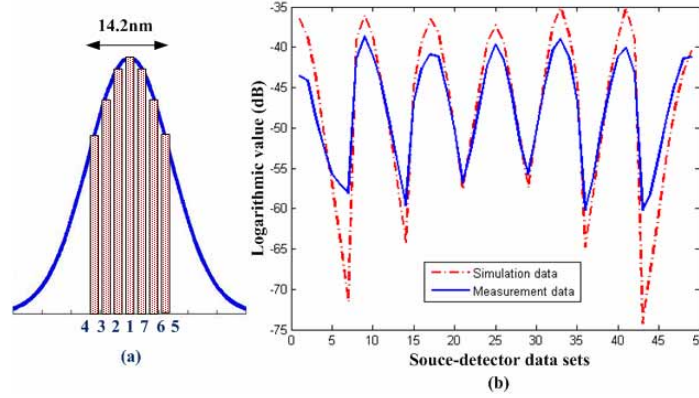


Fig. 4. Source coupling sequence with the Gaussian-spectrum (a), and the received signal dynamic range compared with the case when source channels have even intensities (b).

### 3. NIR image reconstruction based on continuous-wave data

The steady-state diffusion equation for a photon density  $U$  at position  $\vec{r}$  can be stated as [28]

$$\nabla \cdot D(\vec{r}) \nabla U(\vec{r}) - \mu_a(\vec{r}) \cdot U(\vec{r}) = -S(\vec{r}) \quad (1)$$

where  $\mu_a$  is the absorption coefficient,  $D = [3(\mu_a + \mu'_s)]^{-1}$  is the diffusion coefficient with  $\mu'_s$  being the reduced scattering coefficient, and  $S$  is a source term. For a collimated source and a detector at a semi-infinite boundary, the diffuse reflectance may be described by [29]

$$U(\rho) = \frac{S}{4\pi D \rho^2} \left[ -4 \left( \mu_a / D \right)^{1/2} \left( z_b^2 + z_b / \mu'_s \right) \right] \cdot \exp \left[ - \left( \mu_a / D \right)^{1/2} \rho \right] \quad (2)$$

where  $\rho$  is the source-detector distance, and  $z_b$  is a length term determined by the refractive index mismatch on the boundary [30, 31].

The raw data acquired by CCD is shown in Fig. 5(a). If the SLD spectral components were coupled orderly to the source channels from 1 to 7, the higher intensity signals would have been located along a diagonal line in the CCD acquired image [27, 32]. The modified source coupling configuration described in Fig. 4 leads to the pattern of diagonal-shifted high-intensity signals as shown in Fig. 5(a).

The signal non-uniformity among all source-detector pairs is calibrated using the 1% bulk Intralipid solution based on the linear relationship between  $\ln[\rho^2 U(\rho)]$  and  $\rho$  derived from Eq. (2), as shown in Fig. 5(b). One calibrated data set corresponding to the complete 7×7 source-detector pairs is displayed in (c) in comparison to the non-calibrated one.

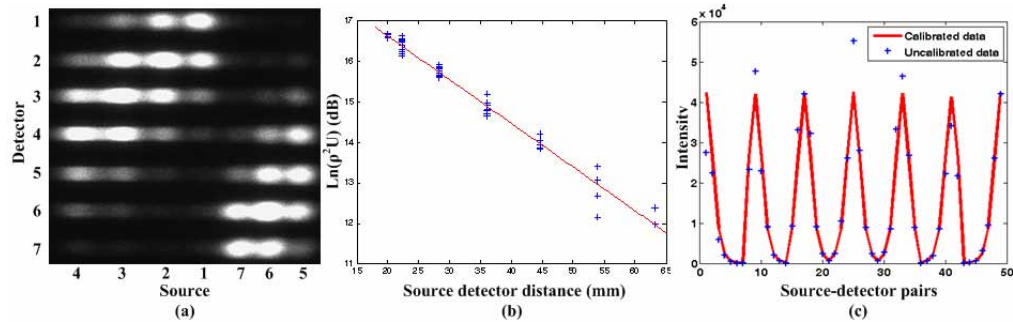


Fig. 5. Data Calibration: (a) raw CCD data; (b) linear fitting of the measurement data based on the semi-infinite model; (c) calibrated data for the signal corresponding to the 49 source-detector pairs.

Recent studies have demonstrated that absorption and reduced scattering coefficients can be reconstructed quantitatively from steady-state measurements, by updating the  $D$  and  $\mu_a$  distributions to minimize a weighted sum of the squared difference between computed and measured data [28]. The method is equivalent to performing the same minimization by mapping the DC signal to frequency-domain [33], which we utilize in the reconstruction.

The frequency-domain diffusion equation [34]

$$\nabla \cdot D(\vec{r}) \nabla U(\vec{r}, \omega) - \left( \mu_a(\vec{r}) + \frac{i\omega}{c} \right) \cdot U(\vec{r}, \omega) = -S(\vec{r}, \omega) \quad (3)$$

where  $\omega$  is the source modulation frequency, is used to map the Equ. (2) using finite-element discretization by setting  $\omega$  to a small value of 0.1Hz. The optical properties are updated by using

$$x_{k+1} = x_k + \alpha \cdot [J^T(x_k)J(x_k) + \lambda I]^{-1} J^T(x_k) \Delta v(x_k) \quad (4)$$

where  $x$  is the parameters to be optimized,  $J$  is the Jacobian derived from Equ. (3),  $\Delta v$  is the forward projection error,  $\lambda$  is a penalty or regularization term. A small damping factor  $\alpha$  in the range of (0, 1) is introduced to stabilize the convergence [1].

Both absorption and reduced scattering coefficients can be reconstructed from the DC measurement, but it is noted that it appears to be generally more difficult for the scattering image to be reconstructed than the absorption image [28]. In this work we focus on recovering targets having absorption contrast to demonstrate the feasibility of TRUS-coupled endo-rectal NIR optical tomography.

The geometry used for image reconstruction is illustrated in Fig. 6. The NIR image reconstruction uses a 3-dimensional mesh representing  $80 \times 40 \times 60 \text{ mm}^3$ . The TRUS sagittal imaging is performed at the mid-plane of the NIR mesh. The TRUS image is used to develop a mesh with target spatial information. The NIR image is reconstructed in 3-dimension, and displayed at the mid-sagittal plane to correlate with TRUS image. The image reconstruction typically takes ~10 minutes on a 3.0GHz Pentium(R) 4 PC for 10 iterations.

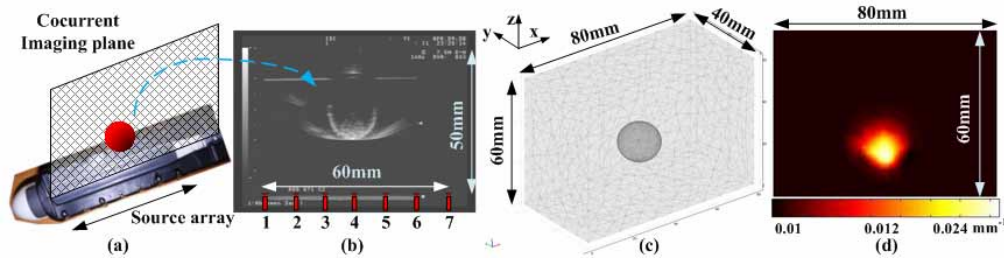


Fig. 6. NIR Imaging geometry: (a) NIR arrays are parallel and symmetric to the TRUS sagittal plane; (b) the positions of NIR channels with respect to the TRUS image; (c) mesh for NIR image reconstruction generated by use of TRUS image; (d) absorption image reconstructed from a simulation data for an absorbing target.

#### 4. Performance evaluation for the TRUS-coupled trans-rectal NIR tomography

##### 4.1 Imaging single target

The performance of phantom imaging by the endo-rectal NIR applicator was evaluated without the use of TRUS *prior*. A 1% bulk Intralipid solution was the background medium. A cylinder-shape solid phantom 15mm in diameter and 25mm long (Fig. 7(a)) was the target. The solid phantom was fabricated from a bulk material that was provided and calibrated by the NIR imaging laboratory of Dartmouth College. The solid phantom has an absorption



coefficient of  $0.0056\text{mm}^{-1}$  and a reduced scattering coefficient of  $1.03\text{mm}^{-1}$ , in comparison to  $0.0023\text{mm}^{-1}$  and  $1.0\text{mm}^{-1}$  of the background. The testing setup is depicted in Fig. 7(b).

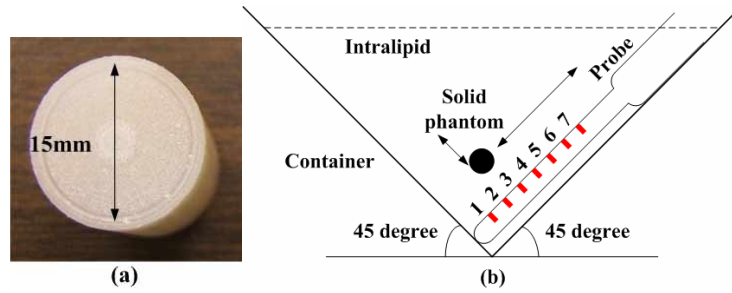


Fig. 7. Solid tissue phantom (a) and experimental setup (b)

Figure 8 lists the images reconstructed without the TRUS *prior* by using a mesh of homogenous density throughout the entire NIR imaging volume. When this mesh is used for reconstruction based on only the NIR information, the optical properties are certainly updated element-by-element in order to recover the heterogeneity being imaged. The solid phantom is placed at the mid-sagittal plane. The NIR images are displayed with a FOV of  $80 \times 30\text{mm}^2$ . The left most optode is located at 10mm right to the left edge of the image, and the right-most optode is 10mm left to the right edge of the image. The (a), (b), and (c) correspond to the target depth of 17.5mm at longitudinal locations of 20, 40 and 60mm (counted from left edge), respectively. The (d), (e) and (f) correspond to the phantom depth of 12.5mm at longitudinal locations of 20, 40 and 60mm, respectively. The target is identified clearly against satisfactorily recovered background; however, the absorption contrast of the target is significantly underestimated.

The same data sets were reconstructed using the target spatial information obtained from TRUS. The TRUS image, similar to the one in Fig. 6(b), has artifacts around and shows only the lower half of the cylinder owing to the shadow effect. This image/artifact pattern is specific to the solid cylinder target that reflects much of the US signal on its surface. This type of artifact may not be representative for tissue imaging *in situ*. The artifact is thereby ignored when incorporating the spatial information of the target, by generating a mesh having a homogenous background region and a circular target region as shown in Fig. 6(c). As there are only two regions to reconstruct, the hierarchical iteration routine introduced in [1] involves only 2-steps. The results are given in Table 2 and Figure 9. The absorption coefficient of the background medium is reconstructed at  $0.002\text{mm}^{-1}$  for all images. The absorption coefficient of the target is recovered to within 14% of the true value.

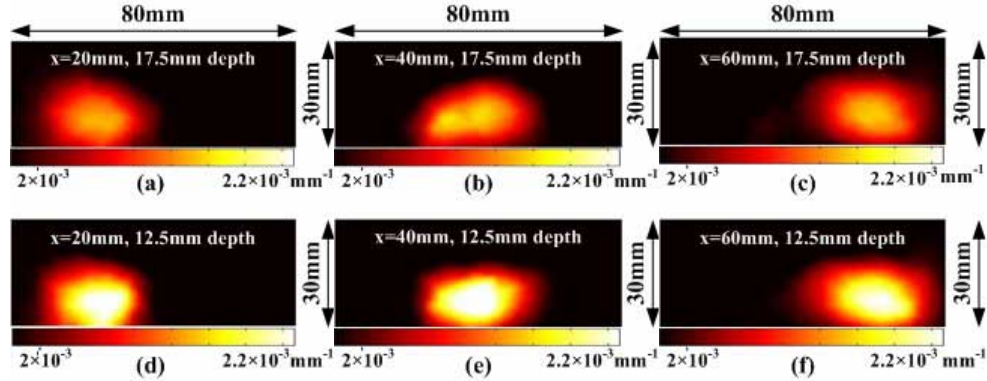


Fig. 8. NIR imaging of a solid tissue phantom having an absorption coefficient of  $0.0056\text{mm}^{-1}$ . The reconstructed background absorption coefficients are  $0.0019\text{mm}^{-1}$  in (a), (b), (d), (e), and  $0.0020\text{mm}^{-1}$  in (c), (f).

Table 2. NIR image reconstruction guided by TRUS- *prior*

Center depth	12.5mm		
Longitudinal location (x)	20mm	40mm	60mm
True Value ( $\text{mm}^{-1}$ )	0.0056	0.0056	0.0056
Reconstructed value ( $\text{mm}^{-1}$ )	0.0067	0.0064	0.0063
Center depth	17.5mm		
Longitudinal location (x)	20mm	20mm	20mm
True Value ( $\text{mm}^{-1}$ )	0.0056	0.0056	0.0056
Reconstructed value ( $\text{mm}^{-1}$ )	0.0064	0.0063	0.0061

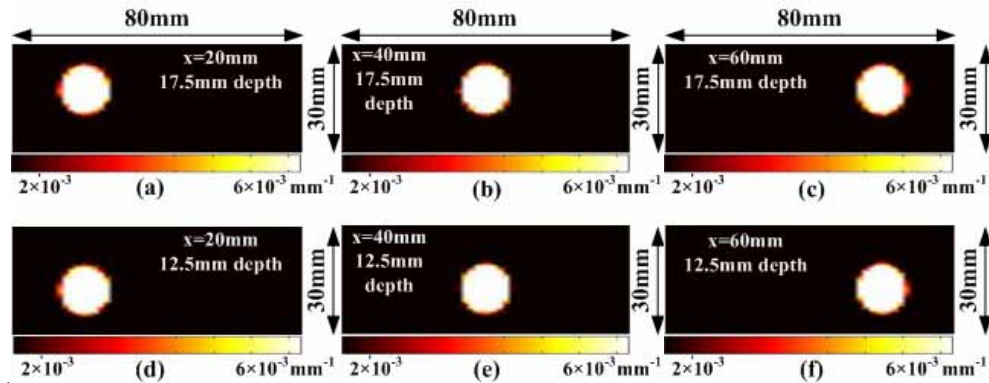


Fig. 9. TRUS guided NIR image reconstruction for solid phantom in homogenous medium

#### 4.2 Imaging two targets

The capability of recovering more than one target by the endo-rectal NIR probe is also examined. Two cylinder-shaped solid tissue phantoms, including the one shown in Fig. 7(a), are used as the target. Both targets are 15mm in diameter and 25mm in length. The newly added solid phantom has an absorption coefficient of  $0.0064\text{mm}^{-1}$  and a reduced scattering coefficient of  $0.997\text{mm}^{-1}$  in comparison to the other one of  $0.0056\text{mm}^{-1}$  and  $1.03\text{mm}^{-1}$ . Figure 10(a) and (b) are the images for placing the two targets at depths of 17.5mm and 22.5mm, respectively, in the mid-sagittal plane, with 20mm longitudinal spacing. When the reconstruction is performed without the target spatial information, the two targets can barely be differentiated at the depth of 17.5mm, and not discriminated at the depth of 22.5mm. The

absorption contrasts of the targets are also significantly underestimated in both cases. Figure 10(c) indicates the results of using the spatial information from the TRUS image. The two targets can be recovered as having different absorption contrasts, at both depths. The reconstructed absorption coefficients listed in Table 3 are also close to the true values.

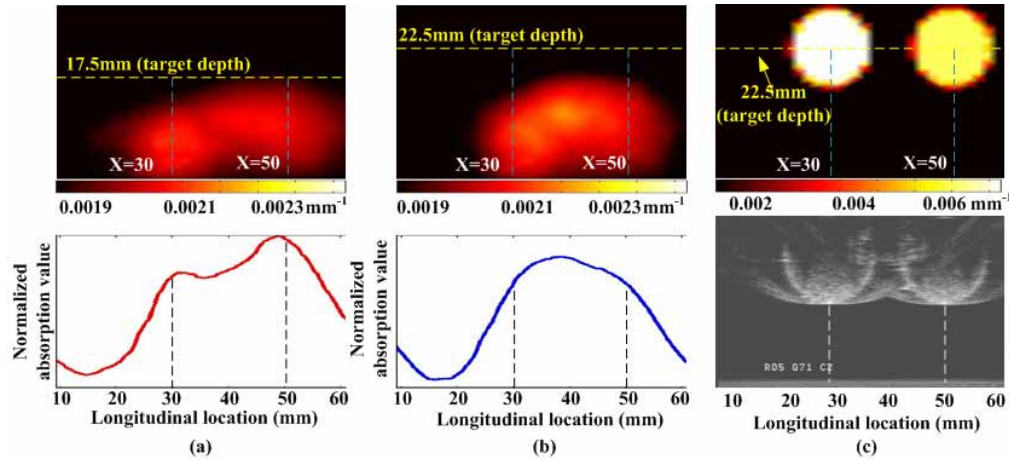


Fig. 10. Imaging of multiple targets: (a) NIR-only reconstruction when the target depth is 17.5mm, the targets can be barely separated; (b) NIR-only reconstruction when the target depth is 22.5mm, the targets cannot be separated; (c) region based reconstruction when the target depth is 22.5mm.

Table 3. Reconstructed absorption coefficients of the two targets in Fig. 12

	Target 1	Target 2
True value ( $\text{mm}^{-1}$ )	0.0064	0.0056
Reconstructed value ( $\text{mm}^{-1}$ )	0.0067	0.0058

#### 4.3 Effects of condom on NIR tomography

The TRUS probe is always covered with a regular latex condom when imaging the prostate. A TRUS-coupled NIR applicator has to be applied with a condom if used in the clinic. In the previous applications of NIR tomography imaging there was no need of applying a latex barrier between an NIR applicator and the tissue being interrogated, therefore the effect of a latex condom on NIR tomography was not reported.

The test being carried out used the setup and solid phantom shown in Fig. 7, by applying US gel to the NIR/US probe, covering the NIR/US with a condom, then pressing the condom to eliminate any gas between the condom and the probe. US gel is not applied on top of the condom when imaging the Intralipid, but is applied for all the tissue imaging tests presented in Section 5. The absorption coefficient of the target reconstructed using TRUS information is listed in Table 4. The overall distribution of the reconstructed absorption coefficient of the target is plotted in Fig. 11(a), and the distribution specific to target position is plotted in Fig. 11(b). These results, which are consistent with those presented in Section 4.1, demonstrate that the condom has minimum effect on NIR imaging. Nevertheless, an attention of the light power is observed, as it takes 10% longer exposure time for CCD to integrate the same amount of signal when the condom is applied.



Table 4. Absorption coefficient reconstructed with the use of condom on the NIR probe ( $\text{mm}^{-1}$ )

Depth (mm)	22.5	25	27.5	30	32.5	35	37.5
True value	0.0056	0.0056	0.0056	0.0056	0.0056	0.0056	0.0056
X=20mm	0.0065	0.0058	0.0070	0.0066	0.0048	0.0043	0.014
X=40mm	0.0053	0.0051	0.0047	0.0049	0.0043	0.0052	0.0063
X=60mm	0.0059	0.0045	0.0066	0.0052	0.0054	0.0095	0.0065

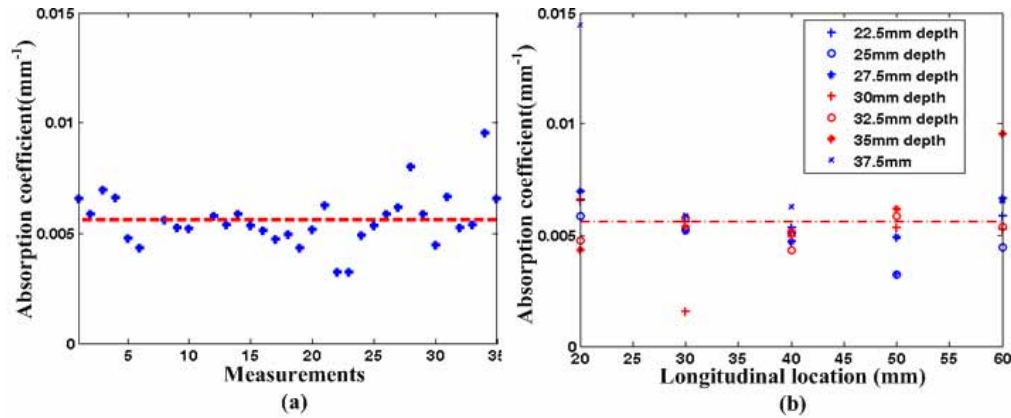


Fig. 11. Test of condom effect on the NIR imaging: (a) reconstructed absorption coefficients for all cases listed in Table 4, and The red dashed line shows the true value; (b) data points in (a) specific to target depths and longitudinal locations.

## 5. Results of tissue imaging by TRUS-coupled trans-rectal NIR tomography

### 5.1 Imaging solid absorbing object embedded in avian tissue

The condom-covered NIR/US probe was enclosed within thick layers of chicken breast tissue ( $\mu_a = 0.006\text{mm}^{-1}$ ,  $\mu'_s = 0.757\text{mm}^{-1}$  [35]), and a black object (10mm diameter  $\times$  10mm length) was embedded as the target. The photographs in Fig. 12(a) and (b) show the setup of tissue sample and the absorbing target being embedded. The tissue without the absorbing target is also imaged as a baseline test. The baseline images by US and NIR are shown in Fig. 12(c), where the NIR image is reconstructed using a homogenous mesh as there was no indication of a target on US. Figure 12(d) to (f) correspond to target being embedded at different longitudinal locations at slightly different depths. The embedded object is clearly visible in the US images as anechoic shadows. The NIR imaging without prior information can clearly recover the object, but with inconsistent and potentially much under-estimated absorption coefficients. When the target location and size information are used to guide the NIR image reconstruction, the target is recovered with consistent absorption coefficients indicating a strongly absorbing object.

### 5.2 Internal imaging of avian tissues

As shown in Fig. 13(a) the empty abdomen of a whole chicken was filled with chicken breast tissue and a piece of chicken liver was embedded within the breast tissue. The embedded liver shows up as the hypo-echoic region circled in Fig. 13(b). The NIR image reconstructed without any target information is given in Fig. 13(c), in which the absorptive mass does correlate longitudinally with the liver tissue. Fig. 13(d) shows NIR image reconstructed by treating the liver mass as a sphere. Fig. 13(e) shows the NIR image reconstructed by excluding the non-tissue region from the background of Fig. 13(b). Fig. 13(f) shows the NIR

image reconstructed by taking into account the irregular shape of the liver mass. Among the 3 spatial *prior* implementations, the one in Fig. 13(f) is the most accurate wherein the absorption coefficient of the chicken liver mass is also the closest to the realistic value [35].

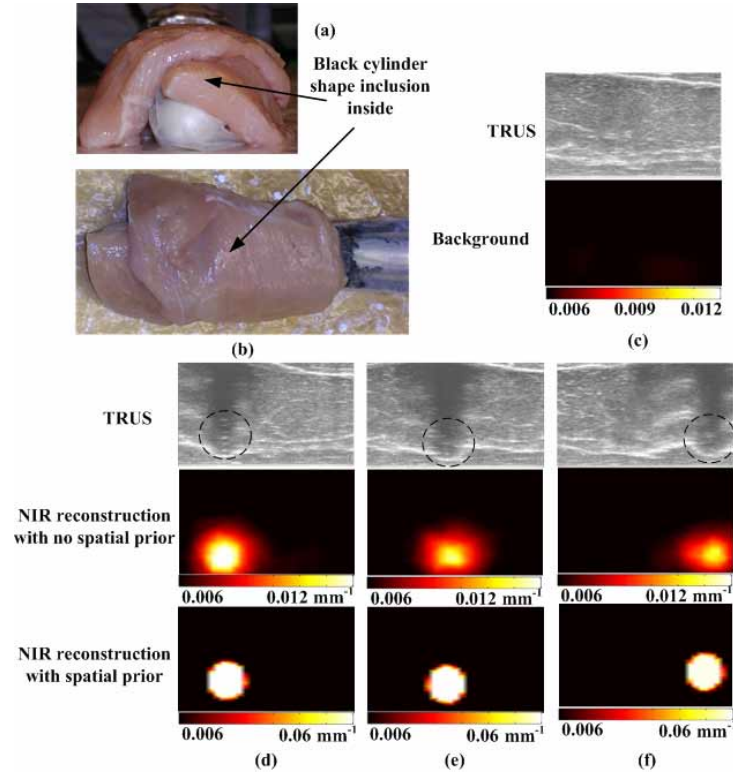


Fig. 12. Avian tissue imaging: (a) front view; (b) top view; (c) no inclusion; (d) inclusion is at 20mm; (e) 35mm; (f) 58mm, longitudinally, respectively.

### 5.3 TRUS-coupled trans-rectal optical tomography of canine prostate *in situ*

TRUS-coupled trans-rectal NIR imaging of the prostate is conducted on a canine cadaver. The prostate was exposed and approximately 0.33ml of homogenized foal liver was injected ventral-dorsally, paramedian in the left lobe of the prostate. The prostate was then enclosed in thick layers of peri-prostate tissues. On the TRUS image of Fig. 14(a) the injected liver tissue is visible by the mass proximal to the center of the prostate and the vertical hyper-echoic strip at the ventral side of the prostate. The large hypo-echoic region at the upper half was due to air. The mesh generated in Fig. 14(b) has excluded the air based on the US image. The rectum wall was not outlined in the mesh because of its close proximity and near apposition to the US transducer due to the small size of this canine cadaver. The rectum layer may be included when imaging a larger subject. The finalized mesh given in Fig. 14(b) shows nested-domains where there is a relatively small prostate and a much smaller target in the prostate. The NIR image in Fig. 14(c) is reconstructed by applying the 3-step hierarchical reconstruction method introduced in the previous paper [1]. A highly absorptive mass is clearly recovered out of the injected liver tissue. The absorption coefficient of the foal liver tissue in Fig. 14(c) is lower than that of the avian liver tissue in Fig. 13(f); nevertheless both values are at the order of  $0.1\text{mm}^{-1}$ , indicating high absorption by both tissues. The reconstructed absorption coefficients of the prostate and the peripheral tissue are given in Table 5. It is very interesting to observe that the numbers agree with the values suggested by the literature [16-18, 35].

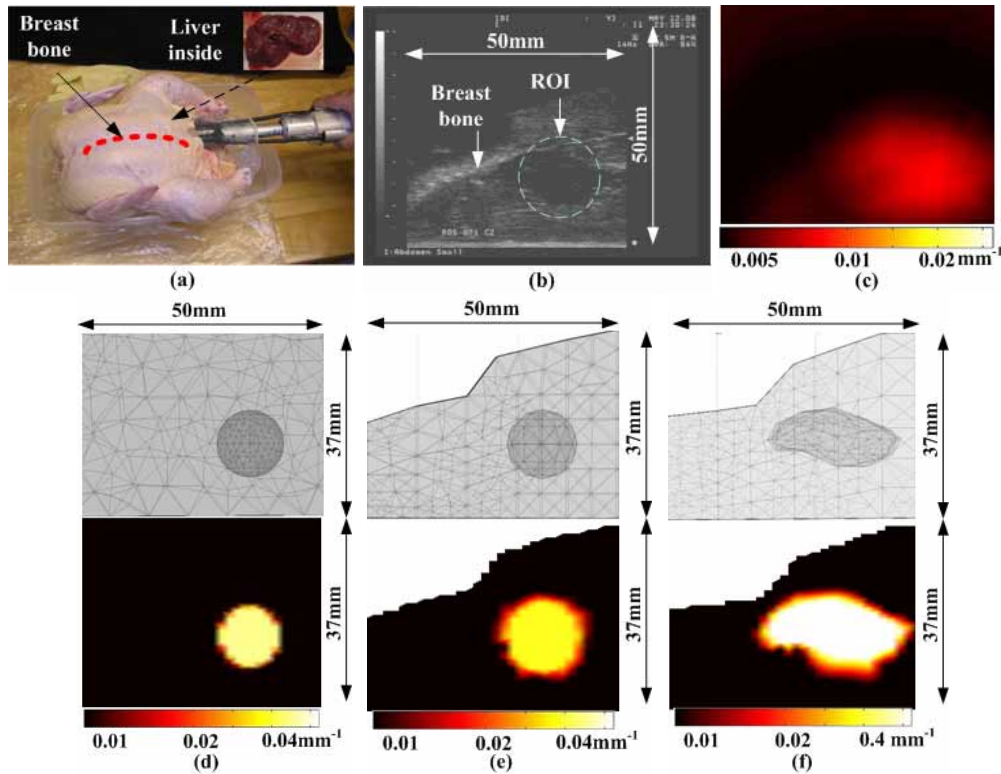


Fig. 13. Internal imaging of avian tissue embedded with a piece of liver. (a) Whole chicken sample; (b) US image of the embedded liver tissue; (c) NIR image reconstructed without US *prior*; (d) NIR image reconstructed assuming a circular target; (e) NIR image reconstructed by adding the boundary profile of the background tissue; (f) NIR image reconstructed by adding the actual contour of the target.

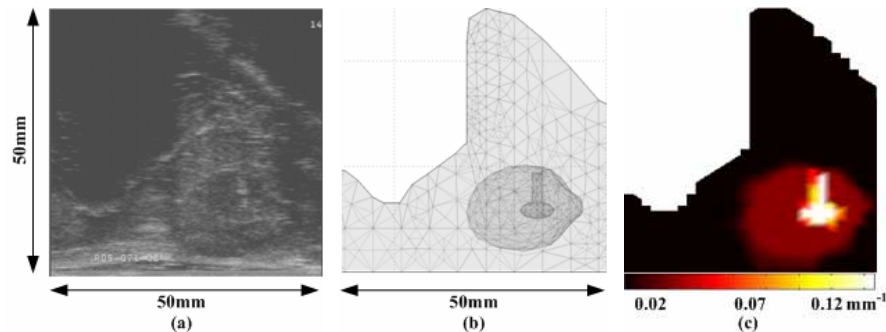


Fig.14. Trans-rectal NIR / US imaging of in vitro canine prostate with exogenous tissue contrast.

Table 5 Reconstructed absorption value of in vitro canine prostate imaging

Region	Background	Prostate	Injected liver
Reconstructed value ( $\text{mm}^{-1}$ )	0.0062	0.0309	0.1301

## 6. Discussion

In the NIR imager an 840nm superluminescent diode with ~14nm bandwidth is used to simultaneously excite all source channels. The bandwidth would certainly introduce

wavelength-dependent attenuation among source channels for the same tissue chromophore. The reconstructed absorption coefficient is therefore a value averaged over the band coupled into the source channels. Luckily the absorption of the tissue chromophores like hemoglobin is less wavelength-dependent in the close vicinity of 840nm. If the source coupling method is performed at an additional wavelength, such as 780nm, to quantify the oxygen saturation [36], it may be necessary to compensate the wavelength-dependent absorptions among source channels in image reconstruction.

It is shown that the absorption coefficient can be quantitatively reconstructed by steady-state trans-rectal NIR measurements. The accuracy of reconstruction for a highly heterogeneous domain can be improved dramatically by use of the TRUS spatial *prior*. Implementing frequency-domain detection to the NIR system will also allow more accurate reconstruction of the absorption coefficient owing to the reliable differentiation of it from the scattering by true phase information.

Generating the target mesh from the TRUS image has been based on the assumption that the entire imaging volume and the target are symmetric and centered at the TRUS imaging plane. This is perhaps necessary if only one TRUS image is utilized to form a 3-dimensional mesh for NIR image reconstruction, but is mostly inaccurate. This is particularly problematic in imaging of the prostate if the NIR/US probe is to be directed away from the midline of the prostate. The effect of asymmetric-domain may be corrected if multiple US images are available to generate a mesh representing the true 3-dimensional contents of the imaging volume more faithfully.

The trans-rectal examination of the prostate on the sagittal view is likely being interfered with by the nearby bladder and pelvic bone. If the bladder is empty, the photon propagation may be less interrupted. If the bladder is full, it may become a relatively transparent domain for photon propagation. In this case the bladder likely becomes a diffusion-void domain [37, 38]. A transport-equation based model of photon propagation can be implemented [37, 39] to mitigate the interference of void-domains. The interference from the pelvic bone is similar in principle to that of the chest wall in breast imaging when using a planar NIR array [40]. In this work we applied the Robin-type boundary condition under diffusion equation to the void-tissue interfaces under the diffusion model. This is a rather straightforward approach that is proven helpful for improving the reconstruction accuracy, but more studies are needed to quantitatively evaluate improvement by this approach in comparison to the more rigorous transport-based model.

The probe sensitivity curves in this paper and those in the previous paper [1] were all derived under the assumption of an absorptive NIR probe surface. This boundary condition produces a peak of depth-sensitivity close to, but not at, the probe surface. This feature may be desirable for prostate imaging, since the measurement will be less sensitive to the existence of a rectum layer. On the other hand, the peak also indicates that the measurement is less sensitive to a lesion deeper in the prostate than one closer to the surface of the prostate. Prostate tumors are known to occur more often in the peripheral zone which stretches abaxial from the middle-line of the prostate. For deeper target, we have showed that with TRUS *prior*, the accuracy of target recovery can be improved successfully. However, more dedicated simulation and experimental studies are necessary to evaluate the likelihood of retrieving deeper target *in vivo*.

In all the tests presented in this work, the target of interest is visible or at least sensitive to US, therefore US spatial information of the target is readily rendered to guide the NIR image reconstruction. If the target is ambiguous to US, it may still be recognizable by NIR-only reconstruction. One example is given in Fig. 15 wherein a piece of chicken breast tissue was dyed with diluted Indian ink and then placed in the middle of the natural chicken breast tissue. The approximate boundary of the dyed tissue is marked with the dash-circle in the US image. This embedded tissue is hardly distinguishable in the TRUS image; therefore the NIR image reconstruction was performed without any *a priori* information. The target is identified by

NIR even though the depth and size were not accurate. This result may show positive indication on the clinical application of trans-rectal NIR/US measurement providing the fact that up to 40% of prostate tumors are not sensitive to US [3, 6, 7]. Besides using NIR information to characterize US-sensitive lesions, if the NIR imaging is able to discover a lesion that is otherwise non-suspicious on US, the overall sensitivity and specificity of TRUS-based prostate imaging may be improved.

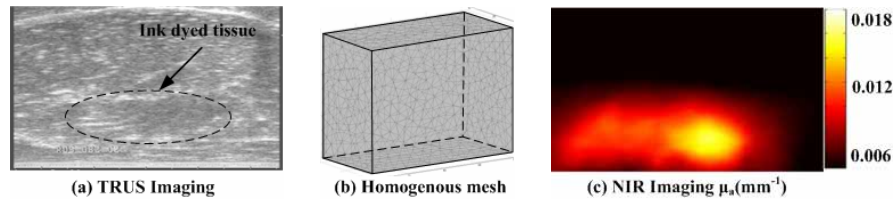


Fig. 15. Imaging of a tissue mass that is ambiguous to TRUS but sensitive to NIR.

## 7. Conclusions

We implemented the NIR array design suggested in our previous work for direct integration of the NIR array with a TRUS transducer. The combined NIR/US probe & system enabled concurrent acquisition of trans-rectal NIR tomography and TRUS images in the same sagittal plane. Although the NIR imager is constructed in CW mode, accurate quantitative reconstruction of the absorption coefficient is feasible with the TRUS spatial *a priori* information. The use of a condom is found to have minimum affect on NIR tomography measurement, indicating that endo-rectal NIR may be applied concurrently with TRUS in a clinic setting with no alteration of the standard procedures. An absorptive target may also be recovered by trans-rectal NIR only, but the incorporation of TRUS *a priori* information allows trans-rectal NIR tomography to recover an absorption target more accurately, as demonstrated by imaging of the alien tissue in the canine prostate. The previous Part-I and this Part-II papers together have validated prostate imaging as feasible by TRUS-coupled trans-rectal NIR tomography. Work is on-going toward *in vivo* measurement of optical properties in intact prostate as well as development of prostate cancer models in the canine to validate that augmenting TRUS morphology information with trans-rectally acquired NIR contrast may improve the overall accuracy of TRUS prostate imaging.

## Acknowledgments

This work has been supported by the Prostate Cancer Research Program of the U.S. Army Medical Research Acquisition Activity (USAMRAA), 820 Chandler Street, Fort Detrick MD, 21702-5014, through grant #W81XWH-07-1-0247. The content of the information does not necessarily reflect the position or the policy of the USARAA, and no official endorsement should be inferred. The authors would like to thank Drs. Brian W. Pogue and Quing Zhu for enlightening discussions and suggestions. Comments and questions may be directed to Daqing Piao whose e-mail address is [daqing.piao@okstate.edu](mailto:daqing.piao@okstate.edu).

# Development of a continuous-wave dual-band trans-rectal optical tomography system for concurrent sagittal imaging with trans-rectal ultrasound

Zhen Jiang, Hao Xie, Daqing Piao, Jerzy S. Krasinski

*School of Electrical and Computer Engineering, Oklahoma State University, Stillwater, OK 74078*

*\*Corresponding author: [daqing.piao@okstate.edu](mailto:daqing.piao@okstate.edu)*

## ABSTRACT

A dual-band trans-rectal optical tomography system is constructed based on an endo-rectal near-infrared/ultrasound applicator that has been developed previously in our laboratory. The endo-rectal NIR/US applicator consists of a commercial bi-plane ultrasound and a NIR probe attached to the sagittal ultrasound transducer. The NIR probe consists of 7 illumination & 7 detection channels that are distributed in parallel to and aside the sagittal TRUS transducer. The emissions from a 780nm and an 830nm light sources are combined and delivered sequentially to the 7 NIR source channels of the endo-rectal NIR/US probe. The 7 NIR detection channels are coupled to a spectrometer for separation of the signals at two wavelengths illuminated from single source channel. The dual-band signals from all source channels are acquired sequentially by a CCD camera synchronized with the source switching. The acquisition of dual-band trans-rectal optical tomography data is accompanied by position-correlated concurrent trans-rectal ultrasound imaging. The reconstruction of a target at dual-wavelength illumination is guided by *a priori* spatial information provided by the sagittal trans-rectal ultrasound. Liquid phantoms with different hemoglobin concentration and oxygen saturation are used to test the feasibility of dual-band trans-rectal optical tomography.

**Keywords:** Near-infrared tomography, oxygen saturation, trans-rectal ultrasound

## 1. INTRODUCTION

The utility of non-invasive imaging of the tissue oxygenation by multi-band near-infrared (NIR) light has been recognized for decades. The distinctly different spectra of hemoglobin absorption of the NIR light when being oxygenated and deoxygenated have enabled finding lesions of angiogenesis or altered oxygenation indicating malignant changes [1-2]. Studies on prostate cancer have found a correlation between the cancer and increased micro-vessel density [3]. Changes of the local oxygen saturation were also observed during the prostate photodynamic therapy under interstitial NIR measurement [4]. Tissue oxygenation status is also an important prognostic indicator for androgen-deprivation therapy of newly diagnosed metastatic prostate cancer [5]. There is increasing evidence that the ability of quantifying the hemoglobin concentration and oxygen saturation in prostate is important for the diagnosis, prognosis, and treatment monitoring.

Encouraged by the applications of multi-band NIR light in breast cancer imaging [6-7], researchers recently start to develop NIR tomography techniques for trans-rectal imaging of the prostate [8-10]. In this work we report the progress on the instrumentation of dual-band trans-rectal NIR imaging. The dual-band trans-rectal NIR tomography is to be combined with trans-rectal ultrasound (TRUS) to take advantage of real-time positioning information and further the anatomic information of US to guide the NIR image reconstruction.

## 2. METHODS AND MATERIALS

A total of three endo-rectal imaging NIR applicators have been historically developed in our laboratory to investigate dual-band trans-rectal NIR tomography that may be coupled with TRUS. The first one was an axial-imaging probe of 13mm in diameter [11]. The second one was an axial-imaging probe of 20mm in diameter [8] which is comparable in



size to the trans-rectal ultrasound transducer. The third probe was for sagittal imaging and could couple directly to a sagittal TRUS transducer for concurrent NIR/US imaging [10].

## 2.1 The 13mm-diameter axial-imaging endo-rectal NIR probe

Figure 1 illustrates the 13mm-diameter axial imaging NIR tomography probe. It consists of 16 optical channels including 8 for sources and 8 for detectors. Those source and detector channels were interlaced evenly on the circle. The diameter of each optical fiber is 600 $\mu$ m. A 10mm-diameter cone lens was used for deflecting the light circumferentially for axial-imaging. The fibers and cone-lens were mounted together in a 13mm diameter black sleeve and sealed with transparent optical epoxy. A total of 16 sealed transparent apertures were made at the axial-plane of the probe for the light-path.

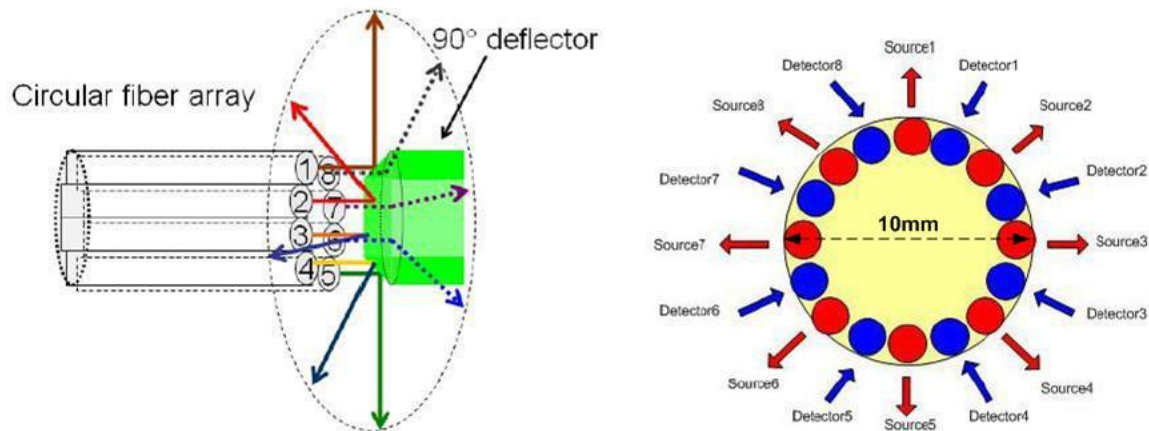


Figure 1. Geometry of the 13mm axial-imaging NIR tomography probe

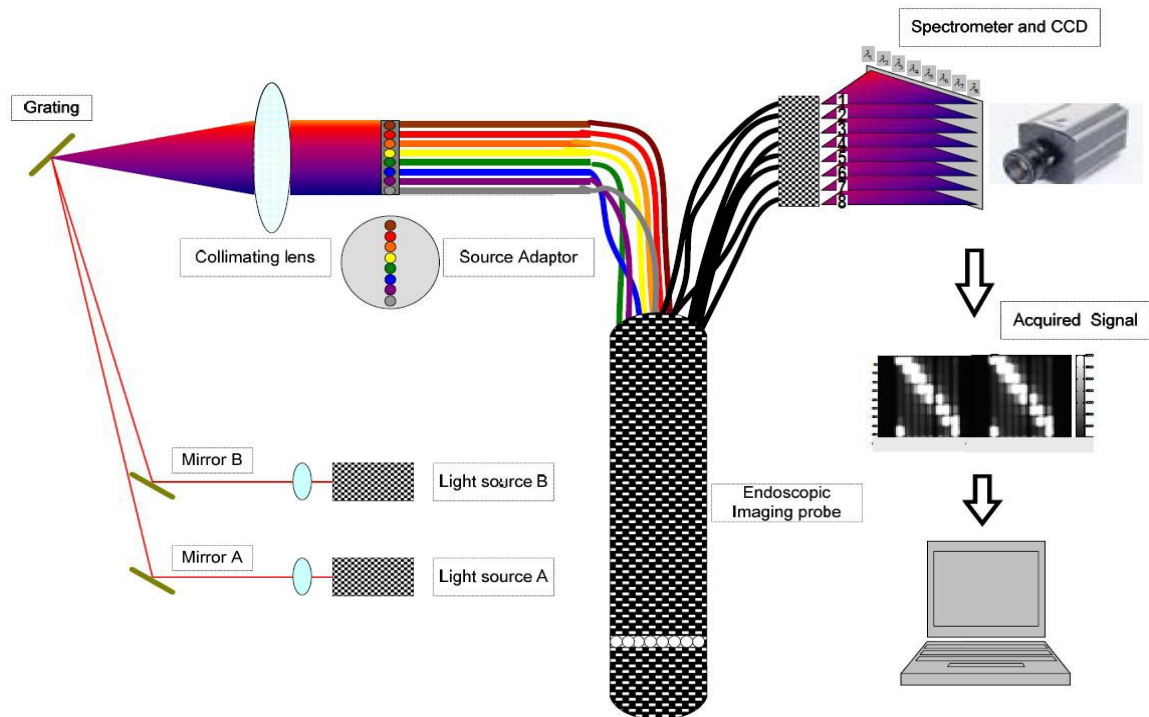


Figure 2. Spread-spectral-encoding based dual-wavelength NIR imaging system

For this probe the dual-wavelength NIR imaging was configured in spread-spectral-encoding mode. Shown in Fig. 2, two broadband (~14nm bandwidth) superluminescent diode (SLD) light sources (780nm and 830nm) pigtailed to single mode fibers were used in the system. Each SLD delivers 14mW of power. The SLD outputs were collimated at



different angles to a 1200 grooves/mm grating and the dispersed beams of both bands overlap. The dual-wavelength dispersed beam was collimated by a planar-convex lens with a focal length of 300mm, and then coupled onto 8 linearly aligned source fibers. Each source channel coupled  $\sim 1.5$ nm bandwidth out of each SLD bands for illumination to the medium, and the dual-band light was collected by detection fibers coupled to a spectrometer where the dual-band signals were differentiated by a 300 grooves/mm grating to two groups, each containing a complete set of measurements for all source and detector channels for each wavelength band. The complete set of the dual-band data, shown in Fig. 3 which was acquired by a 16-bit CCD camera, was calibrated based on photon diffusion equation and underwent image-reconstruction using the NIRFAST algorithm developed by Dartmouth NIR imaging group. The use of photon-diffusion equation for this 13mm probe may not be accurate owing to the smaller size of the probe with respect to the mean scattering distance; however, the reconstructed dual-band images of the hemoglobin and oxygenation were qualitatively correct as a result of likely canceling out of the inaccuracy from both bands.

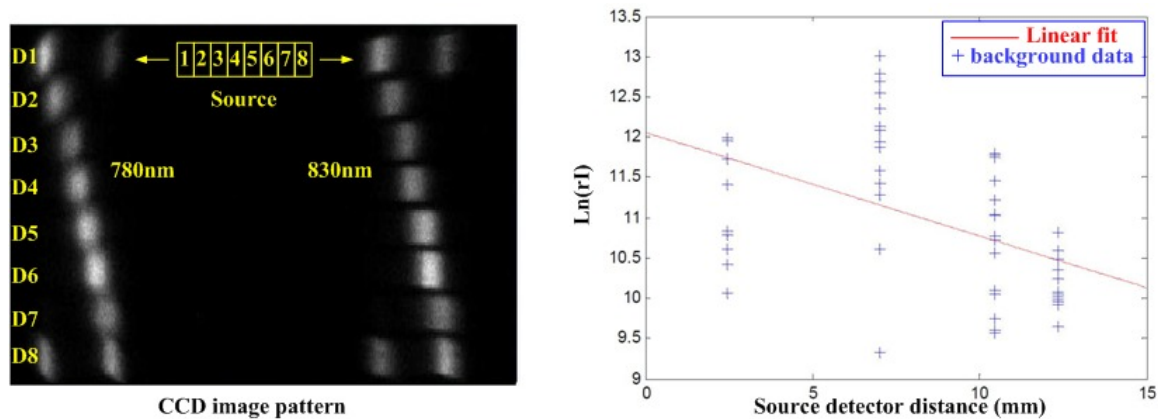


Figure 3. CCD image and raw data of 13mm-probe

## 2.2 The 20mm axial-imaging endo-rectal NIR probe

Figure 4 illustrates the configuration of the 20mm axial-imaging endo-rectal NIR probe. Similar to the previous 13mm-imaging probe, there are 8 source and 8 detector optical channels spaced circularly. Each optical channel was constructed with a 1.0mm core diameter fiber and aligned to a  $45^\circ$  rod lens of 2mm diameter to deflect the beam transversely for side-firing. A 2mm drum lens was attached for illumination and beam focusing. The length of the probe is 7" which was comparable to a standard TRUS probe.

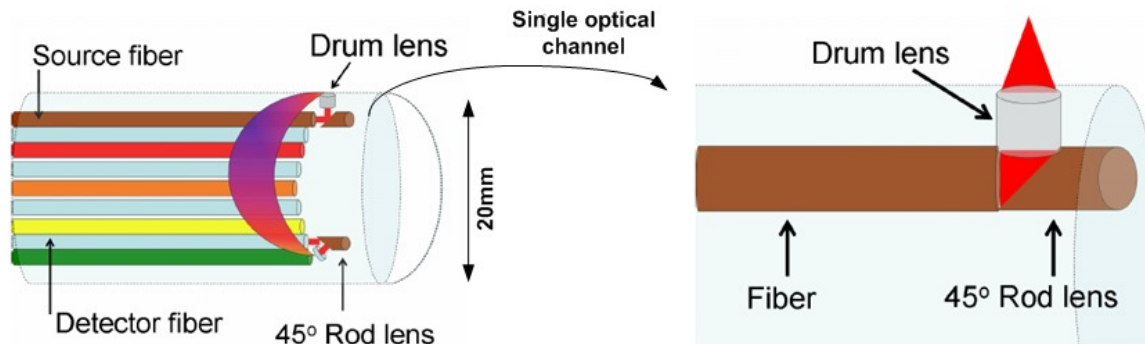


Figure 4. Diagram of 20mm endoscope NIR tomography transverse imaging probe

This 20mm diameter probe was connected to a time-multiplexing light delivery setup for dual-band NIR tomography as shown in Fig. 5. The  $\sim 100$ mW outputs from two laser diodes (LDs) at 785nm and 850nm were coupled by a bifurcated fiber to a fiber switch that was home-made using a linear motorized translation stage (Zaber Technologies). The switching of the light upon 8 source channels was synchronized with the CCD acquisition of the corresponding signals received by all detectors.

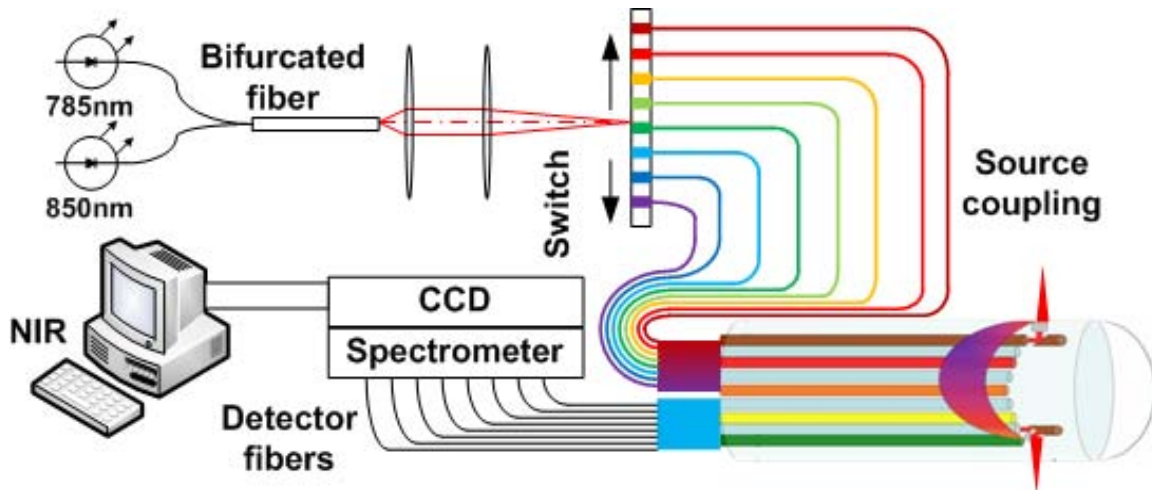


Figure 5. Dual wavelength NIR tomography system for 20mm-probe

Each complete set of the data consists of 8 frames corresponding to each source channel being turned on by the fiber switch. Fig. 6 is the one frame data when the source 3 is switched on. Because of the longer distance between the source and detector, the total 64 data sets follow a better linear fitting curve than the previous data sets for the 13mm probe in Fig. 3. The use of fiber switching also minimized the cross-talk among the adjacent source channels. The weakest signal however may submerge in the background noise owing to the limited dynamic range of the CCD.

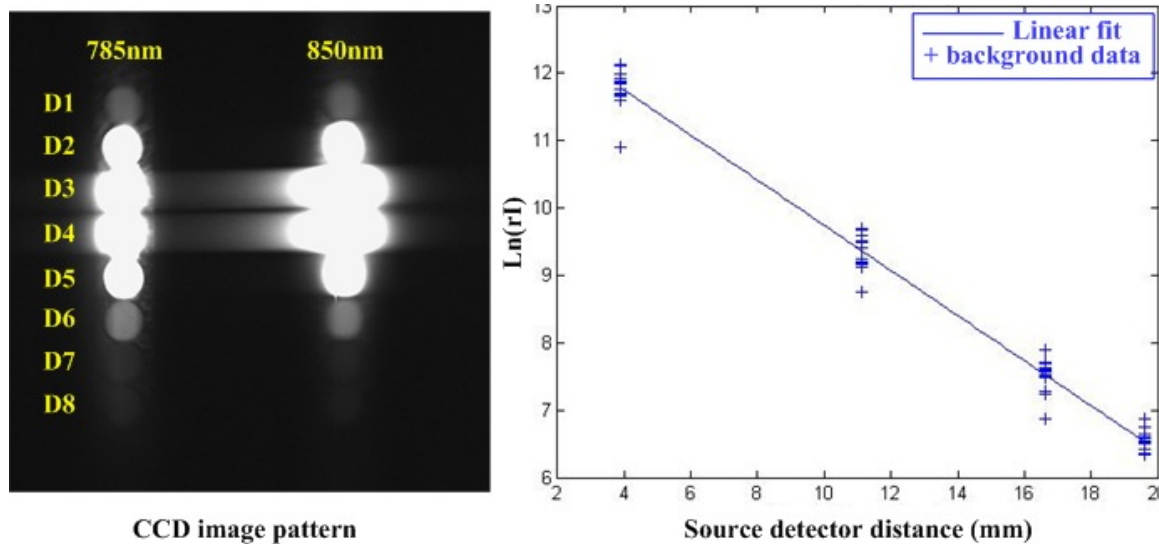


Figure 6. CCD image and raw data of 20mm probe

### 2.3 Combined trans-rectal NIR and ultrasound imaging probe

A sagittal trans-rectal NIR imaging probe was developed for coupling with the TRUS and to improve the imaging depth as in sagittal view the optodes can occupy larger array for deeper interrogation. The integrated sagittal-imaging trans-rectal NIR/US applicator consists of a custom-built NIR probe and a commercial sagittal TRUS transducer operating at 7.5MHz, as shown in Fig. 7. The sagittal TRUS transducer occupies a space of 60mm×10mm. The NIR applicator was fabricated from a black polycarbonate material and built to a cap-shape to attach to the TRUS probe. A slot of 60mm×10mm was opened up in the NIR applicator to expose the sagittal TRUS transducer.

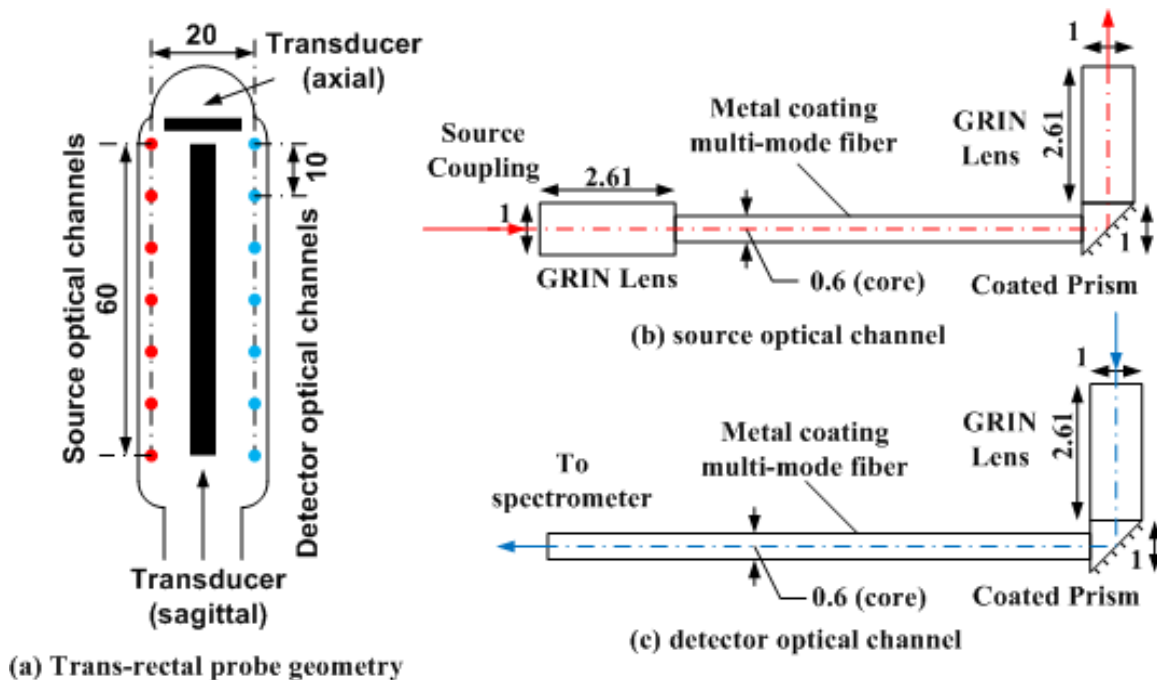


Figure 7. Combined trans-rectal NIR/US imaging probe geometry (unit: mm)

The source array and the detector array, separated 20mm laterally, each has 7 channels spaced at 10mm. A metal-coated 600 $\mu$ m-core diameter fiber (Oxford Electronics) was chosen for each optical channel. As shown in Fig. 7, each source channel includes 2 gradient-index (GRIN) lenses and 1 prism attached to the fiber while each detector channel has 1 GRIN lens and 1 prism attached to the fiber. The GRIN lens (Newport Corporation) has a pitch of 0.25, a diameter of 1mm, a length of 2.61mm, and a numerical aperture of 0.46. The prism is a coated 1mm right angle micro-prism (Tower Optics). Each fiber was polished and epoxied to a prism and a GRIN lens was attached to the other side of the micro-prism for illumination and detection at the probe surface. Each source channel has one GRIN lens attached to the proximal end of the fiber for coupling the emission from the light source.

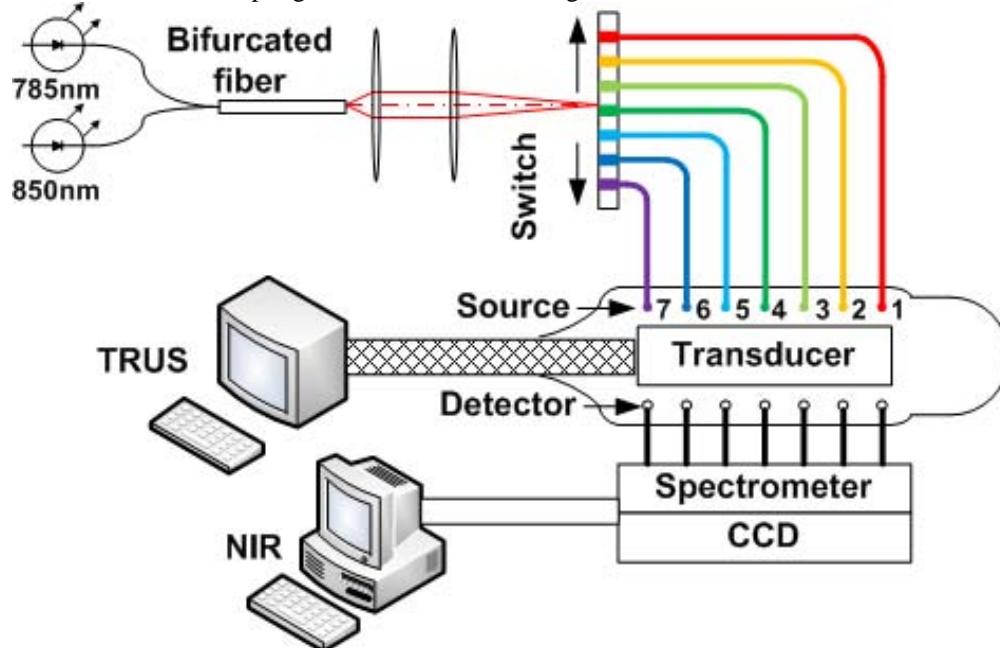


Figure 8. Dual wavelength system setup for combined trans-rectal NIR/US probe

The combined NIR/US system for dual-band trans-rectal mode imaging is shown schematically in Fig. 8. The US scanner was an Aloka SSD-900V portable machine. The US images were transferred to the main computer of the combined imager by a PCI image acquisition card (National Instruments PCI-1405). The source switching is by the time-multiplexing setup described in Fig. 5. This system takes 7 frames to acquire a complete set of data. One example of the single-frame image for the fiber switch being turned to source channel 4 is depicted in Fig. 9. The signals have less dynamic range than do in Fig. 6 because of the configurations of the optodes.

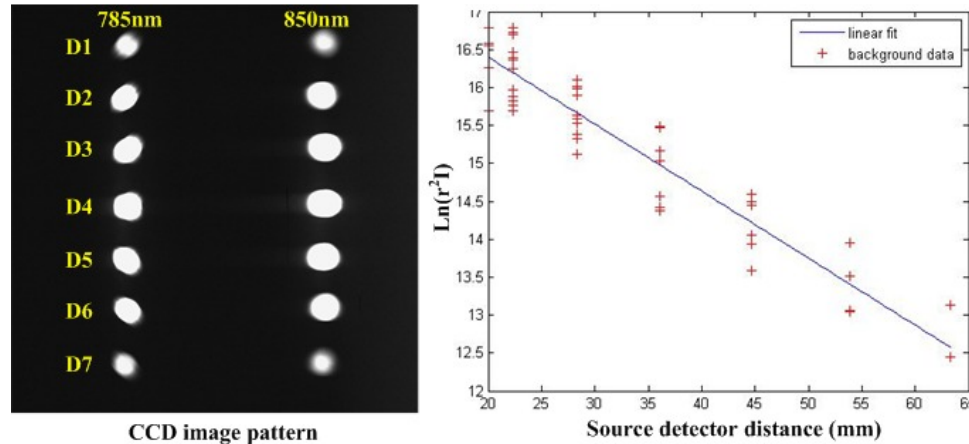


Figure 9. CCD image and raw data for trans-rectal NIR/US imaging probe

#### 2.4 Setup for measurements of hemoglobin concentration and oxygen saturation.

A setup shown in Fig. 10 was built for measuring the blood hemoglobin concentration and oxygen saturation. Oxygen and Nitrogen gases were introduced to the fresh sheep blood (300mL) in a tank to administer the level of blood oxygen saturation ( $\text{StO}_2$ ) which was monitored by an oximeter. A pump delivered the blood from the tank to a cylindrical container placed 2.5mm away from the endo-rectal NIR probe. Test started from the lowest  $\text{StO}_2$  level in the blood and stopped when it became saturated.

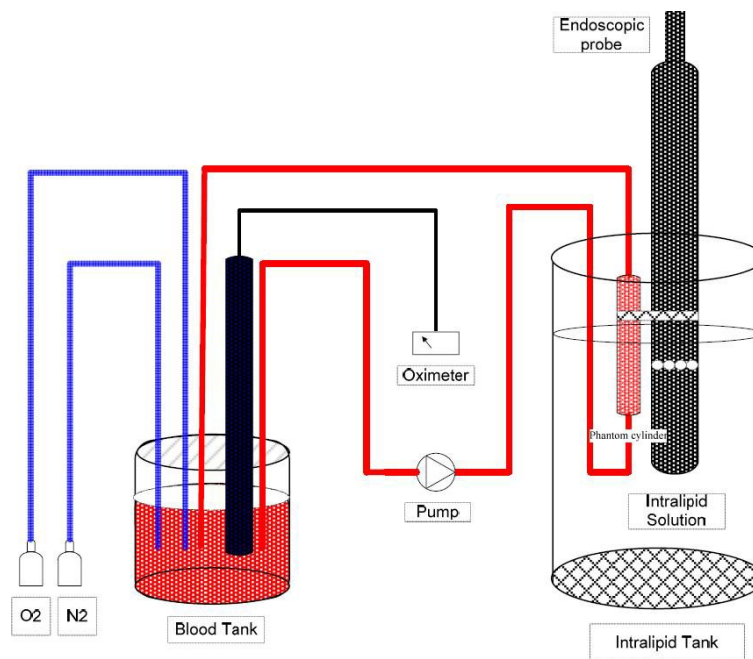


Figure 10. Diagram of blood circulation system for measurements of  $\text{StO}_2$

### 3. PRELIMINARY RESTULS

#### 3.1 Dual-band absorption measurements by the 13mm axial-imaging endo-rectal NIR probe.

Calibration of the system at both wavelengths was carried out using homogenous medium with different concentrations of diluted India ink (concentration 0.005%~0.5%). A container was made into cylinder shape (10mm inner diameter) from a solid phantom ( $0.0056\text{mm}^{-1}$  of absorption and  $1.03\text{mm}^{-1}$  of reduced scattering). The container was fixed close to the probe (2.5mm away from container surface to probe surface) in a 1% intralipid background ( $0.0023\text{mm}^{-1}$  in absorption and  $1.0\text{mm}^{-1}$  in reduced scattering). Another 2ml 1% intralipid was poured into the cylindrical container. The container wall was thinner than 1mm. The total volume of this cylindrical container was 3ml. The change of the absorption of adding one drop (0.02ml) of the diluted ink (0.5%) into the intralipid medium was previously calibrated by use of transmission measurements and Beer's law. One frame data was taken after adding each drop of ink up to 10 drops. The reconstructed absorption of the diluted ink in the container was shown in Fig. 11 where a linear relationship is found comparing with the true values.

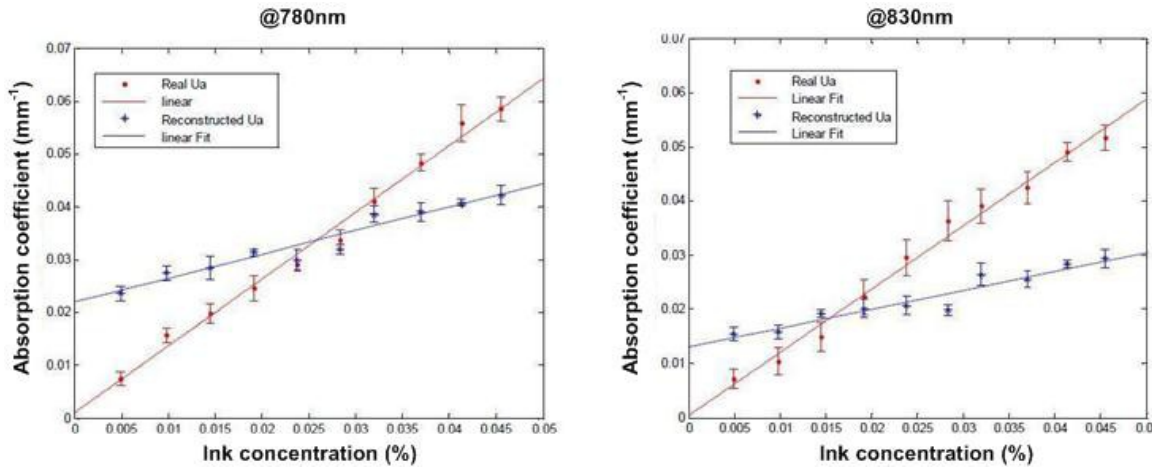


Figure 11. True absorption coefficient and reconstructed absorption coefficient of diluted ink

#### 3.2 Dual-band measurements of blood oxygenation by the 13mm axial-imaging endo-rectal NIR probe.

By using the imaging system configured in Fig. 10 and the calibration results in Fig. 11, the reconstructed absorption coefficients of the sheep blood when the oxygen saturation level changed were illustrated in Fig. 12. Due to the fluctuation of oxygen and nitrogen flowing in the blood and some other aspects including temperature control, leakage of gas from the blood tank, the blood could not be fully oxygenated. However, the tendencies of decreasing and increasing absorption values with respect to the increasing oxygenation at the two wavelength bands were correct.

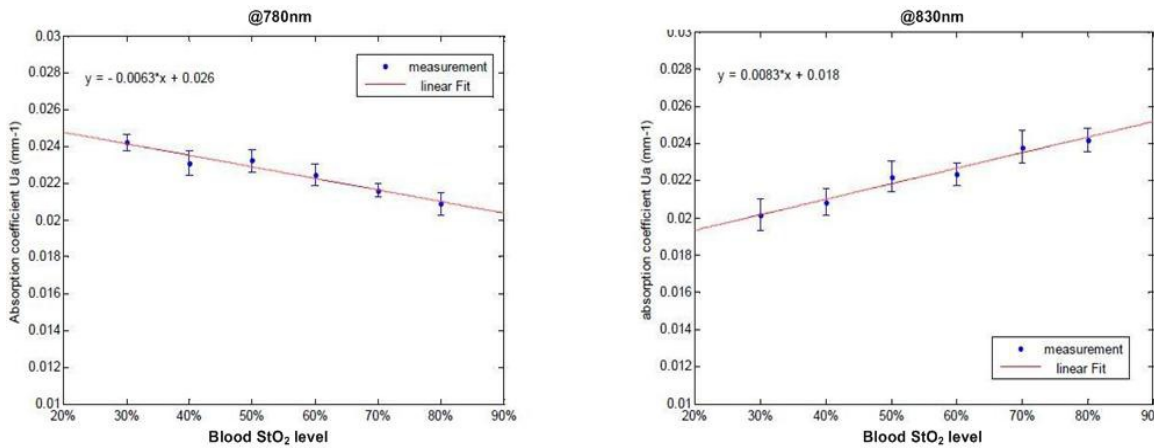


Figure 12. Variation of the hemoglobin absorption coefficient along with the  $\text{StO}_2$  changes



The reconstructed total hemoglobin concentration of the sheep blood circulated to the cylinder container aside the 13mm probe is illustrated in Fig. 13. Constant level of the total hemoglobin concentration was correctly imaged. The reconstructed oxygen saturation of the sheep blood circulated to the cylinder container is illustrated in Fig. 14. The images show correct trend of increased  $StO_2$  levels.

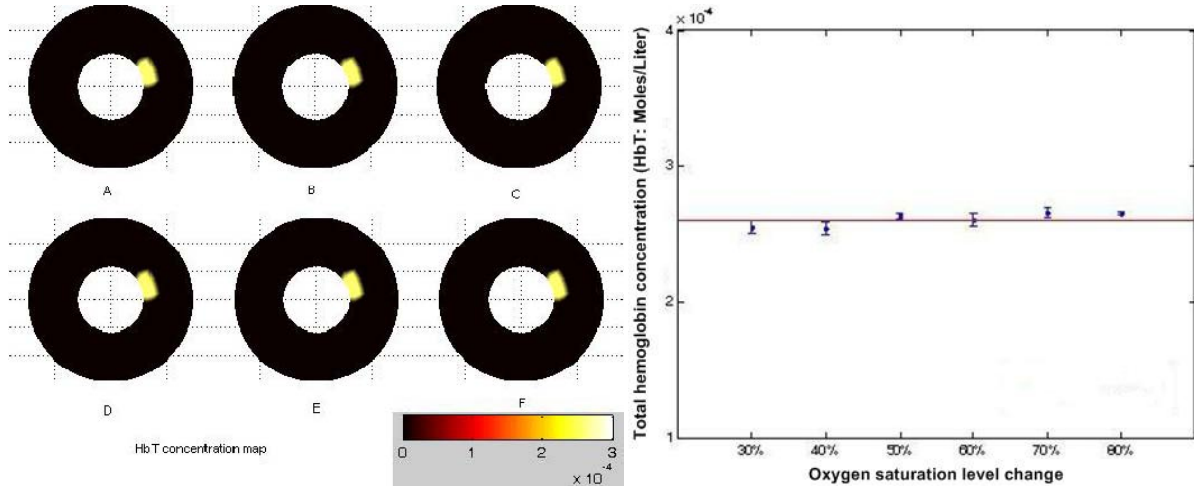


Figure 13. Reconstructed map (left) and the level (right) of the total hemoglobin concentration vs. oxygenation change.

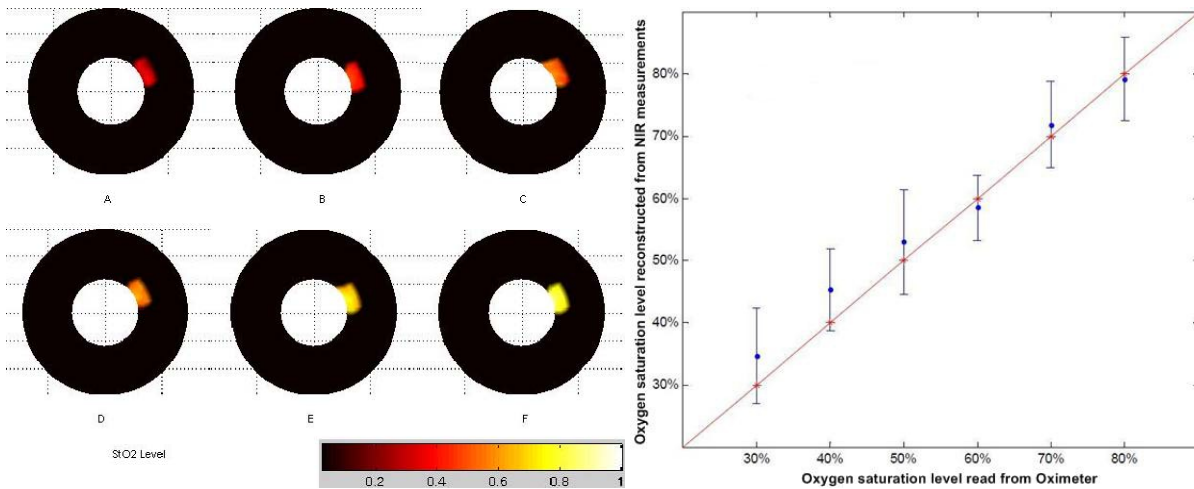


Figure 14. Reconstructed map (left) and the level (right) of the oxygen saturation vs. the true oxygenation change

### 3.3 Dual-band absorption measurements by the 20mm axial—imaging endo-rectal NIR probe.

In the previous measurement by use of the 13mm probe, the 2.5mm separation of the target from the probe surface was too small to be differentiated by the NIR tomography. This is not only related to the relatively low resolution of the NIR tomography, but also to the non-uniform sensitivity of the axial imaging probe along the radial depth [12] as well as the use of photon-diffusion equation without accounting for the circular curvature. Further test on the 20mm axial-imaging probe confirmed that the depth of a target is severely compromised at this axial-imaging geometry without proper analytic treatment of the boundary curvature, as indicated in Fig. 15. A solid cylinder shape phantom (10mm in diameter and 16mm in length) was put into a homogeneous background of 1% solution intralipid. The phantom was put 10mm away (center) from the 20mm probe surface. The solid phantom has the optical properties of  $\mu_a = 0.0064 \text{ mm}^{-1}$ ,  $\mu'_s = 0.91 \text{ mm}^{-1}$ . The high absorption regions reconstructed at two wavelengths are consistent, but at a position close to the probe surface. Improving the depth localization of the axial-imaging NIR tomography may be rendered by incorporating spatial information of the target. Yet, the curvature of the axial-imaging geometry may limit the depth of target being detected.

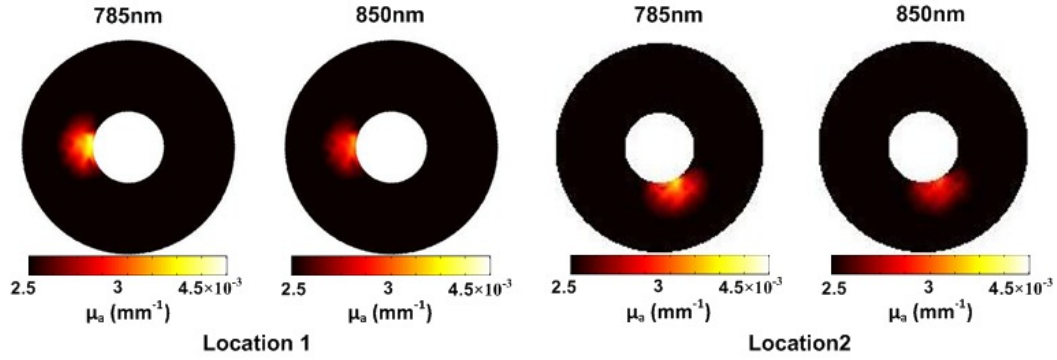


Figure 15. Stand-alone optical reconstruction of transverse images

### 3.4 Dual-band absorption measurements by the sagittal-imaging concurrent NIR/US probe.

The dual-band measurements of absorption based on the sagittal-imaging NIR probe are shown in Fig. 16. A solid phantom target ( $\mu_a=0.0056\text{mm}^{-1}$ ,  $\mu'_s=1.03\text{mm}^{-1}$ ) was put in the middle-sagittal plane of the probe at a depth of 10mm and 15mm, respectively, in a homogeneous background (1% solution intralipid). Both targets appear at the same depth of 10mm by NIR only reconstruction. This target depth corresponds to the maximum depth sensitivity of the probe. The absorption value of the target is also underestimated. Figure 17 shows the dual-band reconstruction after incorporating the spatial information of the target available from the TRUS. The target spatial information is used to develop a mesh representing a target at the correct location and the background. The *prior*-guided NIR reconstruction at both bands gives more accurate recovery of the absorption coefficient of the target.

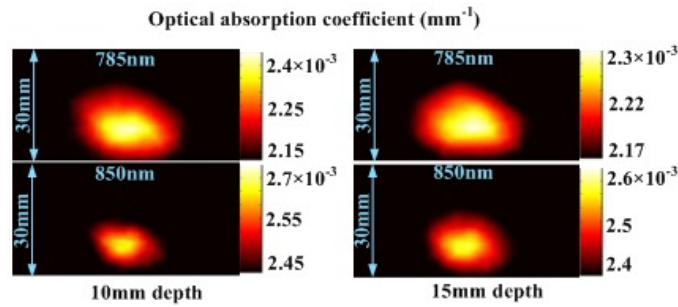


Figure 16. Stand-alone optical reconstruction for sagittal images

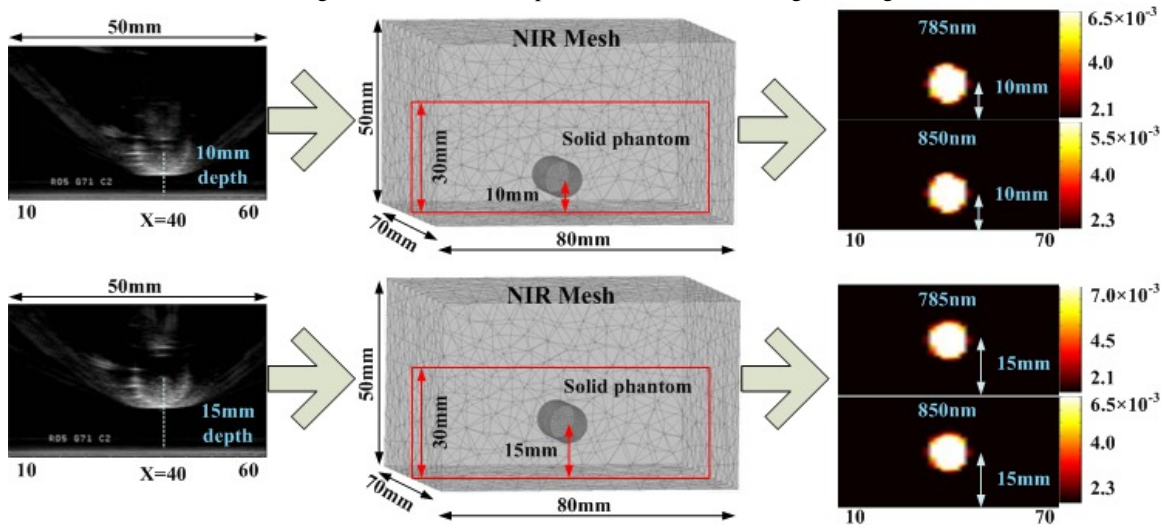


Figure 17. Sagittal images of combined trans-rectal NIR/US probe in different depth



## 4. SUMMARY

We described the development of three NIR imaging probes intended for dual-band endo-rectal imaging of the prostate and ultimately coupling with TRUS for ultrasound-guided NIR image reconstruction. We have demonstrated that oxygenation changes of blood can be quantified by the axial-imaging probe being developed. Work is ongoing to validate the dual-band imaging of the oxygenation in blood samples and with the sagittal-imaging NIR probe, as well as conduct *n vivo* testing with cancer models developed in canine prostate.

## 5. ACKNOWLEDGEMENT

This work has been supported by the Prostate Cancer Research Program of the U.S. Army Medical Research Acquisition Activity (USAMRAA), 820 Chandler Street, Fort Detrick MD, 21702-5014, through grant #W81XWH-07-1-0247. Comments and questions may be directed to Daqing Piao whose e-mail address is daqing.piao@okstate.edu.

## REFERENCES

- [1] Srinivasan, S., Pogue, B.W., Carpenter C., Jiang, S., Wells, W.A., Poplack, S.P., Kaufman P.A. and Paulsen, K.D., "Developments in Quantitative Oxygen-Saturation Imaging of Breast Tissue In Vivo Using Multispectral Near-Infrared Tomography", *Antioxidants & Redox Signaling*, 9(8): 1143-56 (2007).
- [2] Chance B., Nika S., Zhang J., Conant E.F., Hwang E., Briest S., Orel S.G., Schnall M.D., and Czerniecki B.J., "Breast cancer detection based on incremental biochemical and physiological properties of breast cancers: a six-year, two-site study", *Acad Radiol.*, 12: 925-933 (2005).
- [3] Vollmer, R.T., Kantoff, P.W., Dawson, N.A. and Vogelzang, N.J., "Importance of Serum Hemoglobin in Hormone Refractory Prostate Cancer", *Clinical Cancer Research*, 8: 1049-1053 (2002).
- [4] Yu, G., Durduran, T., Zhou, C., Zhu, T.C., Finlay, J.C., Busch, T.M., Malkowicz, S.B., Hahn, S.M. and Yodh, A.G., "Real-time In situ Monitoring of Human Prostate Photodynamic Therapy with Diffuse Light", *Photochemistry and Photobiology*, 82: 1279-1284 (2006).
- [5] Beer, T.M., Tangen, C.M., Bland, L.B., Hussain, M., Goldman, B.H., DeLoughery, T.G. and Crawford, E.D., "The prognostic value of Hemoglobin change after initiating Androgen-Deprivation therapy for newly diagnosed metastatic prostate cancer", *Cancer*, 107(3):489-96 (2006).
- [6] Kondepoti, V.R., Heise, H. M. and Backhaus, J., "Recent application of near-infrared spectroscopy in cancer diagnosis and therapy," *Anal Bioanal Chem*, 390:125-139 (2008).
- [7] Pogue, B.W., Jiang, S., Dehghani, H., Kogel, C., Soho, S., Srinivasan, S., Song, X., Tosteson, T.D., Poplack, S.P. and Paulsen, K.D., "characterization of hemoglobin, water and NIR scattering inbreast tissue:analysis of intersubject variability and menstrual cycle changes," *Journal of Biomedical Optics*, 9(3): 541-552 (2004).
- [8] Piao, D., Jiang, Z., Xu, G., Musgrove, C.H. and Bunting, C.F., "Approach of trans-rectal NIR optical tomography probing for the imaging of prostate with trans-rectal ultrasound correlation", *Proc. SPIE*, 6850: 68500E-1 (2008).
- [9] Xu, G. Piao, D., Musgrove, C.H., Bunting, C.F. and Dehghani H., "Trans-rectal ultrasound-coupled near-infrared optical tomography of the prostate, Part I: Simulation", *Optics Express*, 16(22): 17484–17504 (2008).
- [10] Jiang, Z., Piao D., Xu, G., Ritchey, J.W., Holyoak, G.R., Bartels, K.E., Bunting, C.F., Slobodov, G. and Krasinski, J.S., "Trans-rectal ultrasound-coupled near-infrared optical tomography of the prostate Part II: Experimental demonstration," *Optics Express*, 16(22): 17505–17520 (2008).
- [11] Xie, H., "Dual-spectral endoscopic near-infrared optical tomography for assessment of hemoglobin concentration and oxygen saturation", Oklahoma State University, Master thesis, (2008).
- [12] Musgrove, C., Bunting, C.F., Dehghani, H., Pogue, B.W. and Piao, D., "Computational Aspects of Endoscopic (Trans-rectal) Near-infrared Optical Tomography: Initial Investigations", *Proc. SPIE*, 6434, 643409 (2007).

# A hierarchical spatial *prior* approach for prostate image reconstruction in trans-rectal optical tomography

Guan Xu,<sup>1</sup> Charles F. Bunting,<sup>1</sup> Hamid Dehghani,<sup>2</sup> Daqing Piao<sup>1</sup>

<sup>1</sup> School of Electrical and Computer Engineering, Oklahoma State University,  
Stillwater, OK, 74078-5032

<sup>2</sup> School of Physics, University of Exeter, Exeter, UK, EX4 4QL

## ABSTRACT

An approach of hierarchically implementing the spatial *prior* information in trans-rectal optical tomography is introduced. Trans-rectal optical imaging of the prostate deals with photon propagation through the rectum wall, the peri-prostate tissue and the prostate. Reconstructing a lesion in the prostate is challenging due to the structural complexity as well as the optical heterogeneity. Incorporating spatial “hard” *a priori* information available from complementary imaging modalities such as trans-rectal ultrasound could in principle improve the accuracy of trans-rectal optical tomography reconstruction. However, the reconstruction is potentially subject to the local-minimum sensitivity if the values of all regional optical properties are to be initialized simultaneously. We propose a hierarchical spatial *prior* approach for trans-rectal optical tomography reconstruction. Instead of assigning the initial values to all sub-regions at once, a region is initially assumed homogenous, and the reconstructed optical properties are used as the initial guess for the region as a background when a sub-region is included in the next step. This approach translates to a 3-step iteration routine whereby the first step reconstructs the entire imaging volume as a single region, the second step uses these results as the initial guess of peri-prostate tissue to reconstruct the prostate and the rectum wall, and the third step assigns the updated results as the initial values of 3 existing regions to reconstruct a lesion inside the prostate. This approach, validated by simulation and applied to experimental measurements, is more reliable in global convergence, robust in imaging of single or multiple targets, and accurate for the recovering of optical properties.

**Keywords:** Prostate, optical tomography, trans-rectal, image reconstruction, near-infrared.

## 1. INTRODUCTION

Among the men in USA, prostate cancer is the most common cancer that is only second to skin cancer<sup>[1]</sup>. Prostate cancer screening is performed by measurement of serum prostate-specific antigen (PSA), digital rectal examination (DRE), and a combination of these tests<sup>[2]</sup>. When the suspicion of prostate cancer is raised by abnormal PSA and/or DRE, the diagnosis is made by biopsy, most often performed under trans-rectal ultrasound (TRUS) guidance, to confirm the neoplastic lesions and to determine their clinical significance for treatment planning<sup>[3,4]</sup>. It is known that most times prostate cancer presents as being multi-focal<sup>[5, 6]</sup>, thereby tissue sampling at multiple sites within the prostate gland is necessary.

The most common appearance for prostate cancer on TRUS is a hypoechoic lesion in the peripheral zone. With PSA based screening enabling earlier cancer detection, fewer overt abnormal sonographic findings are being detected at the time of TRUS guided biopsy<sup>[7]</sup>. The sonographic finding of the classic hypoechoic peripheral zone lesion has a sensitivity of cancer detection of 85.5%, specificity of 28.4%, positive predictive value of 29%, negative predictive value of 85.2% and overall accuracy of 43%. The prevalence of isoechoic or nearly invisible prostate cancers on TRUS ranges from 25 to 42%. To date, no biologic differences have been noted between isoechoic and hypoechoic prostate cancers<sup>[8,9]</sup>. The notably high rates of iso-echoic cancers on TRUS imaging leads to increasing the number of biopsy cores to improve the probability of detecting the prostate cancer. However, the current prostate

biopsy strategy of “systematic sampling” results in large number of negative diagnosis performed for initial biopsy evaluations.

TRUS is widely received as a standard imaging modality in performing the prostate biopsy owing to its real-time utility, patient-and-physician friendly features as well as cost-effectiveness. The prostate anatomy and needle track are visualized accurately with TRUS enabling accurate localization of the tissue sites being sampled. TRUS will maintain as the primary imaging guidance for prostate biopsy in the future, thereby the quest of reducing the numbers of unnecessary biopsies demands the specificity of TRUS be improved. Doppler ultrasonography, contrast-enhanced gray-scale ultrasonography, 2<sup>nd</sup>-harmonic imaging, etc. are among the approaches being investigated to improve the outcome of TRUS imaging<sup>[10]</sup>. A more effective approach of improving the outcome of TRUS prostate imaging is, perhaps, to augment the TRUS with a complimentary modality being more specific to the tumor malignancy.

It has been recognized during the past decades that near-infrared (NIR) tomography, being non-ionizing and non-or-minimally-invasive similar to TRUS, has the potential of providing a functional or “surrogate” markers of prostate tumors. Near-infrared measurements of attenuation through tissue have demonstrated significant contrast gradients between blood and parenchymal tissue that is otherwise difficult to obtain<sup>[11-16]</sup>. The alteration of vascularity or the hemoglobin content in the tumor provides, often very high, intrinsic optical contrast between the tumor and benign tissues which has been well demonstrated in breast cancer imaging. When multi-spectral detection is engaged, NIR imaging is also capable of directly quantifying the chromophore concentrations important for determining the local tissue malignancy<sup>[11-16]</sup>. In prostate, studies have shown vascular density gradient in malignant versus benign tissue specimens<sup>[17]</sup>, and different water concentrations in cancerous and benign tissues *in vitro*<sup>[18]</sup>. Invasive NIR measurements of prostate have been conducted for experimental prostate tumors<sup>[19]</sup> and human prostate<sup>[20, 21]</sup>. Surface measurements of implanted prostate tumor have also been reported<sup>[22, 23]</sup>. All these studies demonstrate the potential of using NIR to detect and characterize prostate cancer. NIR diffuse optical measurement, performed interstitially, is also becoming an important tool for monitoring of the photodynamic therapy in prostate<sup>[20, 21, 24]</sup>. Prostate NIR imaging via trans-urethral probing had been analyzed and tested<sup>[25]</sup>. Recently, trans-rectal prostate NIR imaging has been investigated in simulation in the context of assisting MRI for treatment decision<sup>[26]</sup>. NIR optical tomography, when carried out trans-rectally and performed concurrently with TRUS, will improve the specificity of TRUS imaging.

The implementation of trans-rectal NIR tomography for imaging the prostate, similar to other NIR tomography applications, will be benefited by knowing the structural properties of tissue volume being imaged. The tissue volume interrogated by trans-rectal NIR imaging constitutes a nested-domain including a thin layer of rectum wall, a large volume of peri-prostate tissue, a relatively absorbing prostate, and the lesion within the prostate. These nested imaging domains may be further complicated by the pelvic bone, the bladder if not completely voided and other peri-prostatic anatomic structures, that could interfere with the light propagation in the prostate. Previous investigations have discussed the issue of recovering the shapes and optical properties of regions with optical contrast inside non-nested or nested domains<sup>[27-31]</sup>, where the shapes of the regions-of-interest (ROIs) were derived from optical information when no spatial *prior* is available from other complementary imaging modalities. These methods have shown sufficient robustness in recovering the shapes and optical properties of the ROIs, yet the problem of stability and/or slow convergence was noticed in such approaches dealing with nested-domains. In trans-rectal NIR tomography reconstruction the spatial information from TRUS may be implemented by assigning homogenous optical properties within each ROIs of the imaging domain. However, the convergence and the accuracy of reconstruction for trans-rectal NIR tomography of the prostate will likely be more dependent upon the initial guess, given sufficient accuracy of the spatial *prior* information, due to the possible multiple combinations of optical properties in the nested-structures. The image reconstruction in trans-rectal optical tomography is further complicated by the non-consensus regarding the optical contrast that the prostate tumor has with respect to the benign prostate tissue. All these features, as shown in this paper, will complicate and thereby reduce the accuracy of the reconstruction in trans-rectal NIR tomography even with the structural information from TRUS.

In this work, we propose a hierarchical reconstruction scheme that may be more robust and accurate for structural *prior* guided NIR tomography reconstruction of the prostate. This hierarchical method improves both the stability of the convergence and the convergence to the global minimum for the iterative inverse solver. The improvement and robustness of the hierarchical reconstruction approach are demonstrated via simulations and experimental investigations.

## 2. SIMULATION CONFIGURATIONS

### 2.1 Geometry of TRUS coupled trans-rectal NIR imaging of the prostate

We have designed and developed a trans-rectal NIR probe that is directly coupled to a bi-plane TRUS probe (Aloka UST-672-5/7.5). Having more NIR channels in the trans-rectal probe would certainly render more advantageous imaging features, however, the probe dimension and fabrication challenges posed limitation to integrate only 7 source and 7 detector channels to the NIR applicator. The NIR optodes are set laterally aside the sagittal TRUS transducer spanning 60mm×10mm. On each lateral side of the TRUS transducer, the 7 sources or detectors are spaced at 10mm thereby covering a total length of 60mm. The source array and detector array are laterally spaced at 20mm. The geometry of the trans-rectal NIR probe and TRUS transducer with respect to the prostate imaging domain is schematically shown in Fig. 1.

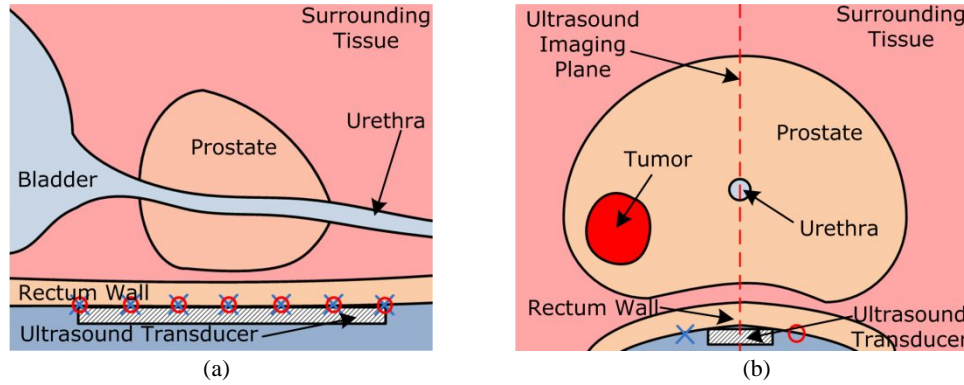


Fig. 1 Illustration of the TRUS coupled trans-rectal NIR imaging of the prostate: (a) sagittal view, (b) transverse view. The middle plane of the sagittal TRUS is marked with a red dash line. The red circles denote NIR sources and the blue crosses denote the NIR detectors.

### 2.2 Model-based trans-rectal optical tomography reconstruction

The prostate and peripheral tissues<sup>[18-21]</sup> are scattering-dominant that justifies describing the light propagation in them by use of the diffusion approximation to the radiative transport equation. We use the frequency-domain photon diffusion equation<sup>[32]</sup>:

$$-\nabla \cdot D(\vec{r}) \nabla U(\vec{r}, \omega) + (\mu_a + \frac{i\omega}{c}) U(\vec{r}, \omega) = q_0(\vec{r}, \omega) \quad (1)$$

where  $U(\vec{r}, \omega)$  is the photon density at position  $\vec{r}$ ,  $q_0(\vec{r}, \omega)$  is the source term,  $\omega$  is the source modulation frequency,  $c$  is the speed of light in medium,  $\mu_a$  is the absorption coefficient, and  $D = [3(\mu_a + \mu'_s)]^{-1}$  is the diffusion coefficient with  $\mu'_s$  being the reduced or transport scattering coefficient.

Equ. (1) is solved under the Type-III boundary condition<sup>[32]</sup> by use of finite-element method<sup>[33]</sup>. The imaging volume to be reconstructed in trans-rectal optical tomography can be divided approximately to, as previously described, 4 domains or ROIs: the rectum wall, the peri-prostate tissue, the prostate, and the prostate tumor. When concurrent TRUS image is available, the thickness of the rectum wall, the size/shape of the prostate, and the approximate spatial extent of the prostate lesion can be defined to guide trans-rectal optical tomography reconstruction. We utilize the TRUS structural information by the “hard” *a priori* method<sup>[34-36]</sup>. The “hard” *a priori* method treats each ROI as homogenous, thereby in our reconstruction 8 parameters are to be recovered as  $\mu_a$  and  $\mu'_s$  of the four ROIs. The Jacobian values are calculated for each ROI instead of for each node in every ROI and has the form of:

$$\begin{bmatrix} \frac{I_{i,j}}{\mu_{a\_ROI\_k}} & \frac{I_{i,j}}{D_{ROI\_k}} \\ \frac{\phi_{i,j}}{\mu_{a\_ROI\_k}} & \frac{\phi_{i,j}}{D_{ROI\_k}} \end{bmatrix} \quad (2)$$

where  $I_{i,j}$  ( $i, j = 1, 2, \dots, 7$ ) and  $\phi_{i,j}$  ( $i, j = 1, 2, \dots, 7$ ) are the intensity and phase terms of  $U(\vec{r}, \omega)$ , respectively. In (2),  $k=1, 2, 3, 4$  denote “rectum wall”, “peri-prostate tissue”, “prostate”, and “prostate lesion”, which are the four ROIs, respectively. The optical properties are iteratively recovered by use of the well-known Levenberg-Marquart (LM) algorithm wherein the ROI-specific values of  $\mu_a$  and  $D$  are updated according to

$$x_{k+1} = x_k + \alpha \cdot [J^T(x_k)J(x_k) + \lambda I]^{-1} J^T(x_k) \Delta v(x_k) \quad (3)$$

where  $x$  is the array of parameters to be optimized,  $J$  is the Jacobian matrix defined by Equ. (2),  $\Delta v$  is the forward projection error,  $\lambda$  is a penalty or regularization term. In the iteration a small damping factor  $\alpha$  in the range of (0, 1) is used to stabilize the convergence<sup>[37]</sup>.

### 2.3 TRUS prior assisted finite-element mesh for trans-rectal NIR tomography reconstruction

Utilizing TRUS structural information to guide trans-rectal NIR tomography reconstruction could be performed by using the location and size of a suspected lesion to directly generate a mesh that contains two ROIs to represent the lesion with a dense mesh and the background tissue with a coarse mesh<sup>[35, 36]</sup>. For trans-rectal prostate imaging a mesh is needed to represent regions including the rectum wall, the peri-prostate tissue, the prostate, and the tumor within the prostate.

The TRUS image (available in open source) was imported into a software 3ds-MAX [Autodesk Inc] for primary 3-D model generation. The finalized 3-D mesh of the prostate is converted to COMSOL Multiphysics [COMSOL AB] compatible format with MeshToSolid [Syncode Inc]. The absorption and reduced scattering coefficients of rectum, peri-prostate tissue, and prostate are assumed homogenous in each individual ROI and assigned based on<sup>[26]</sup>. A spherical shape is adopted for the prostate tumor. Figure 2 illustrates one completed NIR FEM-mesh. The prostate in Fig. 2 has a walnut shape of  $\sim 50 \times 40 \times 30 \text{ mm}^3$  in the maximum extensions. The rectum wall has a thickness of 4mm and a curvature radius of 80 mm. The completed mesh similar to that shown in Fig. 2 contains approximately 4000 nodes and 20000 elements.

The source-modulation frequency  $\omega$  in Equ. (1) is set at 100MHz, and 1% Gaussian noise is added to all forward calculations to form the measurement data. In all the figures presented thereafter, the unit of the length is millimeter,  $x$  is the longitudinal coordinate in the range of [0, 80],  $y$  is the lateral coordinate in the range of [0, 80], and  $z$  is the depth coordinate in the range of [0, 80].

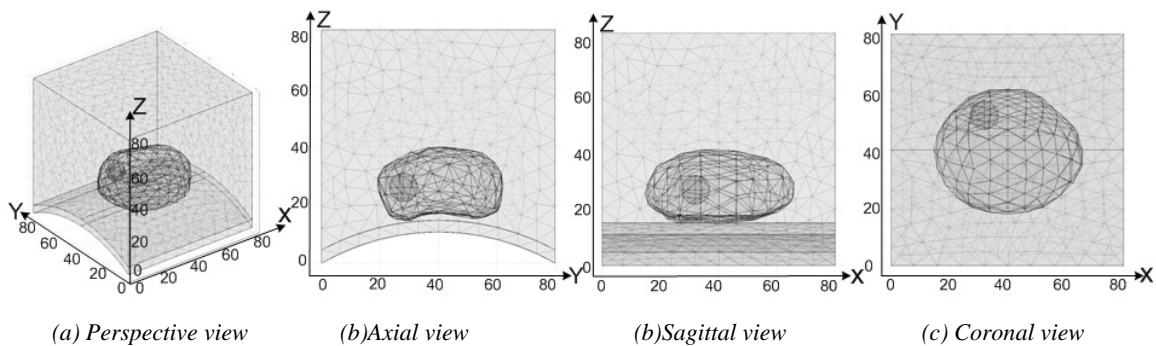


Fig. 2 FEM mesh of the NIR imaging volume generated based on TRUS image

### 3. A HIERARCHICAL SPATIAL PRIOR APPROACH FOR NIR TOMOGRAPHY RECONSTRUCTION

### 3.1 Trans-rectal NIR imaging reconstruction without *a priori* information

The performance of recovering a tumor target by trans-rectal NIR tomography without structural *prior* is first examined. With the accurate forward measurement being calculated by the TRUS-defined geometry as shown in Fig. 2, the iterative image reconstruction is conducted using mesh of homogenous element density throughout the entire volume. The optical properties of a 10mm diameter tumor target is assigned as  $\mu_a = 0.02\text{mm}^{-1}$  and  $\mu_s' = 1.6\text{mm}^{-1}$ , with the parameters of other regions the same as those in Fig. 2 and listed in Table 1 coming later in the text. The reconstruction results are given in Fig. 3 for the tumor target being placed at left, middle, and right locations inside the prostate. The (a) is for  $\mu_a$  and (b) is for  $\mu_s'$  respectively. The 1-dimensional profile across the tumor and parallel to the probe surface indicates the quantitative comparison between the set and reconstructed values. It is observed that the existence of a heterogeneous structure in the prostate region is rendered, but the spatial characterization of the heterogeneity is poor. Further, a tumor with negative absorption contrast is difficult to be recovered when the spatial *prior* is not implemented.

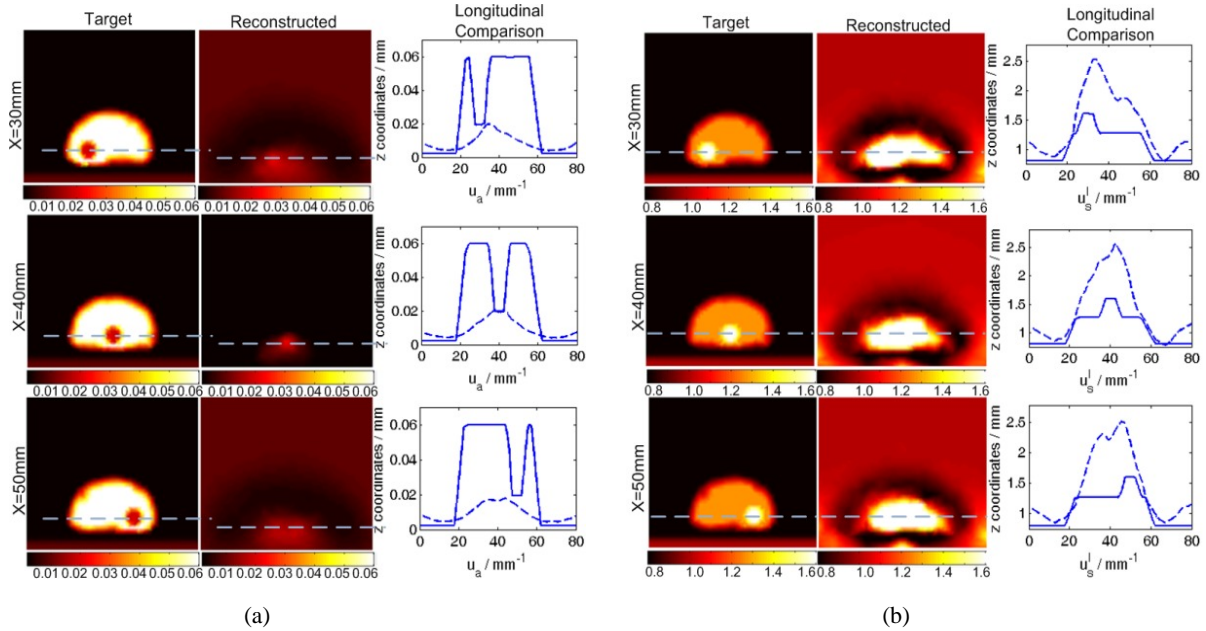


Fig. 3 NIR-only reconstruction for target in varying longitudinal locations. Optical properties are plotted to along line  $y=40\text{mm}$ ,  $z=26\text{mm}$  (actual depth is 15.1mm because of the bottom curvature of the mesh) for both the target and the reconstructed images (a) Recovery of  $\mu_a$ .  $\mu_a$  values are intentionally plotted along the line going through the center of the reconstructed blobs ( $\sim y=40\text{mm}$ ,  $z=26\text{mm}$ , actual depth is approximately 15.1mm because of the bottom curvature of the mesh), which is shallower because the non-uniform sensitivity has dragged the reconstructed target closer to the NIR array. (b) Recovery of  $\mu_s'$  for the target locations identical to those in (a).

### 3.2 Spatial *prior* guided trans-rectal NIR reconstruction-----simultaneous updating of all ROIs

The trans-rectal prostate imaging domain constitutes nested-structures including a thin layer of rectum wall in the vicinity of NIR array, a large and under-defined volume of peri-prostate tissue owing to the one-sided NIR array, a relatively absorbing prostate, and the lesion within the prostate. In our approach of coupling trans-rectal NIR with TRUS, the shapes of the ROIs for trans-rectal optical tomography reconstruction could be defined directly from TRUS. The simplest approach of implementing the TRUS *a priori* information may be assigning homogenous optical properties within each ROIs of the imaging domain. However the convergence and the accuracy of reconstruction will still be dependent on the initial guess. This can be attributed to the gradient based solver for which the local minimum feature would likely be exaggerated in prostate imaging in which the multiple combinations of optical properties of the nested-structures in the imaging volume could give multiple combinations

of optical properties that may fit with the measurements, in which case the projection error of the reconstruction routine could converge to a very small value but the recovered optical properties may be far from the desired ones, as is shown in Fig. 4(c). The local-minimum problem makes the reconstruction sensitive to the initial guess of optical properties. In trans-rectal optical tomography finding the global minimum for the iterations to converge may become particularly intriguing.

When TRUS *prior* is available, a conventional way of utilizing the TRUS spatial information would be the “hard” *a priori* method in which the optical properties of each ROIs are set homogenous and updated simultaneously at each iteration. However, we have found that this conventional approach may not lead to reliable convergence for prostate imaging, which is believed due to the local-minimum problem. One example is given in Table 1 where the calculation is taken for the NIR array in Fig. 1(c), the prostate model in Fig. 2, and a target of 10mm in diameter located at a coordinate setting of (40, 40, 26) that is 15.1 mm from the rectal surface. When the four ROIs including the rectum, the peri-prostate tissue, the prostate, and the prostate tumor are updated simultaneously from the same initial guess of  $\mu_a = 0.01 \text{ mm}^{-1}$  and  $\mu_s' = 1.0 \text{ mm}^{-1}$ , the iteration stops after 1 round due to the negative  $\mu_a$  value obtained for the rectum wall. This is due largely to the effect that the iteration has fallen into local minimums which were the minimum values locally but not globally.

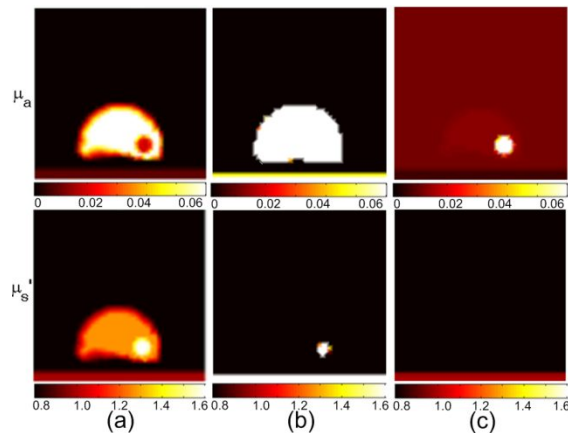


Fig. 4 Local-minimum issue in reconstruction. The forward calculation is based on (a). (b) Reconstruction results with the initial values of all regions as  $\mu_a = 0.1 \text{ mm}^{-1}$  and  $\mu_s' = 2 \text{ mm}^{-1}$ , the iterations stopped with projection error of 123.0100. (c) Reconstruction results with the initial values of all regions as  $\mu_a = 0.002 \text{ mm}^{-1}$  and  $\mu_s' = 0.5 \text{ mm}^{-1}$ , the final projection error of the iterations is 0.8329.

Table 1 Results of simultaneously updating the 4 ROIs from the same initial guess

Regions	$\mu_a \text{ (mm}^{-1}\text{)}$				$\mu_s' \text{ (mm}^{-1}\text{)}$			
	Surrounding Tissue	Rectum Wall	Prostate	Tumor	Surrounding Tissue	Rectum Wall	Prostate	Tumor
Set value	0.002	0.01	0.06	0.02	0.8	1	1.27	1.6
Simultaneous Update	0.1216	<b>-0.008</b>	0.026	0.0215	1.1482	2.3602	0.6173	0.7073

### 3.3 Spatial-prior guided trans-rectal NIR reconstruction-----hierarchical updating of the ROIs

The local minimum problem may be mitigated by a hierarchical spatial *prior* approach that may allow more steady and global convergence of the iteration. The fundamental idea of this method is to first reconstruct the global optical properties of the entire volume, then to reconstruct the optical properties of prostate and rectum wall, and last to reconstruct the tumor lesion area. The 2<sup>nd</sup> and 3<sup>rd</sup> steps use the value obtained in the previous step as the initial guess



of that specific ROI. Therefore at each step, the perturbation by a relatively smaller region is less influential and convergence of iteration is better warranted. The detailed steps are shown in Fig. 5 and described in below:

(a) The first iterations assume an entirely homogenous imaging volume. In this round the initial projection errors will be large and the converging process is most likely to be affected by the global minimum. Therefore, a single set of optimum values of  $\mu_a$  and  $\mu_s$  are determined with LM algorithm and will be used as the initial guess in the second step.

(b) The second iterations consider three regions of rectum wall, peri-prostate tissue, and prostate within the imaging volume. The iterations of optical properties of these three ROIs start at the same initial guess provided in step (a) and converge at different values.

(c) The values obtained from step (b) are used as the initial guess for the same three ROIs but with a tumor added to the prostate. The tumor and the prostate take the same initial values resulted from the previous step. Now each of the four ROIs (rectum wall, peri-prostate tissue, prostate, and tumor) converges to different end values.

The comparison of the optical properties reconstructed at each step is shown in Fig. 5(d). The change of the overall projection error for the three steps is plotted in Fig. 5(e). Rapid and reliable convergence can be observed.

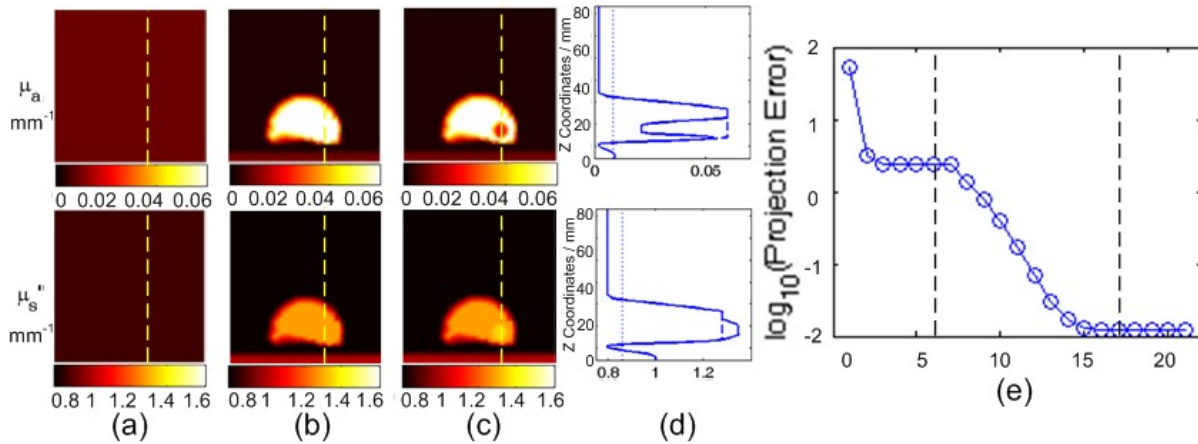


Fig. 5. The 3-step hierarchical reconstruction method (a) Step 1—one ROI for the entire volume; (b) step 2—three ROIs representing rectum wall, peri-prostate tissue, prostate; (c) step 3—four ROIs representing rectum wall, peri-prostate tissue, prostate, tumor; (d) The recovered optical properties along the z direction at  $x=40\text{mm}$ ,  $y=50\text{mm}$ . The dot line denotes the step 1, the dash line the step 2 and the solid line the step 3; (e) changes of the projection error, where the dash lines separate the converging of the three steps in (a)—(c).

## 4. Validation of the hierarchical spatial *prior* method

### 4.1 Simulation geometry

Recently, Li et al. reported simulation results for trans-rectal optical tomography reconstruction in the context of using MRI anatomic information<sup>[26]</sup>. Their work is referred as “NIR/MRI” in the following text. We have tested the performance of our hierarchical spatial *prior* method using the probe geometry (shown in Fig. 6) and the optical properties presented in the NIR/MRI work.

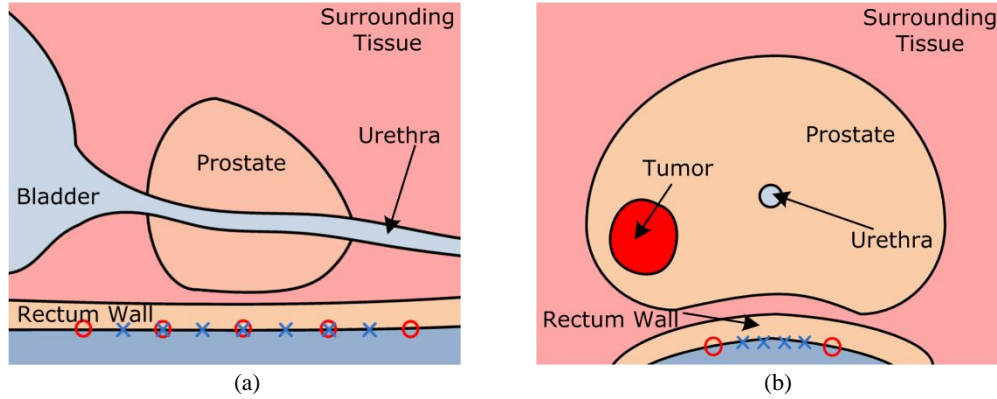


Fig. 6 The imaging geometry used in the NIR/MRI paper<sup>[26]</sup>. Two source arrays are distributed laterally with 20mm distance. Each array has 5 sources with 10mm gaps, as denoted by red circles. 28 detectors are evenly distributed within a 15mm by 30mm area, as denoted by blue crosses. (a) Sagittal view of the distribution of the optodes. (b) Transversal view of the distribution of the optodes.

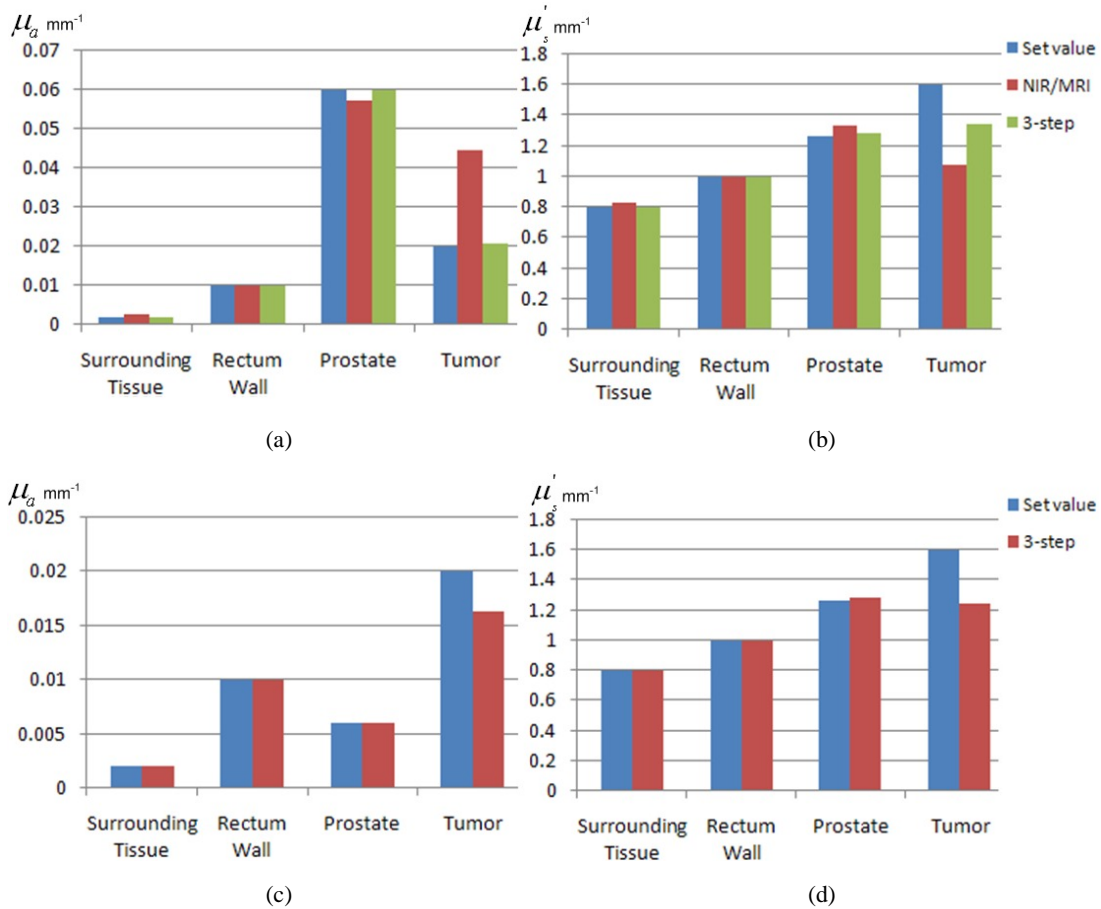


Fig. 7 Comparison of the reconstruction values: (a) & (b) the tumor has a negative absorption contrast with respect to the prostate, (c) & (d) the tumor has a positive absorption contrast with respect to the prostate. The “3-step” refers to the hierarchical image reconstruction method.

With the 1% noise added to the forward simulation data as is indicated in the NIR/MRI paper, the performance of our hierarchical spatial *prior* method with respect to the NIR/MRI one is given in Fig. 7 (a) & (b) for a prostate lesion of negative absorption contrast. It is observed that our hierarchical method (listed as “3-step” in the

table), as expected, slightly outperforms the NIR/MRI method in terms of the accuracy of recovering optical properties. We have also tested recovering a target of positive absorption contrast in Fig. 7(c) & (d) using the NIR/MRI probe geometry and our 3-step method. Since no results were given in the NIR/MRI work for target of positive absorption contrast, only the recovered properties based on our method are presented for comparison with the set values. In (c) & (d) the absorption coefficient of prostate is set much lower than that in (a) & (b) but the tumor optical properties are kept the same as those in (a) & (b). If the absorption of prostate in (c) & (d) is kept the same as in (a) & (b), the positive absorption target is hardly reconstructed at the set location. The choice of lower prostate absorption is for testing our hierarchical method, but it does not necessarily disagree with the actual value of prostate absorption. As a matter of fact, the absorption properties of prostate has shown large variation in literatures where the measurement are either taken from *in vitro* tissue or may be interfered by bleeding of *in vivo* tissue under invasive measurement. The absorption coefficient of non-exposed prostate measured *in situ* & *in vivo* is unavailable so far, and if available, is likely lower than the values reported in literatures for non-intact prostate. The results in Fig. 7 demonstrate the robustness of our hierarchical spatial *prior* method in reconstructing prostate lesion with either negative or positive absorption contrast.

## 4.2 Experimental validations of the hierarchical reconstruction

Two sets of experimental data acquired with continuous-wave NIR imaging system were employed to evaluate the hierarchical reconstruction scheme. The samples were administrated mostly with absorption contrast; therefore results of only absorption reconstruction are displayed in the following figures.

### Case I: Internal imaging of avian tissues

As shown in Fig. 8(a), the empty abdomen of a whole chicken was filled with chicken breast tissue and a piece of chicken liver was embedded within the breast tissue. The embedded liver shows up as the hypo-echoic region circled in Fig. 8(b). A two-ROI FEM mesh is generated to simulate the experiment setup, as is shown in Fig. 8(d).

Since there are only two ROI in this experimental case, when implementing the hierarchical reconstruction scheme, only a two-step reconstruction is performed. The results are shown in Fig. 8(e) & (f), respectively. It can be observed that the absorption values are reconstructed quite close to the true values of a liver tissue indicated by literature findings. Comparing the NIR images reconstructed without structural *prior* in Fig. 8(c) and reconstructed with hierarchical method in Fig. 8(f), the utility of the hierarchical reconstruction method is demonstrated.

### Case II: Trans-rectal optical tomography of canine prostate in situ

The second experiment is conducted on a canine cadaver. The prostate was exposed and approximately 0.33ml of homogenized foal liver was injected ventral-dorsally, paramedian in the left lobe of the prostate. The prostate was then enclosed in thick layers of peri-prostate tissues. On the TRUS image of Fig. 9(a) the injected liver tissue is visible by the mass proximal to the center of the prostate and the vertical hyper-echoic strip at the ventral side of the prostate. The large hypo-echoic region at the upper half was due to absorption by thick layers of muscle, skin and exposure to the air. The mesh is accordingly generated in Fig. 9(b). The rectum wall was not outlined in the mesh because of its close proximity to the US transducer due to the small size of this canine cadaver. The finalized mesh in Fig. 9(b) shows nested-domains including the prostate and a target region in the prostate. The NIR images in Fig. 9(c), (d), and (e) show the absorption distribution reconstructed at each step of the hierarchical reconstruction method. A highly absorptive mass is clearly recovered corresponding to the injected liver tissue. The absorption coefficient of the foal liver tissue in Fig. 9(a) is lower than that of the avian liver tissue in Fig. 8(b); nevertheless both values are at the order of  $0.1\text{mm}^{-1}$ , indicating high absorption by both tissues.

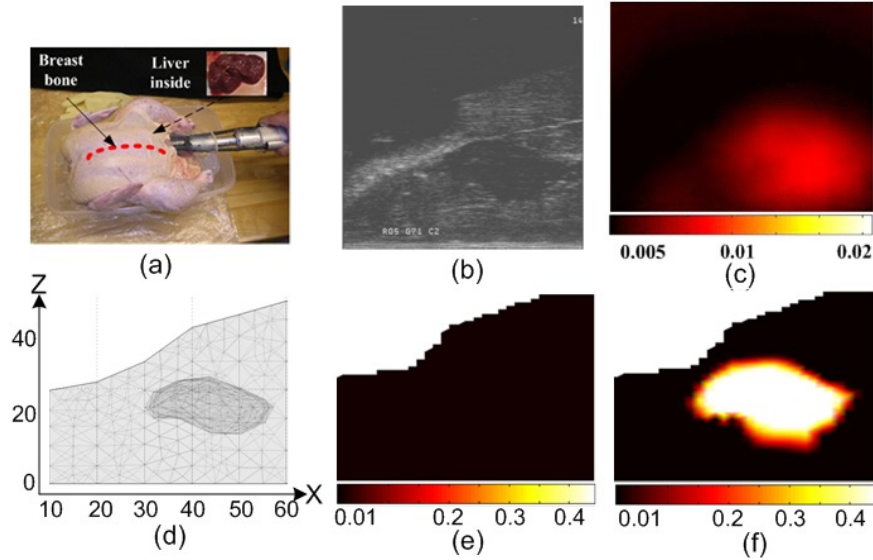


Fig. 8 Experiment I: Internal imaging of avian tissues. (a) Tissue phantom. (b) Ultrasound imaging. (c) NIR-only reconstruction. (d) FEM mesh. (e) Reconstruction step 1: background. (f) Reconstruction step 2 with the target structure

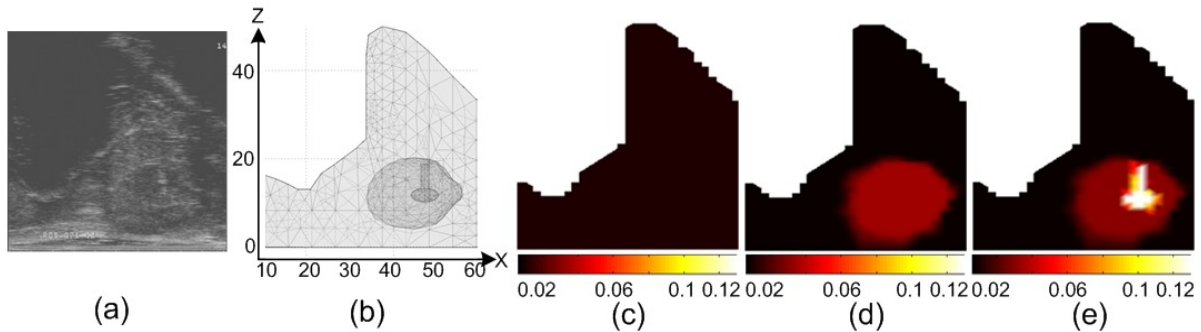


Fig. 9 Experiment II: Imaging on canine cadaver. (a) TRUS imaging (b) FEM mesh. (c), (d), (e) the 3 steps of hierarchical reconstruction

## 5. DISCUSSION AND SUMMARY

In this paper, a structural *prior* guided hierarchical NIR tomography reconstruction scheme aimed at improving the reconstruction accuracy of trans-rectal optical tomography of the prostate is presented. The method is developed under the framework of utilizing the trans-rectal ultrasound information as the structural *prior*. Nevertheless, the hierarchical method could be extended to implementing other high-resolution imaging modalities such as MRI to guide NIR tomography and to applying NIR tomography in other complicated tissue domains. The accuracy of the hierarchical reconstruction method, as indicated by the simulation and experimental investigations, relies on explicit demarcation of the inner structure of the imaging volume to form the region-resolved FEM mesh. In prostate a large amount of the cancer may be shown iso-echoic on TRUS. Thereby the utility or accuracy of this hierarchical imaging approach is hindered when TRUS images do not specify a suspicious region. Under such circumstance, the third step of recovering the tumor lesion in the prostate may proceed by reconstructing the optical properties on every element within the prostate but the overall accuracy of the reconstruction must be compromised.

In summary, an approach of hierarchically implementing the spatial *prior* information in trans-rectal optical tomography is introduced. Trans-rectal optical imaging of the prostate is challenging due to the structural complexity as well as the optical heterogeneity. Incorporating spatial “hard” *a priori* information available from complementary imaging modalities such as trans-rectal ultrasound is potentially subject to the local-minimum

sensitivity if the values of all regional optical properties are to be initialized simultaneously. A hierarchical spatial *prior* approach for trans-rectal optical tomography reconstruction does not assign the initial values to all sub-regions at once, instead a region is initially assumed homogenous, and the reconstructed optical properties are used as the initial guess for the region as a background when a sub-region is included in the next step. This approach translates to a 3-step iteration routine whereby the first step reconstructs the entire imaging volume as a single region, the second step uses these results as the initial guess of peri-prostate tissue to reconstruct the prostate and the rectum wall, and the third step assigns the updated results as the initial values of 3 existing regions to reconstruct a lesion inside the prostate. The robustness of this approach is demonstrated in both simulations and experiments.

## ACKNOWLEDGEMENT

This work has been supported by the Prostate Cancer Research Program of the U.S. Army Medical Research Acquisition Activity (USAMRAA), 820 Chandler Street, Fort Detrick MD, 21702-5014, through grant #W81XWH-07-1-0247.

## REFERENCES

- [1] Jemal, A., Siegel, R., Ward, E., Murray, T., Xu, J., and Thun, M. J., "Cancer statistics, 2007," *CA Cancer J. Clin.* 57, 43-66 (2007).
- [2] Polascik, T. J., Oesterling, J. E., and Partin, A. W., "Prostate specific antigen: a decade of discovery—what we have learned and where we are going," *J. Urol.* 162, 293-306 (1999).
- [3] Grossfeld, G. D. and Carroll, P. R., "Prostate cancer early detection: a clinical perspective," *Epidemiol. Rev.* 23, 173-80 (2001).
- [4] Loch, A. C., Bannowsky, A., Baeurle, L., Grabski, B., König, B., Flier, G., Schmitz-Krause, O., Paul, U., and Loch, T., "Technical and anatomical essentials for transrectal ultrasound of the prostate," *World J. Urol.* 25, 361-366 (2007).
- [5] Wise, A. M., Stamey, T. A., McNeal, J. E., and Clayton, J. L., "Morphologic and clinical significance of multifocal prostate cancers in radical prostatectomy specimens," *Urology* 60, 264-9 (2002).
- [6] Miller, G. J. and Cygan, J. M., "Morphology of prostate cancer: the effects of multifocality on histological grade, tumor volume and capsule penetration," *J. Urol.* 152, 1709-13 (1994).
- [7] Purohit, R.S., Shinohara, K., Meng, N.V., Carroll, P.R., "Imaging clinically localized prostate cancer," *Urol. Clin. North Am.*, 30(2),279-93. Review (2003).
- [8] Shinohara, K., Wheeler, T., and Scardino, P., "The appearance of prostate cancer on transrectal ultrasonography: correlation of imaging and pathological examinations," *J. Urol.* 142, 76 (1989).
- [9] Tang, J., Yang, J.C., Li, Y., Li, J., Shi, H., "Peripheral zone hypoechoic lesions of the prostate: evaluation with contrast-enhanced gray scale transrectal ultrasonography," *J Ultrasound Med*, 26(12), 1671-9(2007).
- [10] Linden, R.A., and Halpem, E.J., "Advances in transrectal ultrasound imaging of the prostate," *Semin Ultrasound CT MR*, 28(4), 249-57 (2007).
- [11] Tromberg, B., Coquoz, J., Fishkin, O., Pham, J. B., Anderson, T., Butler, E. R., Cahn, J., Gross, M., Venugopalan, J. D., and Pham, D., "Non-invasive measurements of breast tissue optical properties using frequency-domain photon migration," *Phil. Trans. R. Soc. Lond. B* 352, 661-668 (1997).
- [12] Pogue, B. W., Poplack, S. P., McBride, T.O., Wells, W. A., Osterman, K. S., Osterberg, U. L., and Paulsen, K. D., "Quantitative hemoglobin tomography with diffuse near-infrared spectroscopy: pilot results in the breast," *Radiology* 218, 261-266 (2001).
- [13] Ntzichristos, V. and Chance, B., "Probing physiology and molecular function using optical imaging: applications to breast cancer," *Breast Cancer Res.* 3, 41-46 (2001).
- [14] Choe, R., Corlu, A., K. Lee, Durduran, T., Konecky, S. D., Grosicka-Koptyra, M., Arridge, S. R., Czerniecki, B. J., Fraker, D. L., DeMichele, A., Chance, B., Rosen, M. A., and Yodh, A. G., "Diffuse optical tomography of breast cancer during neoadjuvant chemotherapy: a case study with comparison to MRI," *Med. Phys.* 32, 1128-1139 (2005).
- [15] Franceschini, M. A., Moesta, K. T., Fantini, S., Gaida, G., Gratton, E., Jess, H., Mantulin, W. W., Seeber, M., Schlag, P. M., and Kaschke, M., "Frequency-domain techniques enhance optical mammography: initial clinical results," *Proc. Nat. Acad. Sci. USA* 94, 6468-6473 (1997).
- [16] Zhu, Q., Cronin, E. B., Currier, A. A., Vine, H. S., Huang, M., Chen, N., and Xu, C., "Benign versus malignant breast masses: optical differentiation with US-guided optical imaging reconstruction," *Radiology* 237, 57-66 (2005).
- [17] Bigler, S. A., Deering, R. E., and Brawer, M. K., "Comparison of microscopic vascularity in benign and malignant prostate tissue," *Hum. Pathol.* 24, 220-226 (1993).
- [18] Ali, J. H., Wang, W. B., Zevallos, M., and Alfano, R. R., "Near infrared spectroscopy and imaging to probe differences in water content in normal and cancer human prostate tissues," *Technol. Cancer Res. Treat.* 3, 491-497 (2004).
- [19] Arnfield, M. R., Chapman, J. D., Tulip, J., Fenning, M. C., and McPhee, M. S., "Optical properties of experimental prostate tumors in vivo," *Photochem. Photobiol.* 57, 306-311 (1993).
- [20] Zhu, T. C., Dimofte, A., Finlay, J. C., et al. "Optical properties of human prostate at 732 nm measured in mediated photodynamic therapy," *Photochem. Photobiol.* 81, 96-105 (2005).
- [21] Svensson, T., Andersson-Engels, S., Einarsson, M., and Svanberg, K., "In vivo optical characterization of human prostate tissue using near-infrared time-resolved spectroscopy," *J. Biomed. Opt.* 12, 014022 (2007).
- [22] Goel, M., Radhakrishnan, H., Liu, H., et al. "Application of near infrared multi-spectral CCD imager system to determine the hemodynamic changes in prostate tumor," in *OSA Biomedical Topical Meetings* (Optical Society of America, 2006), paper SH10.
- [23] Liu, H., Song, Y., Worden, K. L., Jiang, X., Constantinescu, A., and Mason, R. P., "Noninvasive investigation of blood oxygenation dynamics of tumors by near-infrared spectroscopy," *Appl. Opt.* 39, 5231-43 (2000).
- [24] Zhou, X. and Zhu, T. C., "Image reconstruction of continuous wave diffuse optical tomography (DOT) of human prostate," in *Proceedings of the COMSOL Users Conference*, n/a, (2006).

- [25] Jacques, S. L. and Motamedi, M., "Tomographic needles and catheters for optical imaging of prostatic cancer," Proc. SPIE 2395, 111-118 (1995).
- [26] Li, C., Liengsawangwong, R., Choi, H., and Cheung, R., "Using *a priori* structural information from magnetic resonance imaging to investigate the feasibility of prostate diffuse optical tomography and spectroscopy: a simulation study," Med. Phys. 34, 266-274 (2007).
- [27] Schweiger, M., Arridge, S. R., Dorn, O., Zacharopoulos, A., and Kolehmainen, V., "Reconstructing absorption and diffusion shape profiles in optical tomography using a level set technique," Opt. Lett. 31, 471-473 (2006).
- [28] Kolehmainen, V., Arridge, S. R., Lionheart, W. R. B., Vauhkonen, M., and Kaipio, J. P., "Recovery of region boundaries of piecewise constant coefficients of an elliptic PDE from boundary data," Inverse Probl. 15, 1375-1391 (1999).
- [29] Kolehmainen, V., Vauhkonen, M., Kaipio, J. P., and Arridge, S. R., "Recovery of piecewise constant coefficients in optical diffusion tomography," Opt. Express 7, 468-480 (2000).
- [30] Kolehmainen, V., Arridge, S. R., Vauhkonen, M., and Kaipio, J. P., "Simultaneous reconstruction of internal tissue region boundaries and coefficients in optical diffusion tomography," Phys. Med. Biol. 45, 3267-3284 (2000).
- [31] Srinivasan, S., Pogue, B. W., Dehghani, H., Jiang, S., Song, X., and Paulsen, K. D., "Improved quantification of small objects in near-infrared diffuse optical tomography," J. Biomed. Opt. 9, 1161-1171 (2004).
- [32] Pogue, B. W., Geimer, S., McBride, T. O., Jiang, S., Osterberg, U. L., and Paulsen, K. D., "Three-dimensional simulation of near-infrared diffusion in tissue: boundary condition and geometry analysis for finiteelement image reconstruction," Appl. Opt. 40, 588-600 (2001).
- [33] Schweiger, M., Arridge, S. R., and Delpy, D. T., "Application of the finite-element method for the forward and inverse models in optical tomography," J. Math. Imag. Vision 3, 263-283 (1993).
- [34] Dehghani, H., Carpenter, C. M., Yalavarthy, P. K., Pogue, B. W., and Culver, J. P., "Structural *a priori* information in near-infrared optical tomography," Proc. SPIE 6431, 64310B1 (2007).
- [35] Zhu, Q., Durduran, T., Ntziachristos, V., Holboke, M., and Yodh, A. G., "Imager that combines near-infrared diffusive light and ultrasound," Opt. Lett. 24, 1050-1052 (1999).
- [36] Holboke, M. J., Tromberg, B. J., Li, X., Shah, N., Fishkin, J., Kidney, D., Butler, J., Chance, B., and Yodh, A. G., "Three-dimensional diffuse optical mammography with ultrasound localization in a human subject," J. Biomed. Opt., 5, 237-47 (2000).
- [37] Yu, X., Chen, G., and Cheng, S., "Dynamic learning rate optimization of the backpropagation algorithm," IEEE Trans. Neural Netw. 6, 669-677 (1995).

# ***In vivo* trans-rectal ultrasound coupled trans-rectal near-infrared optical tomography of canine prostate bearing transmissible venereal tumor**

Zhen Jiang,<sup>1</sup> G. Reed Holyoak,<sup>2</sup> Kenneth E. Bartels,<sup>2</sup> Jerry W. Ritchey,<sup>3</sup>  
Guan Xu,<sup>1</sup> Charles F. Bunting,<sup>1</sup> Gennady Slobodov,<sup>4</sup> Jerzy S. Krasinski,<sup>1</sup> Daqing Piao<sup>1\*</sup>

<sup>1</sup> *School of Electrical and Computer Engineering, Oklahoma State University,  
Stillwater, OK 74078 USA*

<sup>2</sup> *Department of Veterinary Clinical Sciences, Oklahoma State University, Stillwater, OK 74078 USA*

<sup>3</sup> *Department of Veterinary Pathobiology, Oklahoma State University, Stillwater, OK 74078 USA*

<sup>4</sup> *Department of Urology, University of Oklahoma Health Science Center,  
Oklahoma City, OK 73104 USA*

\*E-mail: [daqing.piao@okstate.edu](mailto:daqing.piao@okstate.edu)

**Abstract:** *In vivo* trans-rectal near-infrared (NIR) optical tomography is conducted on a tumor-bearing canine prostate with the assistance of trans-rectal ultrasound (TRUS). The canine prostate tumor model is made possible by a unique round cell neoplasm of dogs, transmissible venereal tumor (TVT) that can be transferred from dog to dog regardless of histocompatibility. A characterized TVT cell line was homogenized and passed twice in subcutaneous tissue of NOD/SCID mice. Following the second passage, the tumor was recovered, homogenized and then inoculated by ultrasound guidance into the prostate gland of a healthy dog. The dog was then imaged with a combined trans-rectal NIR and TRUS imager using an integrated trans-rectal NIR/US applicator. The image was taken by NIR and US modalities concurrently, both in sagittal view. The trans-rectal NIR imager is a continuous-wave system that illuminates 7 source channels sequentially by a fiber switch to deliver sufficient light power to the relatively more absorbing prostate tissue and samples 7 detection channels simultaneously by a gated intensified high-resolution CCD camera. This work tests the feasibility of detecting prostate tumor by trans-rectal NIR optical tomography and the benefit of augmenting TRUS with trans-rectal NIR imaging.

**Keywords:** Prostate; near-infrared optical tomography; trans-rectal; ultrasound; transmissible venereal tumor.

## **1. INTRODUCTION**

Prostate cancer is prevalent in the men in the U.S. and in the industrialized countries [1]. Most of the prostate cancers are diagnosed at earlier stage now with the use of the sensitive prostate-specific antigen (PSA) test [2] aided by the digital rectal exam (DRE). Prostate biopsy, guided by trans-rectal ultrasound (TRUS), is performed when the pathological evidence is needed to confirm or rule out the onset of carcinoma in prostate [3].

The real-time utility and the excellent morphological information of TRUS make it ideal for visualizing the needle trajectory during the biopsy. TRUS had been utilized to assess the malignant changes in prostate tissue [4], unfortunately, the lack of specificity has limited the value of TRUS in diagnostic imaging of the prostate cancer and transformed the role of TRUS to becoming primarily an imaging tool for placing the biopsy needle. The accuracy of TRUS imaging may be improved by augmenting it with a functional contrast, thereby reducing unnecessary biopsies and more accurately targeting the malignant areas for biopsy. The near-infrared (NIR) light is known to reveal significant functional contrasts between a tumor and normal tissue originated from the angiogenic and hypoxic changes of the malignancy [5-11]. However, using NIR alone is less viable for prostate imaging due to its low spatial resolution and non-real time image reconstruction. An appealing approach is to combine NIR and TRUS to take advantage of the complementary features of NIR and TRUS.

*In vivo* imaging of NIR tomography of the prostate to augment TRUS is confronted with difficulties uncommon to the previous application of NIR tomography in cancer imaging. First of all, the prostate lies deep inside the pelvic compartment wherein the imaging by trans-rectal probing may be the optimal choice. In trans-rectal probing the NIR light will be attenuated by the condom (required when using TRUS) first, then the rectum wall, and the peri-rectum



tissue before reaching the prostate. As the light reaches the prostate, reflection on the prostate capsule and the potentially strong absorption by the peripheral vascular structures may limit the amount of light interrogating the deep prostate tissues. Secondly there is considerable challenge of fabricating an endo-rectal NIR applicator which should contain a number of source and detector channels if spatially-resolved imaging of large tissue volumes of the prostate is intended. The challenge becomes more pronounced when the NIR is to be combined with TRUS [12].

Recently we have constructed a trans-rectal NIR/US probe and validated the utility of the combined trans-rectal NIR/US imaging in a cadaver canine prostate *in situ* [13]. In this paper, we demonstrate the *in vivo* utility of the trans-rectal NIR/US imaging by use of a canine prostate bearing transmissible venereal tumor (TVT). TVT has an anechoic response that makes it visible on the TRUS. The TVT is known to have a higher cell density that tends to absorb and potentially scatter more NIR light than does the normal prostate tissue. In this work, the TVTs in the prostate and periprostatic tissue were located by TRUS, then imaged by NIR tomography *in situ*. The TVTs are shown as strong hyper-absorptive and moderately hyper-scattering on NIR tomography images being reconstructed without any prior.

## 2. METHODS AND MATERIALS

### 2.1 Sagittal-imaging trans-rectal NIR/US system

The details of the integrated sagittal-imaging trans-rectal NIR/US applicator and system are described elsewhere [13]. Briefly, this combined imaging applicator consists of a custom-built NIR probe and a commercial bi-plane TRUS transducer. The 7.5MHz sagittal-imaging transducer of the TRUS probe is used to couple with the NIR. The NIR applicator was fabricated to a cap-shape and attached to the TRUS probe on the top with a slot opened to expose the sagittal US transducer. The NIR array substrate was fabricated from a black polycarbonate material to satisfy the absorptive boundary condition. The NIR probe consists of two linear arrays, one for the source and the other for the detector, separated by 20mm and placed on each side of the sagittal TRUS transducer of 60mm in length. Each linear-array consists of 7 channels spaced 10mm apart and covering a total length of 60mm. Each NIR channel consists of a metal-coated fiber epoxied to a gradient-index lens and a prism to deflect the light to and from the probe surface.

The geometric relation between the imaging probe and the prostate is depicted in Fig. 1 where the optical channels are seen arranged cranial-caudally from 1 to 7. The NIR light illuminates through the condom, the rectum, and propagates into the prostate.

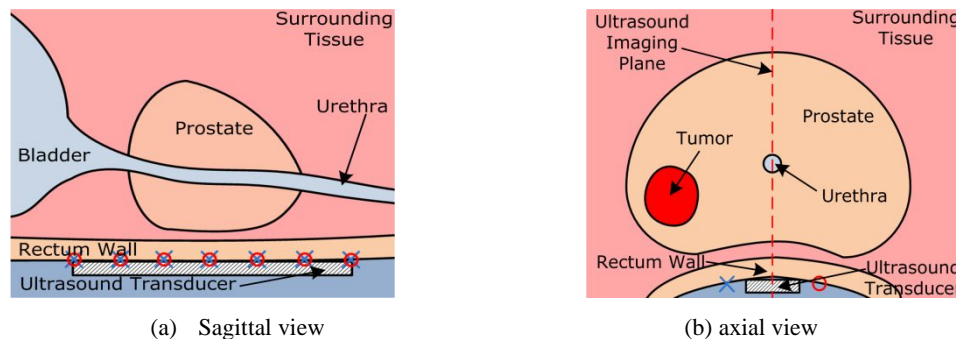


Fig. 1 Illustration of the TRUS coupled trans-rectal NIR imaging of the prostate. The TRUS middle-sagittal plane is marked by a red dash-line. The red circles denote NIR sources and the blue crosses denote the NIR detectors.

The TRUS probe is connected to an Aloka-3500 scanner. The US images were transferred to the main computer of the combined NIR/US imager by a PCI image acquisition card (National Instruments PCI-1405). The NIR imager uses a custom-designed superluminescent diode (SLD) (Superlumdiodes Inc.) that is pigtailed to a multi-mode fiber and delivers 100mW of 840nm NIR light with 14.2nm FWHM bandwidth. The SLD output beam is focused and delivered sequentially onto 7 source fibers of the NIR applicator by a translating fiber multiplexer. The entire NIR bandwidth is coupled to each fiber at a time. The remitted NIR light is collected by 7 detection fibers coupled to a spectrometer (Acton Research). A 16-bit intensified CCD camera (Princeton Instruments) acquires the 7 optical signals corresponding to one source simultaneously, and a complete set of data for all 7 source channels is taken within 5 seconds.

### 2.2 Animal model

Dogs have been previously used for prostate tumor model studies because of the similarity between canine and human prostate glands [14-16]. For this study, the prostate of a mature dog was injected with canine TVT cells with the purpose

of developing an *in vivo* prostate tumor model for NIR/US imaging. The unique canine TVT is a round cell tumor of dogs that mainly affects the external genitalia and can be transmitted from animal to animal during copulation, regardless of histocompatibility. The neoplastic cells are generally thought to be of histiocytic origin [17]. TVT cells can be propagated in immunocompromised (SCID) mice and transferred to different tissues (such as the prostate gland) of the dog to result in a neoplastic mass effect useful for imaging studies [16].

The experiments were conducted in the Center for Veterinary Health Sciences at Oklahoma State University under a protocol approved by the university's Institutional Animal Care and Use Committee. The protocol was also approved and underwent an on-site inspection by the US Army Medical Research and Material Command. For these studies, an existing TVT cell line was obtained as cryopreserved tissue from MD Anderson Cancer Center (Houston, TX). The tumor tissue was quick-thawed, homogenized and inoculated into the subcutis of a NOD/SCID mouse. After approximately 12 weeks, the tumor reached an appropriate volume ( $4.0\text{--}4.5\text{cm}^3$ ) for recovery and were processed and inoculated into a second NOD/SCID mouse. Following growth in the second mouse (8 weeks), the neoplastic cells were recovered and homogenized for inoculation into the canine prostate gland.

A 12 kg sexually intact adult Beagle dog estimated to be approximately 4 years of age was housed single in a inside run and given free access to water and food. For TVT cell injection, the dog was anesthetized using an intravenous injection of propofol (8mg/kg) followed by intubation and halothane/oxygen inhalation anesthetic maintenance. The animal was placed in left lateral recumbency for bowel preparation and physical examination of the prostate. The perineum was aseptically prepared for injection and under TRUS visualization, a 6-inch 16 gauge hypodermic needle was inserted transperineally into the right lobe of the prostate where 3 cc of the prepared TVT cells were injected. During retraction of the injection needle, it was considered unavoidable that TVT cells would leak from the prostate injection site and be "seeded" along the needle insertion tract.

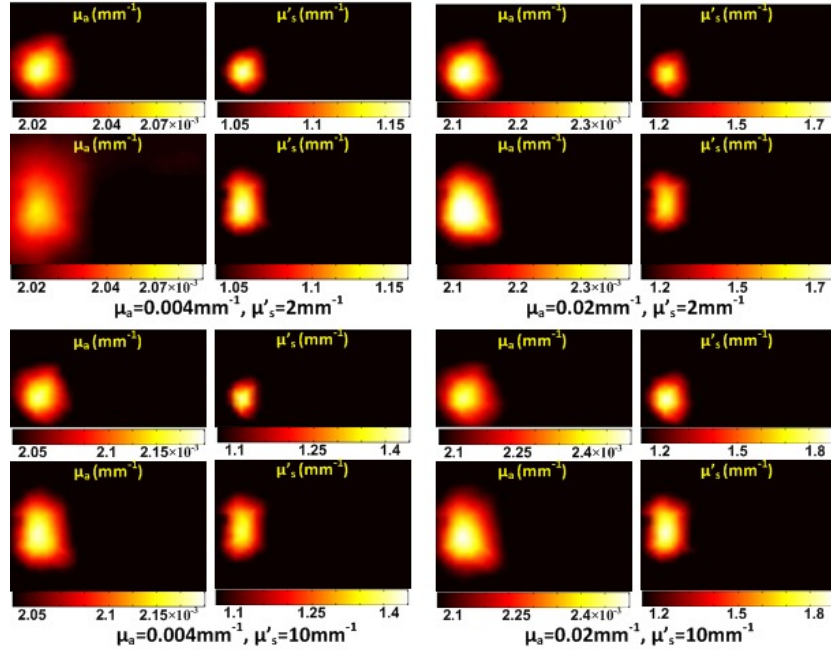
The dog was examined weekly by TRUS using a condom-covered combined NIR/US probe. For all TRUS and NIR follow-on imaging sessions, the dog underwent general anesthesia using a similar protocol used for TVT cell injection. During the first two weeks following TVT cell injection there was no evidence of tumor growth. The next TRUS examination occurred 5 weeks post-injection when hypoechoic masses were observed both in the prostatic parenchyma and peri-prostatically around the right lobe of the prostate. The dog underwent weekly monitoring for 2 more weeks, and was then humanely euthanized 8 weeks after the initial TVT cell injection. A complete necropsy was performed with the prostate and peri-prostatic structures submitted for histological examination.

### 3. SYSTEM PERFORMANCE

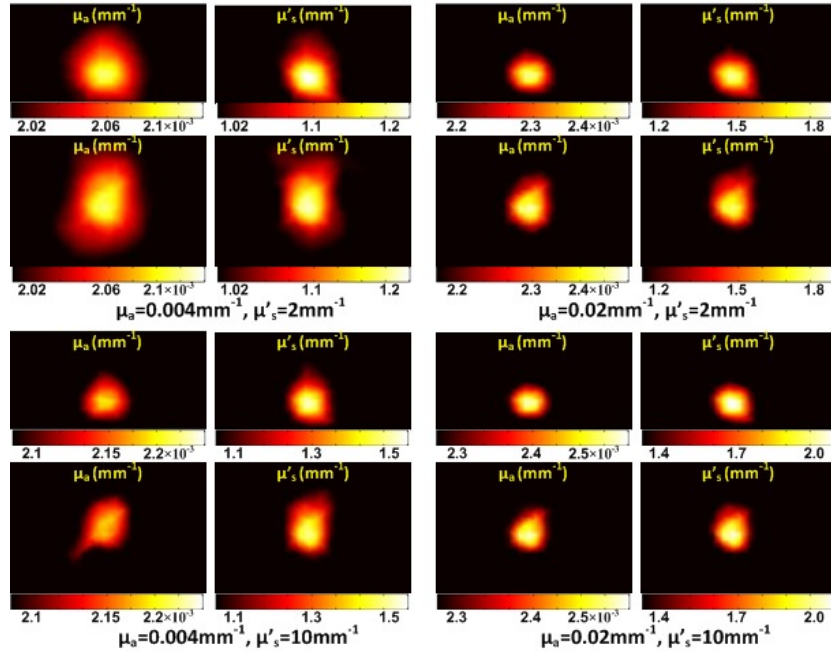
The combined NIR/US probe & system enables concurrent acquisition of trans-rectal NIR tomography and TRUS images on the same sagittal plane. Our previous studies have validated that incorporating TRUS *a priori* information allows trans-rectal NIR tomography to recover an absorption target accurately. We have also demonstrated that trans-rectal NIR imaging could recover an absorptive target with no spatial prior. In this paper, the TRUS is used to locate a suspected TVT target, and NIR image reconstruction is performed without *prior* information in order to examine if the TVT shows inherent NIR contrast. As our trans-rectal NIR probe allows 3-dimensional imaging, the system performance is evaluated for recovering targets located on or off the sagittal plane when using only the NIR information.

#### 3.1 Reconstruction of a target on the mid-sagittal plane-----Simulation

The performance of reconstructing absorptive targets in the sagittal-plane using continuous-wave measurement has been investigated previously [13]. As the optical scattering properties of the prostate cancer and the benign tissue may be different, simulation is performed to investigate reconstruction of the reduced scattering property of a target using continuous-wave measurements. Figure 2 lists the results simulated for a single target having both absorption and scattering contrasts over the background. The homogeneous background (for all the simulations conducted in this work) is set at  $\mu_a$  (absorption coefficient) of  $0.002\text{mm}^{-1}$  and  $\mu'_s$  (reduced scattering coefficient) of  $1.0\text{mm}^{-1}$ . The  $\mu_a$  of the target is set at  $0.004\text{mm}^{-1}$  and  $0.02\text{mm}^{-1}$ ; the  $\mu'_s$  of the target is set at  $2.0\text{mm}^{-1}$  and  $10\text{mm}^{-1}$ . The target is a sphere of 10mm in diameter and located along the middle-sagittal plane (the TRUS imaging plane) at a depth of 10mm. Figure 2(a) shows the results for the target at a depth of 10mm and placed 20 mm longitudinally from the mid-line of the sagittal plane. Figure 2(b) shows the results when the target is at the mid-line of the sagittal plane. The sagittal and coronal locations of the target are correctly reconstructed. Cross-coupling between the absorption and scattering reconstructions out of the continuous-wave data is not observed, however, the optical properties are underestimated.

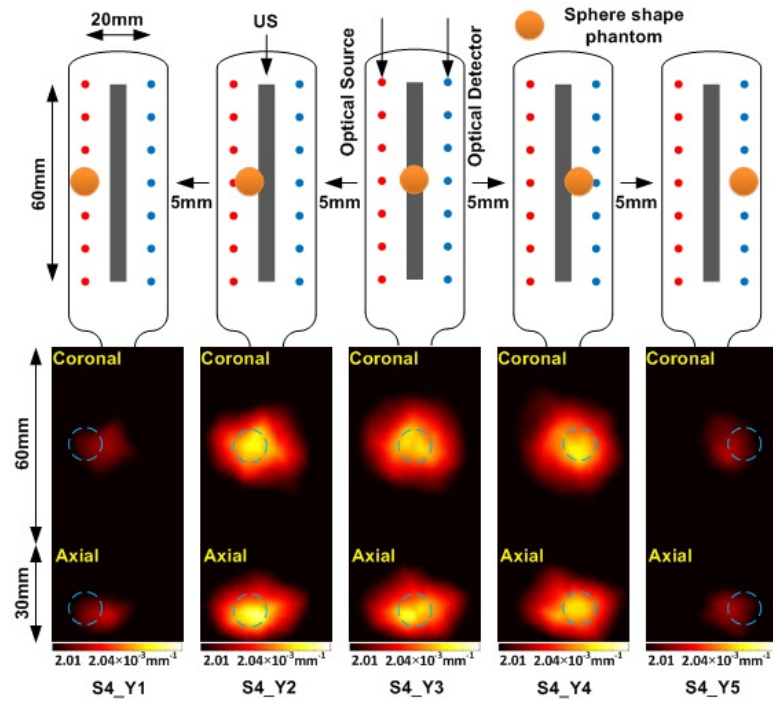


(a) Target shift 20mm longitudinally from the mid-point

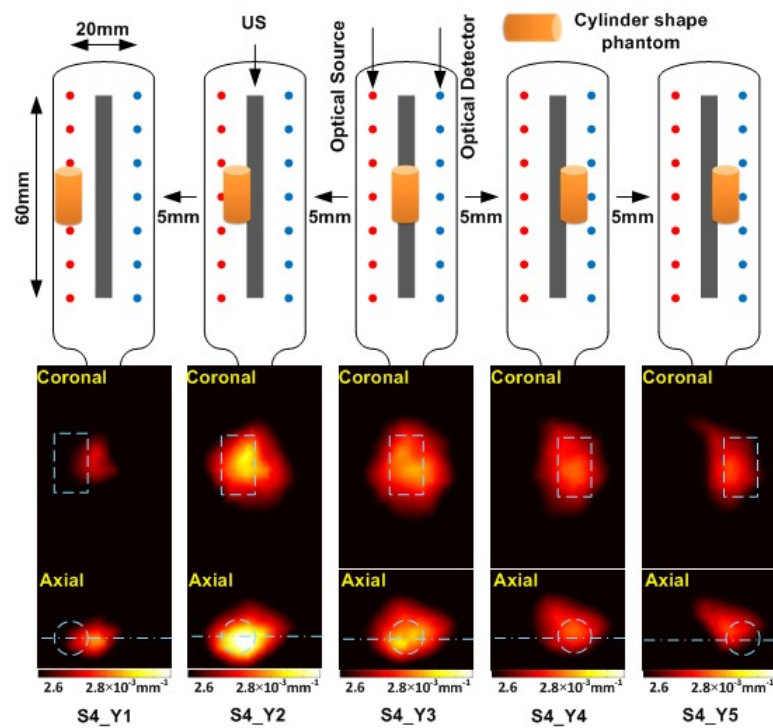


(b) Target at the mid-point

Figure 2 Reconstruction of the absorption and reduced scattering of a target located in the sagittal plane based on continuous-wave data. For each set of 4-image, the top row corresponds to the sagittal view, and the bottom row corresponds to the coronal view.



(a) Simulation for a sphere target



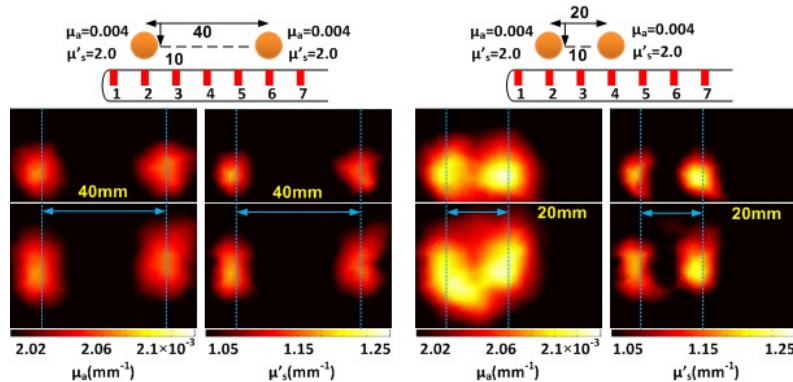
(b) Experimental results for a cylinder target

Figure 4. Recovering of a target at different lateral positions.

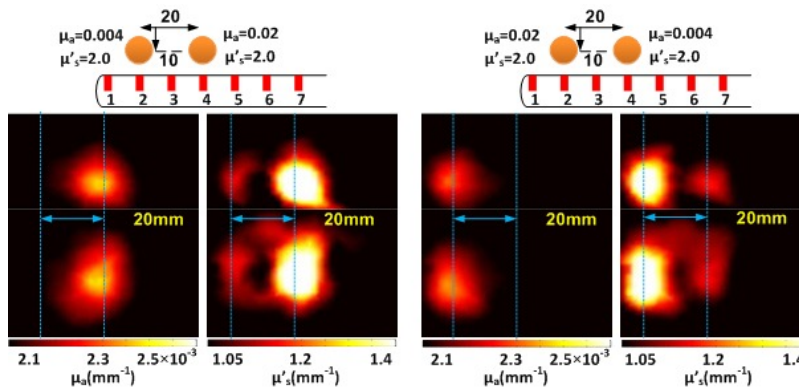
### 3.2 Reconstruction of a target off the mid-sagittal plane----Simulation and experimental results

The geometry of the trans-rectal NIR applicator allows 3-dimensional imaging. The reconstruction of a target located off the middle-sagittal plane is illustrated in Fig. 4. Figure 4 (a) shows the target being displaced from left-lateral to right-

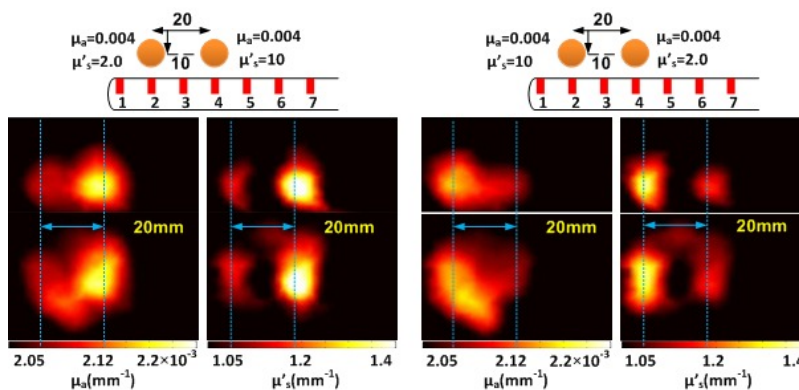
lateral at 5mm per step. The target is a sphere of 10mm in diameter with  $\mu_a$  of  $0.0056\text{mm}^{-1}$  and  $\mu'_s$  of  $1.03\text{mm}^{-1}$ . The experiment results are shown as Fig. 4(b) for a target of cylinder shape (10mm in diameter and 16mm in length) having the same optical properties of the target in simulation of (a). Both the simulation and the experimental results indicated that a target off the middle-sagittal plane may be recovered by NIR only, but at slightly displaced spatial location.



(a) Multiple targets with the same absorption and scattering coefficients



(b) Multiple targets with different absorption but same scattering coefficients



(c) Multiple targets with same absorption but different scattering coefficients

Figure 1. Reconstruction of multiple targets

### 3.3 Reconstruction of multiple targets on the mid-sagittal plane-----Simulation

The performance of differentiating multiple targets on the mid-sagittal plane is evaluated by simulation. The simulation is performed for two sphere targets of 10mm in diameter. In (a) the two targets have the same  $\mu_a = 0.004\text{mm}^{-1}$  and

$\mu'_s = 2.0\text{mm}^{-1}$ . At 40mm longitudinal separation, the targets can be separated on both  $\mu_a$  and  $\mu'_s$  images. At closer separation, overlapping of the two targets is seen on  $\mu_a$  before on  $\mu'_s$ . In (b), the two targets are 20mm apart, the  $\mu'_s$  of both is  $2.0\text{mm}^{-1}$ , and the  $\mu_a$  values are set at  $0.004\text{mm}^{-1}$  and  $0.02\text{mm}^{-1}$  respectively. In the  $\mu_a$  image, only the higher contrast target is recovered. While in the  $\mu'_s$  image, the lower contrast target is recovered but with cross-coupling from the higher contrast target. In (c), the  $\mu_a$  is  $0.004\text{mm}^{-1}$  for both, and the  $\mu'_s$  is set at  $2.0\text{mm}^{-1}$  and  $10\text{mm}^{-1}$  for the two targets. The two targets are recovered on  $\mu'_s$  image, but barely separated on the  $\mu_a$  image. The above simulation and experimental results demonstrate the utility of reconstructing both  $\mu_a$  and  $\mu'_s$  based on continuous-wave measurement even though the recovery of the target is not satisfactory for all conditions.

## 4. IN VIVO RESULTS

The results of in vivo trans-rectal NIR tomography and TRUS of the canine are presented in Fig. 6 for the NIR absorption images and Fig. 7 for the NIR reduced scattering images. All NIR images are displayed with consistent color scales for both  $\mu_a$  and  $\mu'_s$ . The dimensions of US and NIR images are 60mm (cranial-caudal)×30mm (posterior-anterior) for sagittal, 40mm (right lateral –left lateral)×30mm (posterior-anterior) for axial, and 60mm (cranial-caudal)×40mm (right lateral –left lateral) for coronal views, respectively.

### 4.1 Hyper-absorptive indication of the TVT on NIR image

The three sagittal TRUS images (Fig. 6) were taken at the mid-line of the prostate, the middle portion of the right lobe of the prostate, and the right lateral edge of the prostate. The hypo-echoic region L1 indicates an abnormal intra-prostatic mass. The large hypo-echoic region L2 indicates an abnormal mass anterior and caudal to the prostate that may have connection with L1. The NT on the right lobe US image denotes the needle trajectory for introducing the TVT cells. Longitudinal hypo-echoic regions including L3 are seen along the NT. The three sagittal NIR images correspond to the US taken at the middle portion of the right lobe, 10mm medial to it and 10mm lateral to it, respectively. Hyper-absorptive regions on sagittal NIR images correspond to L1, L2, and L3 on sagittal US images. The 10mm-medial NIR image shows reduced contrast for the absorptive masses, and the 10mm-lateral NIR reveals connected strong absorptive masses. The bladder is seen as slightly hypo-echoic at the 2 more medial sagittal US images; however, no hyper-absorptive mass is presented at the left-most region of the sagittal NIR images.

The three axial TRUS images were taken at the cranial edge of the prostate crossing L1, the caudal edge of the prostate crossing L2, and the peri-rectal region crossing L3. The axial US images show a small hypo-echoic intra-prostatic mass at cranial side of the prostate, the bulging of the right lobe and extending of the L2 over the prostate mid-line that correlates with the findings on mid-line sagittal US, and large peri-rectal hypo-echoic mass cranial to the perineum. Of the five axial NIR images, the longitudinal positions are 10mm apart from cranial to caudal. The axial NIR image A2 should contain L1, and the axial NIR image A5 should contain L3.

The coronal NIR images correspond to 5mm, 10mm, and 15mm anterior to the anterior edge of the rectal lumen. The hyper-absorptive mass indicative of L1 is seen medial to the hyper-absorptive masses indicative of L2 and L3. The anatomies of the hyper-absorptive masses on the NIR images in 3-views agree with the hypo-echoic regions on the US images in 2-views.

The US and NIR imaging were also performed at the middle-line of the left lobe where no abnormal features were found on the US, and globally homogenous and low absorption was seen in the NIR images.

### 4.2 Hyper-scattering indication of the TVT on NIR image

The hyper-absorptive masses in Fig.6 being suspicious of TVTs are shown in Fig. 7 with different patterns of the reduced scattering contrast, indicating minimum cross-coupling between the reconstructions of  $\mu_a$  and  $\mu'_s$  from the in vivo continuous-wave measurement. In the scattering NIR images, L3 has much higher contrast than do the other masses corresponding to L1 and L2. The contrast elsewhere is also slightly more homogenous compared with that in the absorption image.



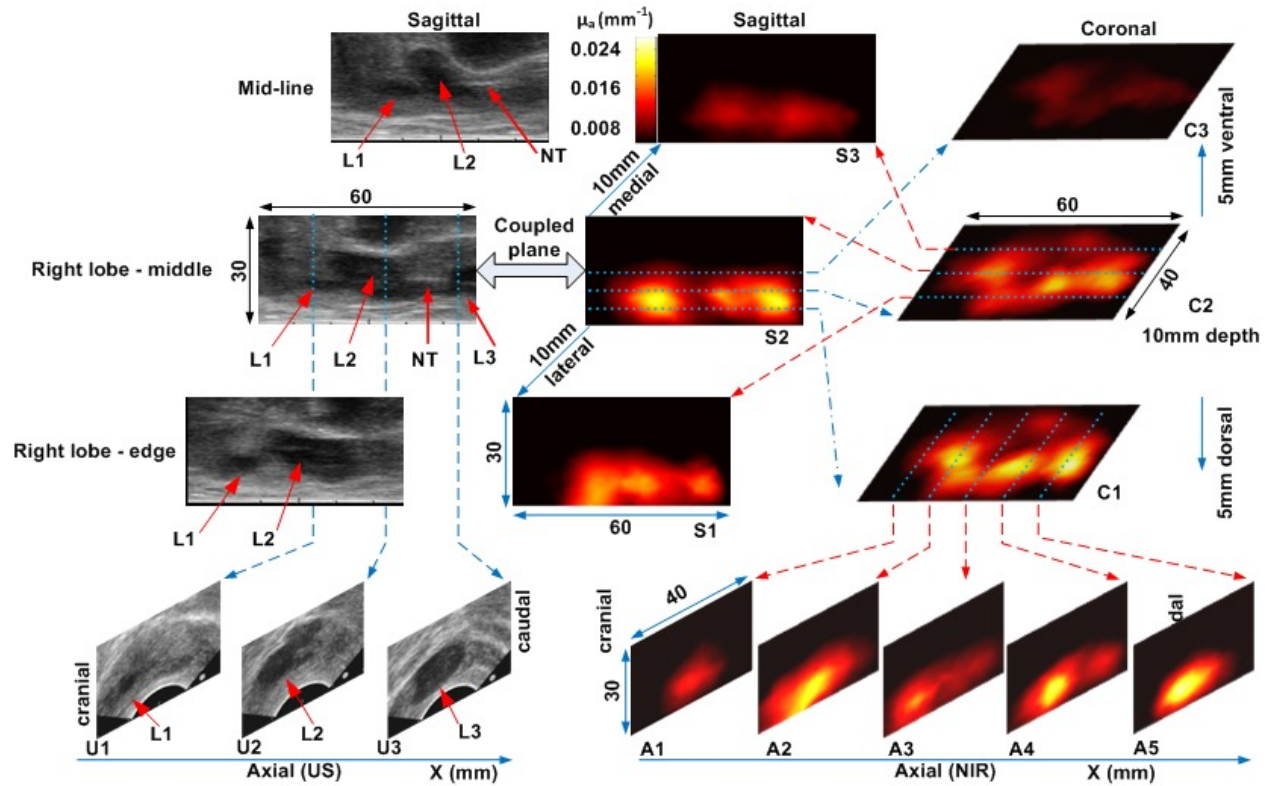


Figure 2. Trans-rectal NIR imaging (absorption) in 3-views vs TRUS imaging in 2-views

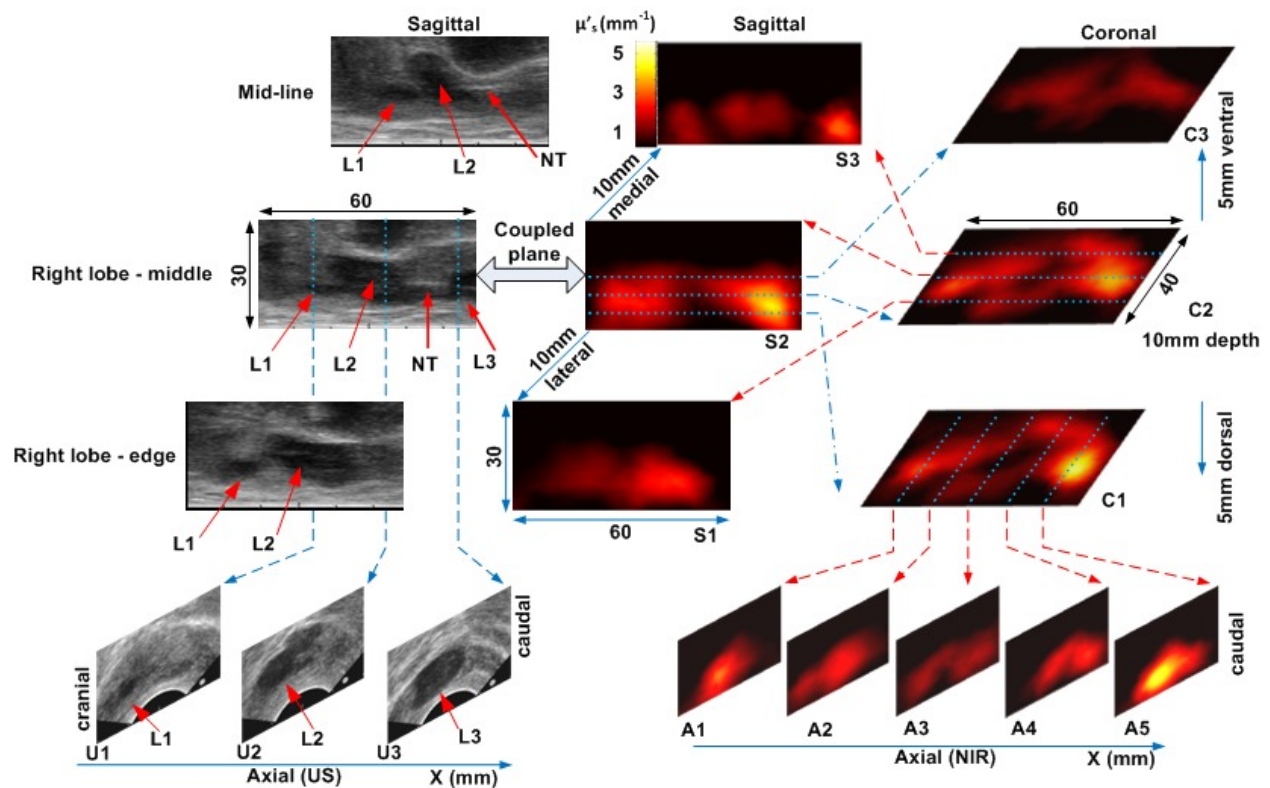


Figure 7. Trans-rectal NIR imaging (reduced scattering) in 3-views vs TRUS imaging in 2-views

### 4.3 Confirmation of the TVT growth

The mass L3 indicated by the US and NIR correlates with a large peri-prostatic nodule along the needle track site determined by digital rectal examination prior to imaging. Necropsy confirmed that L3 was a peri-rectal nodule along the needle track. The necropsy also confirmed a large nodule, corresponding to L2, anterior to the prostate at the caudal side of the prostate that extended from the right-lateral aspect of the prostate to the middle-line of the prostate. Exposing the interior of the prostate also confirmed a nodule at the right lobe of the prostate that corresponds to the mass L1. Histological examination confirmed all nodules to be TVT.

## 5. DISCUSSIONS AND CONCLUSIONS

Among the hypo-echoic masses shown on the US, L1 was intra-prostatic, L2 was largely anterior to the prostate, and L3 was caudal to the prostate. These 3 masses are however shown at similar depths on NIR images. This is attributed to the un-even NIR sensitivity profile along the posterior-anterior direction [12]. It is however noted that the existence of TVT nodules have been recovered by use of only the NIR information. If the anatomic location of the TVT available from the US can be utilized as the spatial prior for NIR image reconstruction, the localization of the TVT nodules on NIR images will certainly be more accurate.

It is known that most of the prostate cancers are presented as multi-focal [18, 19]. It must be noted that the intraprostatic TVT tumors were initiated and developed during this project in a non-immunosuppressed canine model. The subject in this study developed multiple TVT nodules intra-prostatically and peri-prostatically. Although the sites of the TVT tumors were not totally confined to the prostate, the successful imaging of multiple TVT tumor nodules by trans-rectal NIR tomography implies the feasibility of recovering multiple intra-prostatic TVT tumors. All of the TVT tumor nodules developed in this subject were shown strongly hypo-echoic on the US, which correlates with the strongly hyper-absorptive and moderately hyper-scattering findings on NIR imaging. The bladder, on the other hand, shows hypo-echoic on the ultrasound; however it is not shown as hyper-absorptive or hyper-scattering on the NIR images. This confirms that trans-rectal NIR tomography has higher specificity of imaging the regions hypo-echoic to TRUS.

It has been well-demonstrated that cancers in organs like breast are presented in NIR tomography as having increased absorption and different reduced scattering contrast over the normal tissues when imaged intact, *in situ* and *in vivo*. However, there was previously no information on the optical contrast of prostate cancer compared to normal prostatic or peri-prostatic tissue taken at intact prostate *in situ* and *in vivo*. Our work presents a new paradigm for prostate imaging that shows promises of improving the specificity of TRUS imaging by augmenting it with trans-rectal NIR tomography.

In conclusion, this work reported *in vivo* imaging of TVT tumors in the canine prostate and pelvic canal by trans-rectal NIR tomography coupled with TRUS. The TVT tumor nodules show strong NIR absorption and moderate scattering contrasts over the normal prostatic and peri-prostatic tissues. Correlation of the TVT locations is found between trans-rectal NIR and TRUS results.

## 6. ACKNOWLEDGEMENT

This work has been supported by the Prostate Cancer Research Program of the U.S. Army Medical Research Acquisition Activity (USAMRAA), 820 Chandler Street, Fort Detrick MD, 21702-5014, through grant #W81XWH-07-1-0247.

### References:

1. A. Jemal, R. Siegel, E. Ward, T. Murray, J. Xu, and M. J. Thun, "Cancer statistics, 2007," *CA Cancer J. Clin.* **57**, 43-66 (2007).
2. T. J. Polascik, J. E. Oesterling, and A. W. Partin, "Prostate specific antigen: a decade of discovery--what we have learned and where we are going," *J. Urol.* **162**, 293-306 (1999).
3. A. C. Loch, A. Bannowsky, L. Baeurle, B. Grabski, B. König, G. Flier, O. Schmitz-Krause, U. Paul, and T. Loch, "Technical and anatomical essentials for transrectal ultrasound of the prostate," *World J. Urol.* **25**, 361-366 (2007).
4. B. Spajic, H. Eupic, D. Tomas, G. Stimac, B. Kruslin, and O. Kraus, "The incidence of hyperechoic prostate cancer in transrectal ultrasound-guided biopsy specimens," *Urology* **70**, 734-737 (2007).
5. B. Tromberg, J. Coquoz, O. Fishkin, J. B. Pham, T. Anderson, E. R. Butler, J. Cahn, M. Gross, J. D. Venugopalan, and D. Pham, "Non-invasive measurements of breast tissue optical properties using frequency-domain photon migration," *Phil. Trans. R. Soc. Lond. B* **352**, 661-668 (1997).
6. B. W. Pogue, S. P. Poplack, T.O. McBride, W. A. Wells, K. S. Osterman, U. L. Osterberg, and K. D. Paulsen, "Quantitative hemoglobin tomography with diffuse near-infrared spectroscopy: pilot results in the breast," *Radiology* **218**, 261-266 (2001).
7. V. Ntziachristos and B. Chance, "Probing physiology and molecular function using optical imaging: applications to breast cancer," *Breast Cancer Res.* **3**, 41-46 (2001).

8. R. Choe, A. Corlu, K. Lee, T. Durduran, S. D. Konecky, M. Grosicka-Koptyra, S. R. Arridge, B. J. Czerniecki, D. L. Fraker, A. DeMichele, B. Chance, M. A. Rosen, and A. G. Yodh, "Diffuse optical tomography of breast cancer during neoadjuvant chemotherapy: a case study with comparison to MRI," *Med. Phys.* **32**, 1128-1139 (2005).
9. M. A. Franceschini, K. T. Moesta, S. Fantini, G. Gaida, E. Gratton, H. Jess, W. W. Mantulin, M. Seeber, P. M. Schlag, and M. Kaschke, "Frequency-domain techniques enhance optical mammography: initial clinical results," *Proc. Nat. Acad. Sci. USA* **94**, 6468-6473 (1997).
10. Q. Zhu, E. B. Cronin, A. A. Currier, H. S. Vine, M. Huang, N. Chen, and C. Xu, "Benign versus malignant breast masses: optical differentiation with US-guided optical imaging reconstruction," *Radiology* **237**, 57-66 (2005).
11. S. A. Bigler, R. E. Deering, and M. K. Brawer, "Comparison of microscopic vascularity in benign and malignant prostate tissue," *Hum. Pathol.* **24**, 220-226 (1993).
12. G. Xu, D. Piao, C.H. Musgrove, C.F. Bunting, H. Dehghani, "Trans-rectal ultrasound-coupled near-infrared optical tomography of the prostate Part I: Simulation," *Optics Express*, 16(22), 17484-17504 (2008).
13. Z. Jiang, D. Piao, G. Xu, J.W. Ritchey, G.R. Holyoak, K.E. Bartels, C.F. Bunting, G. Slobodov, J.S. Krasinski, "Trans-rectal ultrasound-coupled near-infrared optical tomography of the prostate Part II: Experimental demonstration," *Optics Express*, 16( 22), 17505-17520 (2008).
14. J.D. Hazle, C.J. Diederich, M. Kangasniemi, R.E. Price, L.E. Olsson, and R.J. Stafford, "MRI-guided thermal therapy of transplanted tumors in the canine prostate using a directional transurethral ultrasound applicator," *J Magn Reson Imaging.*, 15(4), 409-17 (2002).
15. F. Forsberg, D.K. Johnson, D.A. Merton, J.B. Li, P.E. Losco, E.K. Hagen, and B.B. Goldberg, "Contrast-enhanced transrectal ultrasonography of a novel canine prostate cancer model," *J Ultrasound Med.*, 21(9), 1003-13 (2002).
16. B. Rivera, K. Ahrar, M.M Kangasniemi, J.D. Hazle, R.E. Price, "Canine transmissible venereal tumor: a large-animal transplantable tumor model," *Comp Med.*, 55(4), 335-43 (2005).
17. E. Mozos, A. Mendez, J.C. Gomez-Villamandos, J.M. De Las Mulas, J. Perez, "Immunohistochemical characterization of canine transmissible venereal tumor," *Vet Pathol.*, 33, 257-263 (1996).
18. A. M. Wise, T. A. Stamey, J. E. McNeal, and J. L. Clayton, "Morphologic and clinical significance of multifocal prostate cancers in radical prostatectomy specimens," *Urology* **60**, 264-9 (2002).
19. G. J. Miller and J. M. Cygan, "Morphology of prostate cancer: the effects of multifocality on histological grade, tumor volume and capsule penetration," *J. Urol.* 152(5 Pt 2), 1709-13 (1994).